

The Spectrum and Scale Setting on 2+1-flavor NME Lattices

Jun-Sik Yoo,^{1,*} June-Haak Ee,^{2,†} Sungwoo Park,^{3,4,‡} Rajan Gupta,^{5,§} Tanmoy Bhattacharya,^{5,¶} Santanu Mondal,^{6,**} Bálint Joó,^{7,††} Robert Edwards,^{8,‡‡} Kostas Orginos,^{8,9,§§} and Frank Winter^{8,¶¶}

¹*Department of Physics, Korea University, Seoul 02841, Korea*

²*Center for Theoretical Physics – a Leinweber Institute,*

Massachusetts Institute of Technology, Cambridge, MA 02139, USA

³*Physical and Life Sciences Division, Lawrence Livermore National Laboratory, Livermore, CA 94550, USA*

⁴*Nuclear Science Division, Lawrence Berkeley National Laboratory, Berkeley, CA 94720, USA*

⁵*Theoretical Division, Los Alamos National Laboratory,*

PO Box 1663, MS B283, Los Alamos, NM 87545, USA

⁶*Ibsyn Scientific, 75C Park St, Kolkata, India 700016*

⁷*NVIDIA Corporation, Santa Clara, CA 95051, USA.*

⁸*Jefferson Lab, 12000 Jefferson Avenue, Newport News, Virginia 23606, USA*

⁹*Department of Physics, College of William and Mary, Williamsburg, Virginia 23187-8795, USA*

(Dated: January 19, 2026)

This paper describes the thirteen ensembles, named NME, generated with 2+1-flavor Wilson-clover fermions by the JLab/W&M/LANL/MIT/Marseille collaborations, and presents an analysis of the meson and baryon spectrum, decay constants f_π and f_K , flow scales t_0 and w_0 , and time histories of the Θ and Weinberg operators under gradient flow. Using these quantities, the physical point values of the two flow scales, t_0^{Phy} and w_0^{Phy} , and the ratio f_K/f_π^{Phy} are determined. The masses of the octet and decuplet baryons are analyzed using both the next-to-leading order (NLO) and the next-next-to-leading order (NNLO) ansatz from heavy baryon chiral perturbation theory (HB χ PT). The NNLO fit to the octet baryons, M_N , M_Σ , M_Λ and M_Ξ , is preferred while the corresponding fits to the decuplet Omega mass, M_Ω , are not distinguished. We also present a study of the autocorrelations in the data and show that there is no evidence, even at large flow time, of the freezing of the topological charge or the Weinberg three-gluon operator.

I. INTRODUCTION

The starting point of all lattice Quantum Chromodynamics (QCD) calculations is a set of ensembles of gauge configurations that cover a large range of values of the lattice spacing a , quark masses, and lattice volumes $L^3 \times T$ so that results can be extrapolated to the physical point defined by the physical quark masses, $\{m_u, m_d, m_s, m_c, m_b\}$, infinite volume, $L \rightarrow \infty$, and the continuum limit, $a \rightarrow 0$. Over the last ten years, the JLab/W&M/LANL/MIT/Marseille collaborations¹ have generated thirteen ensembles of 2+1-flavors of Wilson-clover fermions using the Hybrid Monte Carlo (HMC) algorithm [1]. Simulations of 2+1-flavor lattice QCD involve four parameters: the lattice spacing a , two quark

masses, light ($m_l = (m_u + m_d)/2$) and strange (m_s), and a large spatial lattice size L with the understanding that for zero temperature simulations, the temporal size $T \geq L$ in all cases. The lattice spacing is essentially fixed as a function of the gauge coupling $\beta \equiv 6/g^2$, with a small dependence on the quark masses for Wilson fermions because they break chiral symmetry explicitly [2]. Our goal is to use these lattices to calculate the matrix elements of various quark bilinear operators within nucleon states and to also make them available to members of the USQCD collaboration for non-competitive calculations. First results from a subset of these ensembles have been presented in Refs. [3–6].

The generated ensembles cover the range $0.053 \text{ fm} \leq a \leq 0.117 \text{ fm}$ in lattice spacing, $3.7 \leq M_\pi L \leq 6.2$ in lattice size and four values of the pion mass: $M_\pi \approx 290, 230, 175, 135 \text{ MeV}$. The lattice parameters of these 13 ensembles are summarized in Tables I and II, and, in this work, we present an analysis of the meson and baryon spectrum, the decay constants f_π and f_K , the setting of the lattice scale a , the behavior of the topological charge and Weinberg three-gluon operator under gradient flow, and results for the renormalization constants for all five quark bilinear local operators.

The following sections provide a summary of the ensembles generated and analyzed, the lattice methodology for the quantities calculated, the quality of the signal obtained, the analysis strategy for the various observables, and the chiral-continuum extrapolation ansatz used to obtain data at the physical point, i.e., at $M_\pi = 135 \text{ MeV}$,

* junsik.yoo@outlook.com

† jhee@mit.edu

‡ sungwoo@sejong.ac.kr (Corresponding Author)

§ rg@lanl.gov

¶ tanmoy@lanl.gov

** santanu.sinp@gmail.com

†† bjoo@nvidia.com

‡‡ edwards@jlab.org

§§ kostas@wm.edu

¶¶ fwinter@jlab.org

¹ The full list of contributors to lattice generation are Robert Edwards, David Richards, and Frank Winter (JLAB); Bálint Joó (NVIDIA); Kostas Orginos (W&M); Tanmoy Bhattacharya, Rajan Gupta, Santanu Mondal, Sungwoo Park and Boram Yoon (LANL); William Detmold, David Murphy, Phiala Shanahan (MIT); and Savvas Zafeiropoulos (Marseille).

$M_K = 495$ MeV, $a = 0$ and $L = \infty$. The full calculation, including the generation of the lattices, the inversion of the Dirac operator, and the measurement of the two-point correlation functions was done using the CHROMA software package [7].

A. Methodology: Lattice Generation

The generation of lattices using the 2+1-flavor Wilson-clover action was carried out using the rational hybrid Monte Carlo (RHMC) algorithm [1] as described in Ref. [4]. The action, set up by the JLab/W&M collaborations [8], is

$$\begin{aligned} S &= S_G + S_F \\ S_G(U) &= \frac{a^4}{6g^2} \left[\sum_{x,\mu,\nu} (1 - 8c_1) \Re \text{Tr}(1 - U_{\mu\nu}(x)) \right. \\ &\quad \left. + \sum_{x,\mu,\nu} \frac{c_1}{u_0^2} \Re \text{Tr}(1 - U_{\mu\nu}^6(x)) \right] \\ S_F^f(U, \bar{\psi}, \psi) &= a^4 \sum_f \sum_x \bar{\psi}_f(x) (D + m_f) \psi_f(x) \\ &\quad - \frac{C_{SW}}{4} \sum_f \sum_{x,\mu,\nu} \bar{\psi}_f(x) \sigma_{\mu\nu} G^{\mu\nu} \psi_f(x) \\ D &= \frac{1}{2} \sum_{\mu=1}^4 [(\nabla_\mu^+ + \nabla_\mu^-) \gamma_\mu - a \nabla_\mu^+ \nabla_\mu^-] \quad (1) \end{aligned}$$

where $\beta \equiv 6/g^2$ is the gauge coupling, $U_{\mu\nu}$ is the plaquette, $U_{\mu\nu}^6$ is the 1×2 Wilson loop, $G_{\mu\nu}$ is the field strength tensor, $\sigma_{\mu\nu} = (1/2)[\gamma_\mu, \gamma_\nu]$, ∇^\pm are the forward/backward covariant derivatives on the lattice, and m_f is the bare mass parameter for quark of flavor f . In this lattice formulation,

- the gauge part of the action, S_G , is the tree-level tadpole improved Symanzik with $c_1 = -1/12$.
- The Sheikholeslami-Wohlert coefficient C_{SW} [9] in the fermion part of the action, S_F , is set to the tadpole improved tree-level value, $c_{SW} = 1/u_0^3$ [10], where u_0 is the fourth root of the plaquette expectation value. This choice is very close to the nonperturbative value determined, a posteriori, using the Schrödinger functional method [11]. This closeness is attributed to the stout smearing of the links implemented in the action.
- The links entering the Dirac action are stout smeared using one iteration with weight $\rho = 0.125$ for the sum of the staples [12].
- In the molecular dynamics part of the HMC, we used a mass preconditioning scheme as described in [13, 14]. In this approach the fermion determinant for the light quarks is simulated as a chain of

fermion determinant ratios:

$$\det(M_0^\dagger M_0) = \left\{ \prod_{I=0}^{N-1} \frac{\det(M_i^\dagger M_i)}{M_{I+1}^\dagger M_{I+1}} \right\} \det(M_N^\dagger M_N) \quad (2)$$

where M_0 is the fermion matrix with the light quark mass and the M_i are auxiliary fermion matrices with quark masses increasing with I . The final term ends the chain by cancelling off the auxiliary determinant with the heaviest mass. Up to 3-4 auxiliary determinant ratios were used in the chain.

- A nested multiple time-scale integration scheme [15] with fourth order force-gradient integrators [16] was implemented using the trick of [17] at each time scale except potentially the innermost one. We integrated the determinant ratios and clover actions on the slowest level, the single flavor term on the second level, and the gauge action and the heavy cancellation 2-flavor action on the innermost level. While the cancellation term was computationally inexpensive due to its high mass, we further reduced its cost by utilizing a minimum residuum extrapolation “chronological” predictor [18].
- The Dirac matrix inversion was accelerated using a multi-grid solver [19, 20] where the multi-grid subspace was developed for the lightest quark mass at the start of the trajectory and was updated if a solution took more than 72 iterations. Because both the chronological predictor and the reuse of the subspace through the trajectory break reversibility in principle, and to maintain stability of molecular dynamics, a high accuracy (with a relative residuum of $O(10^{-10})$) was required for all solves.
- The time step in the molecular dynamics evolution was adjusted to obtain roughly 92% acceptance rate for trajectory length of one unit.

The parameters of the 13 ensembles are given in Tables I and II.

B. Methodology: Measurements

All spectral quantities presented here are extracted from fits to the spectral decomposition of the two-point correlation functions that describe the evolution of the meson and baryon states in Euclidean time τ :

$$\begin{aligned} \Gamma_2(\tau) &\equiv \langle \mathcal{O}^\dagger(\tau) \mathcal{O}(0) \rangle = \sum_i \langle 0 | \mathcal{O}^\dagger | S_i \rangle \langle S_i | \mathcal{O} | 0 \rangle e^{-E_i \tau} \\ &= \sum_i A_i^* A_i e^{-E_i \tau}, \quad (3) \end{aligned}$$

where \mathcal{O} is the interpolating operator used to create/annihilate the states and $A_i \equiv \langle S_i | \mathcal{O} | 0 \rangle$ is the amplitude for \mathcal{O} to create (or annihilate) the state $|S_i\rangle$ from

Ens. ID	$(\frac{L}{a})^3 \times \frac{T}{a}$	β	am_l	am_s	c_{SW}	a (fm)	M_π (MeV)	$M_\pi L$	L (fm)	Total Lattices
$a117m310$	$32^3 \times 96$	6.1	-0.2850	-0.2450	1.249310	0.117	310	5.85	3.7	4865
$a087m290$	$32^3 \times 64$	6.3	-0.2390	-0.2050	1.205366	0.087	289	4.1	2.8	3085
$a087m290L$	$48^3 \times 128$	6.3	-0.2390	-0.2050	1.205366	0.087	289	6.16	4.2	6223
$a087m230$	$48^3 \times 128$	6.3	-0.2415	-0.1974	1.205366	0.087	233	5.0	4.2	5200
$a087m230X$	$48^3 \times 128$	6.3	-0.2406	-0.2050	1.205366	0.087	228	5.0	4.2	3167
$a086m180$	$48^3 \times 96$	6.3	-0.2416	-0.2050	1.205366	0.086	179	3.7	4.1	3248
$a086m180L$	$64^3 \times 128$	6.3	-0.2416	-0.2050	1.205366	0.086	179	5.1	5.5	6622
$a068m290$	$48^3 \times 128$	6.5	-0.2070	-0.1750	1.170082	0.068	290	4.18	3.3	7620
$a068m230$	$64^3 \times 192$	6.5	-0.2080	-0.1788	1.170082	0.068	234	5.2	4.4	3604
$a068m175$	$72^3 \times 192$	6.5	-0.2091	-0.1778	1.170082	0.068	175	4.4	4.9	5556
$a067m135$	$96^3 \times 192$	6.5	-0.2095	-0.1793	1.170082	0.067	135	4.4	6.4	2904
$a053m295$	$64^3 \times 192$	6.7	-0.1830	-0.1650	1.142727	0.053	295	4.8	3.4	5301
$a053m230$	$72^3 \times 192$	6.7	-0.1843	-0.1640	1.142727	0.053	226	4.5	3.8	3331

TABLE I. Parameters of the thirteen isotropic 2+1-flavor Wilson-clover ensembles generated by the JLab/W&M/LANL/MIT/Marseille collaborations using the highly tuned CHROMA code[20]. The acceptance rate in the HMC algorithm was tuned to roughly 92% on each ensemble. The bare light and strange quark masses are given by $am_{l,s} = 1/2\kappa_{l,s} - 4$ where κ is the hopping parameter in the SW action with the coefficient of the clover term given by $c_{SW} = 1/u_0^3$. The last five columns give the approximate lattice spacing a in fermi, the pion mass M_π in MeV, the lattice size L in fermi, its dimensionless version $M_\pi L$, and the total number of configurations available for analysis. The additional L in $a087m290L$ and $a086m180L$, implies a larger volume. Ensembles $a087m230$ and $a087m230X$ differ mainly in the value of the strange quark mass. The ensemble IDs used here are updates from those used in Refs. [3–6] to reflect the new values of the lattice spacing a , M_π and M_K obtained in this analysis. Updates of results presented in Refs. [5, 6] are under progress.

ID	β	a (fm)	M_π (MeV)	M_K (MeV)	N_{KG}	σ	R_{RMS}/a	# Lattices Analyzed	N_{HP}	N_{LP}	τ
$a117m310$	6.1	0.117	310(6)	517(10)	50	5	4.10(1)	3004	12,056	385,792	{8, 10, 12, 14}
$a087m290$	6.3	0.087			91	7	5.46(2)	2469	7,407	237,024	{10, 12, 14, 16}
$a087m290L$	6.3	0.087	289(5)	550(10)	91	7	5.49(3)	5453	18,040	577,280	{10, 12, 14, 16, 18}
$a087m230$	6.3	0.087	233(4)	585(11)	98	7	5.54(1)	2668	8,000	256,000	{10, 12, 14, 16, 18}
$a087m230X$	6.3	0.087	228(4)	534(10)	98	7	5.56(1)	2003	8,024	256,768	{10, 12, 14, 16, 18}
$a086m180$	6.3	0.086			91	7	5.41(2)	4012	16,048	513,536	{8, 10, 12, 14, 16}
$a086m180L$	6.3	0.086	179(3)	523(10)	91	7	5.49(3)	4014	20,000	640,000	{8, 10, 12, 14, 16}
$a068m290$	6.5	0.068	290(5)	614(11)	150	9	6.96(1)	5295	18,880	604,160	{11, 13, 15, 17, 19}
$a067m230$	6.5	0.067	234(4)	568(10)	200	10	7.53(1)	2350	14,100	225,600	{13, 15, 17, 19, 21}
$a067m175$	6.5	0.067	175(3)	567(10)	185	10	7.57(2)	3771	22,632	362,112	{13, 15, 17, 19, 21}
$a067m135$	6.5	0.067	135(3)	548(10)	200	10	7.57(1)	2500	15,000	240,000	{13, 15, 17, 19, 21}
$a053m295$	6.7	0.053	295(5)	553(10)	365	14	10.09(1)	3250	16,200	259,200	{15, 18, 21, 24, 27}
$a053m230$	6.7	0.053	226(4)	550(10)	392	14	10.18(1)	2485	15,300	244,800	{18, 21, 24, 27, 30}

TABLE II. The approximate value of the lattice spacing a used to label the ensembles is taken from Table XIV. The large errors in M_π and M_K are mainly due to those in a . Columns 6 and 7 give the Wuppertal smearing parameters $\{N_{KG}, \sigma\}$ used to construct the smeared sources for generating the quark propagators. The resulting root mean squared smearing radius in lattice units, R_{RMS}/a , is given in column 8. Column 9 gives the number of configurations analyzed. The numbers N_{HP} (N_{LP}) give the total number of high (low) precision measurements made. The connection between these numbers to the data given in Table III is—on each configuration N_{tsrc} maximally separated time slices were selected randomly, and on each time slice N_{src}^{LP} points were selected randomly as sources for low-precision quark propagators and one for high-precision. For completeness, the last column gives the values of source-sink separation τ used in the calculations of 3-point functions to be presented elsewhere.

the vacuum. (See Appendix E for definitions of the operators used.) The sum is over all states with the quantum numbers of \mathcal{O} as one does not, *a priori*, know which amplitudes are non-zero. The quark line diagrams representing the two-point functions for meson and baryon states are shown in Fig. 1. These are constructed by contracting the free spin, color and flavor indices in the non-perturbative Feynman quark propagator P_F (the lines) with the quark fields in \mathcal{O} (the blobs), i.e., by taking appropriate spin and color traces. The gluon lines are shown only to indicate that all possible interactions (with momenta allowed by the lattice cutoff $1/a$) are included. Calculations of the correlation functions represented by these quark-line diagrams are fully non-perturbative.

The quark propagator $P_F \equiv \mathcal{D}^{-1}$ is the inverse of the lattice Dirac operator \mathcal{D} . This inverse (used in both the construction of correlation functions, and in the generation of the lattices) is calculated by solving the equation $P_F|_{j,b}^{i,a} = \mathcal{D}^{-1}|_{j,b}^{k,c} \xi_{k,c}^{i,a}$ using the efficient multi-grid algorithm [20–22] built into the CHROMA software package [7]. The Gaussian smeared source $\xi_{k,c}^{i,a}$ is produced by applying the Wuppertal procedure on a delta-function source [3, 23–25] with smearing parameters N_{KG} and σ given in Table II. To make these smeared sources smooth, the gauge links were first smoothed using twenty hits of the stout algorithm with the sum of the spatial staples added to the link with a weight factor $\rho = 0.08$ [12]. The resulting root-mean-square size of the smearing, $\sqrt{\int dr r^4 S^\dagger S / \int dr r^2 S^\dagger S}$ with $S(r)$ the value of the smeared source at radial distance r , is between 0.5–0.57 fm (Table II).

These quark propagators can be similarly smeared at the sink points, and using these we calculate two types of 2-point functions: the smeared-smeared (SS) using propagators with the same smearing at the source and sink points, and smeared-point (SP) using unsmeared (point) propagators at the sink. Analyzing both using Eq. (3) provided checks on excited state contributions and increased the confidence in the extraction of the ground-state energy M_0 (see Figs. 20, 21, 22 and 23 in Appendix D for the baryon states). By construction, all two-point correlation functions studied are gauge invariant, so no gauge fixing of the lattices is required in their calculation.

For the spectral quantities studied in this work, the goal is to extract the ground-state mass M_0 and the amplitude A_0 . This is achieved in two ways: (i) analyzing $\Gamma_2(\tau)$ at large τ at which ground state domination is manifest, i.e., a long and stable plateau in $M^{\text{eff}}(\tau)$ that, ideally, stretches to $\tau \rightarrow \infty$. Clear examples of this are the pseudoscalar states for which there is no degradation of the signal with τ as shown in Figs. 12 and 13. (ii) For the remaining states, such as all vector mesons and baryons, for which the signal decays exponentially (as $e^{-(M_N - 1.5M_\pi)}$ for nucleons as explained in [26–28]), the plateau with current statistics are not sufficiently long. So we make fits to Eq. (3) truncated at $i = 2, 3, 4$ states

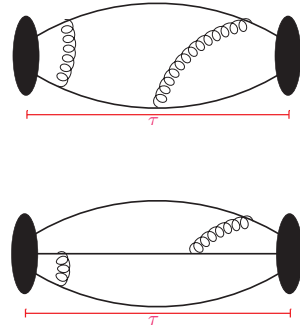


FIG. 1. Quark line diagrams for meson (top) and baryon (bottom) two-point functions. The gluon lines have been added only to remind the reader that all possible intermediate states and gluon exchanges are included in lattice calculations, i.e., they are fully non-perturbative.

depending on the statistical precision of the data. The effects of this truncation are studied using the nucleon state for which, among baryons, the highest statistical precision data was collected (see Appendix D).

The quantities extracted from the analysis of the two-point functions include

- The pseudoscalar masses, M_π , M_K , and $M_{s\bar{s}}$, given in Table IV.
- The pseudoscalar decay constants, f_π and f_K , given in Table V.
- The vector meson masses, M_ρ , M_{K^*} , and $M_{\phi_{s\bar{s}}}$, given in Table VI.
- The masses of octet baryons, M_N , M_Σ , M_Λ and M_Ξ , given in Table VII.
- The masses of decuplet baryons, M_Δ , M_{Σ^*} , M_{Ξ^*} and M_Ω , given in Table VIII.

In addition, we present data for the flow time scales w_0 and t_0 in Table III, and for the topological charge Q and the Weinberg three-gluon operator W as a function of the flow time in Appendix B. The prescription for implementing the flow and the calculation of w_0 , t_0 and the topological susceptibility χ_Q is given in Secs. II and III.

Lastly, Table XI gives the renormalization factors in the $\overline{\text{MS}}$ scheme at scale $\mu = 2$ GeV for all five quark bilinear local operators for the 11 ensembles. Their calculation, using the regularization independent symmetric momentum subtraction (RI-sMOM) intermediate scheme on the lattice [29, 30], is described in Sec. IV A. The matching between the RI-sMOM and $\overline{\text{MS}}$ schemes and the running in the continuum use results from continuum perturbation theory, whose evaluation requires knowing the lattice scale a and $\alpha_s(1/a)$ on each ensemble. Results for these are given in Table XIV and their extraction is discussed in Sec. IV C.

Ens. ID	Streams:	Traj	Configs	t_0/a^2	w_0/a	N_l	N_s	N_{tsrc}	N_{src}^{LP}	N_{bin}
	0: 1000–2108									
<i>a117m310</i>	a: 1010–1870	4865	1.4953(44)	1.3880(29)		3004	1013	4	32	5
	b: 1000–18340									
<i>a087m290</i>	0: 2–13340	3335	2.6566(59)	1.8709(45)		2469	0	3	32	4
<i>a087m290L</i>	0: 262–25154	6223	2.6517(13)	1.86770(75)		5453	944	4	32	5
<i>a087m230</i>	a: 0–12154	5200	2.65879(73)	1.86580(52)		2668	1001	4	32	4
	b: 660–9244									
<i>a087m230X</i>	0: 0 – 12670	3167	2.7079(14)	1.89853(90)		2003	2003	4	32	4
	0: 10–5410									
	a: 0–3560									
	b: 0–3720									
<i>a086m180</i>	c: 0–3276	6634	2.7442(30)	1.9187(19)		3941	0	4	32	5
	d: 40–2810									
	e: 40–2180									
	f: 40–3330									
	g: 40–2420									
	0: 2–6896									
<i>a086m180L</i>	a: 2–5838	6622	2.74588(76)	1.91977(44)		4014	1014	5	32	4
	b: 2–6970									
	c: 2–6776									
	0: 800–7638									
<i>a068m290</i>	a: 10–6612	7620	4.3619(38)	2.4115(19)		5295	819	4	32	5
	b: 10–17028									
<i>a068m230</i>	0: 0–12150	3604	4.4779(18)	2.46372(95)		2350	500	6	16	5
	a: 802–3068									
	0: 0–5640									
<i>a068m175</i>	a: 2–4354	5556	4.5158(11)	2.48351(68)		3771	1273	6	16	4
	b: 2–4072									
	c: 2–5508									
<i>a067m135</i>	0: 0–6400	2904	4.5620(10)	2.50490(61)		2500	1760	6	16	4
	a: 0–5210									
	0: 336–10536									
<i>a053m295</i>	a: 100–5624	5301	7.1233(41)	3.1304(18)		3250	550	6	16	5
	b: 100–5376									
<i>a053m230</i>	0: 2–11306	3331	7.1904(55)	3.1616(25)		2485	2035	6	16	5
	a: 802–2816									

TABLE III. The number of streams and thermalized trajectories (Traj) generated using the HMC algorithm and the number of configurations (Configs) stored at Oak Ridge. Neglecting lattices lost, every second trajectory is stored and measurements were made on configurations mostly separated by four trajectories (6 for the rest). Columns four and five give the measured values of the flow parameters t_0/a^2 and w_0/a . N_l gives the number of lattices analyzed for observables consisting of only light quarks (M_π , f_π , M_ρ , M_N and M_Δ), while N_s gives the number for observables with at least one strange quark (M_K , f_K , $M_{s\bar{s}}$, M_Σ , M_Ξ , M_{Σ^*} , M_{Ξ^*} , M_Ω). On each configuration, N_{tsrc} is the number of maximally separated time slices on which sources were placed and N_{tsrc}^{LP} is the number of randomly selected sources points on each of these time slices from which low-precision (LP) measurements are made for a total of $N_{src}^{LP} \times N_{tsrc}$ measurements. The high-precision measurements are N_{tsrc} , i.e., only one point on each of the N_{tsrc} time slices was used. The last column gives the number of adjacent configurations, N_{bin} , over which data were binned and averaged to construct the binned data used for the statistical analysis.

C. Neglecting Finite Volume Corrections

The two smaller volume ensembles, $a087m290$ and $a086m180$, were generated to evaluate finite volume corrections by comparing with results from their larger volume versions, $a087m290L$ and $a086m180L$. As shown in Tables IV and VII, the errors on M_π and M_N from the smaller volume lattices are much larger, and within these errors, the two values for M_π and M_N overlap. Noting this lack of resolution, we did not calculate any quantity involving strange quarks on these two ensembles. They are, therefore, not included in the analysis. The remaining eleven ensembles have $M_\pi L \geq 4$ and $L > 3.4$ fm. On such large lattices, the finite volume corrections are expected to be exponentially suppressed [31] and smaller than the statistical errors for both the pseudoscalar mesons and the baryons. A more detailed study of finite volume effects presented in Ref. [32], with lattice parameters covering those simulated here, reached the same conclusion. We, therefore, neglect finite volume corrections in our analyses, i.e., the fits used to get the physical point values include only chiral-continuum (CC) corrections.

D. The Quality of the Signal

The number of measurements made for all quantities with one or more strange quark are much fewer. Specifically, as shown in Table III, note the difference between N_l versus N_s configurations used and $N_{tsrc} \times N_{src}^{LP}$ versus N_{tsrc} source points used for measuring correlation functions composed of light quarks only versus those with one or more strange quarks. Nevertheless, the signal in two-point functions with even one strange quark is reasonable as shown in Figs. 22 and 23 in Appendix D.

A necessary input in the calculation of the statistical errors is knowing the autocorrelation time for each observable. We assess the integrated autocorrelation time (ICT), defined in Eq. (C3), using the data for t_0/a^2 and w_0/a as these long-distance quantities show the largest correlations. Note that these data, presented in Table XIX and shown in Appendix C, exhibit (i) significant variations in ICT between the various streams employed in lattice generation and (ii) an increase as $a \rightarrow 0$. To take into account these significant ICT we bin the data. Specifically, all two-point function data are first averaged over the $N_{tsrc} \times N_{src}^{LP}$ (or N_{tsrc} for strange) measurements made on a given configuration, and these averages are further binned over N_{bin} (given in Table III) configurations. These binned data do not show any significant autocorrelations. Therefore, the errors coming out of the analysis of the binned data are not augmented by the ICT determined from t_0/a^2 or w_0/a .

The signal-to-noise (S2N) ratio is widely different for the pseudoscalar mesons versus vector mesons and the baryons. For both the ρ -meson and the nucleons, low lying multihadron states give rise to significant contribu-

tions and an exponentially decaying signal [26–28], a well-known persisting challenge to their analysis.

The main tool used to assess the S2N ratio for the various hadrons are the effective mass plots: $aM^{\text{eff}}(\tau) = \log(\Gamma_2(\tau)/\Gamma_2(\tau + 1))$ versus τ where $\Gamma_2(\tau)$ is the two-point function at time separation τ as defined in Eq. (3). To qualify for a robust signal, we require a long plateau in $aM^{\text{eff}}(\tau)$ indicating that ground state domination has been achieved. A qualitative overview of the signal in the various channels is

- The signal in all two-point functions for pseudoscalar mesons is excellent. There is no S2N degradation with τ , i.e., the plateau in the $M^{\text{eff}}(\tau)$ extends to all τ . Final values for the masses M_π , M_K and $M_{s\bar{s}}$ are given in Table IV, and for the decay constants, f_π and f_K , extracted from the amplitudes A_0 in Table V. The latter are extracted from a simultaneous fit to $P_S(0)P_S(\tau)$ and $P_S(0)\bar{A}_P(\tau)$ two-point correlation functions where $P = \bar{\psi}\gamma_5\psi$ and $A = \bar{\psi}\gamma_4\gamma_5\psi$ are the pseudoscalar and axial vector interpolating operators, with the source placed at time $t = 0$ and sink at time $t = \tau$. The subscript S denotes smeared and P point sources. The signal-to-noise (S2N) ratio in these quantities is approximately $O(10^3)$. See Sec. IV for their analysis and the plots for aM_{eff} for the pion in Appendix A.
- Estimates of vector meson masses are given in Table VI, however, the signal for the ρ meson is poor (there is no credible plateau in $M^{\text{eff}}(\tau)$ with single ρ operator) while that for the K^* and $\phi_{s\bar{s}}$ states is reasonable. The multihadron $\pi\pi$ intermediate state afflicts the signal in the ρ correlator, with the S2N decaying as $e^{-(M_\rho - m_\pi)\tau}$, whereas the situation for K^* ($\phi_{s\bar{s}}$) is better because of the much heavier $K\pi$ (KK) intermediate state. To get a good signal for the rho meson, the method of choice is to use a variational ansatz for the interpolating operator [33–36]. This has not been implemented in this work. Given the lack of a good signal and because these states have strong decays and large widths, we do not present an analysis of their data.
- The signal in all four octet baryon states, $\{N, \Lambda, \Sigma, \Xi\}$, is similar and good. The S2N for the nucleon degrades as $e^{-(M_N - 1.5m_\pi)\tau}$ due to the variance being dominated by the light three-pion state [26–28]. A second, related, problem that impacts extracting the ground state properties of nucleons from fits to the spectral decomposition given in Eq. (3) are the towers of multi-hadron excited states beginning with the $N(\vec{p})\pi(-\vec{p})$ states, with the lowest having a mass gap smaller than the radial state $N(1440)$. Again, the S2N is better for the states with strange quarks, (Λ, Σ, Ξ) , as the lowest multihadron states are expected to be $KK\pi$ or $\phi_{s\bar{s}}\pi\pi$ or $\phi_{s\bar{s}}KK$.

To further understand the signal, we have collected two-point data for a number of local interpolating operators defined in Table XX and measured both smeared-smeared (SS) and smeared-point (SP) correlation functions. Data for M_{eff} are shown in Figs. 12–13 (pion); Figs. 20–21 (nucleon); and Figs. 22 and 23 (the five baryon states).

The widths of $\{\Lambda, \Sigma, \Xi\}$ states are small as they decay only via weak interaction, and isospin breaking corrections are also small, i.e., a few MeV. We, therefore, consider it appropriate to compare, after chiral-continuum extrapolation, the lattice results given in Table VII with the experimental values for the 2+1-flavor QCD given in Eq. (7). This is done in Table XVIII.

- For the decuplet baryons, a credible plateau in the effective mass plot at large τ is found only for the Ω state. The S2N ratio for it is comparable to that for the Λ , Σ , and Ξ octet states. (These four states have the same number of smaller measurements, i.e., fewer configurations and only HP source points, compared to the nucleon.) In addition, the Δ , Σ^* , and Ξ^* have strong decays and their experimental masses have large widths. Thus, to do a proper study of their masses, one needs to relate the resonance parameters to the spectrum in a finite box. This requires calculating correlation functions with a much larger basis of operators including baryon-meson ones. This is beyond the scope of this work. Our analysis of the decuplet baryons is, therefore, based on the data for only the Ω baryon even though, for completeness, we give estimates for aM_Δ and aM_{Σ^*} in Table VIII. Data for aM_{Σ^*} were, unfortunately, collected on only two ensembles due to an oversight.
- The data for the flow time scales w_0 and t_0 is very precise with a S2N ratio of approximately $O(10^3)$.
- The time history of Q and W presented in Appendix B show no freezing of topology in any of the ensembles, and auto-correlations at even large flow times are small. The topological susceptibility χ_Q on each ensemble is extracted with a S2N ratio of approximately $O(10^2)$.

The largest auto-correlations are observed in the flow variables t_0 and w_0 , which are listed in Table XIX and shown in Figs. 12–13 in appendix C. Binned data, as described above, for meson and baryon two-point functions used in the analysis do not show any significant auto-correlations. Consequently, we do not augment the statistical errors coming out of the analysis based on the ICT observed in the t_0 and w_0 data.

For the quantities with a good S2N, the largest source of uncertainty in the final results is due to the chiral-continuum fits used to extrapolate the lattice data in the quark masses and to the continuum limit. In all cases

where data from multiple operators or correlation functions are available, the final results are obtained using an average weighted by their Akaike Information Criteria score (AIC) [37].

E. The chiral-continuum extrapolation

To obtain the physical point values, i.e., at $M_\pi = 135$ MeV, $M_K = 495$ MeV, $a = 0$ and $L = \infty$, we need to specify the extrapolation ansatz used to address the chiral, continuum and finite volume corrections. While detailed descriptions will be provided in appropriate sections later, here we summarize the overall approach.

The input parameters characterizing each of these 2+1-flavor isospin symmetric ensembles are four: the lattice spacing a (or equivalently the gauge coupling $\beta = 6/g^2$), the light and strange quark masses, m_l and m_s , and the spatial lattice size L . These are given in Table I. The intent during lattice generation was to tune the strange quark mass to roughly its physical value on each ensemble so as to reduce the number of free parameters to three. Unfortunately, the output kaon masses listed in Table II vary between 520 – 615 MeV. Therefore, the analysis of these 2 + 1-flavor ensembles is carried out keeping M_π and M_K (equivalently m_l and m_s) as independent parameters. In the chiral fits, we use, instead of the quark masses, the pion and kaon masses expressed in units of the flow variable t_0/a^2 defined in Eq. (10), i.e.,

$$\phi_2 \equiv 8t_0M_\pi^2 = 8(t_0/a^2)(aM_\pi)^2, \quad (4)$$

and the SU(3) symmetric mass parameter

$$\begin{aligned} \phi_4 &\equiv 8t_0(M_K^2 + M_\pi^2/2) \\ &= 8(t_0/a^2)[(aM_K)^2 + (aM_\pi)^2/2]. \end{aligned} \quad (5)$$

The location of the 11 ensembles in the $\phi_2 - \phi_4$ plane is shown in Fig. 2. The measured values of t_0/a^2 and w_0/a are given in Table III.

We also carry out the full analysis using w_0/a , defined in Eq. (11), to construct dimensionless quantities as in Eqs. (4) and (5). Note, however, these two analyses (using t_0/a^2 versus w_0/a) are highly correlated. This is manifest from the results for the ratio f_K/f_π in Table XV, and the chiral fit parameters for baryons in Table XVI.

The chiral analysis of pseudoscalar mesons uses results from meson chiral perturbation theory (χ PT) [38–40], while for baryons, results from heavy baryon χ PT (HB χ PT) are used [41, 42]. On comparing outputs of next-to-leading order (NLO) and next-to-next leading order (NNLO) truncations, one of our main conclusions is that the NLO ansatz is not sufficient to fit the masses of the octet baryons.

The analysis of discretization errors uses the fact that the Wilson-clover fermion action we use is almost, but not fully, $O(a)$ improved. We, therefore, investigate discretization errors using three ansatz modeling the leading-order correction, $O(a)$ or $O(\alpha_s a)$ or $O(a^2)$. In

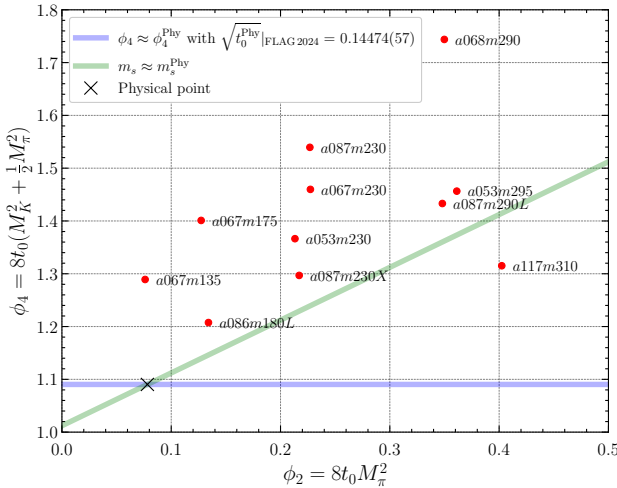


FIG. 2. Overview of the 11 ensembles in the $\phi_2 - \phi_4$ plane. The blue line corresponds to the choice $\phi_4 = \phi_4^{\text{Phy}}$, while the green line corresponds to $\phi_4 = 4t_0^{\text{Phy}}[2(M_K^{\text{Phy}})^2 - (M_\pi^{\text{Phy}})^2] + \phi_2$. Since $m_s \propto 2M_K^2 - M_\pi^2$ in leading order chiral perturbation theory, the strange-quark mass remains close to its physical value on the green line. The two lines intersect at the physical point (black cross), where the pion and kaon have their physical masses.

most cases, the three sets of results overlap. Using any two terms together results in overparameterization.

Lastly, as already stated in Sec. I C, our data are not extensive enough to resolve finite volume corrections. So we ignore them and restrict the analysis to CC fits to data from eleven ensembles that all have $M_\pi L > 4.0$.

F. Main Results

Using the data simulated and the various fit ansatz, we present results for the following quantities:

- Time history for the topological charge Q and Weinberg operator W . Data presented in Appendix B show no evidence of freezing of Q or W on any of the 13 ensembles.
- The topological susceptibility χ_Q in the continuum limit calculated in Sec III.
- The flow scales t_0^{Phy} and w_0^{Phy} extracted using chiral-continuum fits to $\sqrt{8t_0}f_{\pi K} \equiv \sqrt{8t_0}(2f_K + f_\pi)/3$. Because the isovector renormalization constant Z_A has no dependence on the lattice scale, fits to $f_{\pi K}$ involve only dimensionless variables that have all been calculated on the lattice as discussed in Sec. IV B.
- Using the value of t_0^{Phy} (or w_0^{Phy}) extracted from either the fit to our $f_{\pi K}$ data or using the FLAG 2024 values, we calculate the ratio, f_K/f_π , of pseudoscalar decay constants in Sec. IV D.

- A fit to the octet baryon data versus ϕ_2 and ϕ_4 is used to extract second estimates of t_0^{Phy} and w_0^{Phy} in Sec. V A. A comparison of results using the NLO versus NNLO ansatz for the chiral behavior of the octet masses, shows that the NNLO ansatz is preferred.

- The NLO and the NNLO fits to the Ω baryon mass versus ϕ_2 and ϕ_4 , are comparable and NNLO is likely an overparameterization as presented in Sec. V B. These fits give a third estimate for t_0^{Phy} and w_0^{Phy} .

- Various estimates of t_0^{Phy} and w_0^{Phy} are summarized and compared in Table XVII and in Fig. 10.

- The lattice spacing a , the coupling $\alpha_s(1/a)$, and the renormalization constants for quark bilinear local operators, Z_Γ , on each ensemble. The analysis of some of the spectral quantities presented in this paper do not require knowing the lattice scale a on each ensemble. It is, however, needed when calculating (i) any quantity that has a scale dependence, for example matrix elements requiring scale-dependent renormalization constants, i.e., Z_Γ specified in the continuum $\overline{\text{MS}}$ scheme at 2 GeV; or (ii) the analysis involves, explicitly, a mass scale in physical units such as we will encounter in the chiral logarithms in the analysis of f_K/f_π . To facilitate these scale dependent calculations, we discuss scale setting in Sec. IV C.

G. Input Values of Physical Quantities

Throughout this paper, when physical values for the spectrum or decay constants are needed, we take the numbers given in Ref. [32] that have been corrected for the isospin-breaking effects:

$$\begin{aligned}
 M_\pi^{\text{Phy}} &= 134.8(3) \text{ MeV}, \\
 M_K^{\text{Phy}} &= 494.2(3) \text{ MeV}, \\
 f_\pi^{\text{Phy}} &= 130.56(13) \text{ MeV}, \\
 f_K^{\text{Phy}} &= 157.2(5) \text{ MeV}, \\
 f_{\pi K}^{\text{Phy}} &\equiv (2f_K + f_\pi)/3 = 148.32(34) \text{ MeV}, \\
 M_N^{\text{Phy}} &= 937.54(6) \text{ MeV}, \\
 M_\Lambda^{\text{Phy}} &= 1115.68(1) \text{ MeV}, \\
 M_\Sigma^{\text{Phy}} &= 1190.66(12) \text{ MeV}, \\
 M_\Xi^{\text{Phy}} &= 1316.9(3) \text{ MeV}, \\
 M_\Omega^{\text{Phy}} &= 1669.5(3.0) \text{ MeV}.
 \end{aligned} \tag{6}$$

In addition, we will use the following FLAG 2024 averages for the 2+1-flavor theory [43]:

$$\begin{aligned}
 \sqrt{t_0^{\text{Phy}}} \big|_{\text{FLAG}} &= 0.14474(57) \text{ fm}, \\
 w_0^{\text{Phy}} \big|_{\text{FLAG}} &= 0.17355(92) \text{ fm}.
 \end{aligned} \tag{7}$$

II. GRADIENT FLOW AND THE SCALES t_0 AND w_0

The gradient flow is a procedure for smoothing of gauge degrees of freedom (links matrices) that provides an ultraviolet scale characterizing lattice ensembles [44]. The continuum limit of quantities calculated on the lattice can then be taken holding this scale fixed in physical units, say MeV. The smoothing procedure evolves the gauge fields in the flow time t_{gf} according to a gauge-covariant diffusion equation towards static points of the lattice action. It involves updating each gauge link at site i in direction μ in flow time t_{gf} using

$$\frac{dV(t_{gf})_{i,\mu}}{dt_{gf}} = -g_0^2 \frac{\partial S(V)}{\partial V_{i,\mu}} V_{i,\mu}, \quad V_{i,\mu}(0) = U_{i,\mu}. \quad (8)$$

In this work, we employ the stout smearing process [12],

$$U_\mu^{(n+1)}(x) = \exp(-i\rho Q_\mu(x)) U_\mu^{(n)}(x), \quad (9)$$

that, for small ρ , has been shown to be equivalent to the Wilson flow scheme in Refs. [44, 45]. Here Q_μ is the sum of the 6 staples in planes orthogonal to the direction μ . The parameter ρ serves as the small flow step size, δt , which we choose to be $\delta t = 0.01$. This procedure ensures a gauge-covariant smoothing procedure with well-understood continuum behavior.

To calculate the scale t_0 , the infinitesimal gauge-field smearing steps are performed up to a flow time t_{gf} at which the product of the energy density and the square of the flow time reaches the predefined value

$$t_{gf}^2 E(t_{gf})|_{t_{gf}=t_0} = 0.3. \quad (10)$$

A second scale, w_0 , is obtained using the condition,

$$t_{gf} \frac{d}{dt_{gf}} \{t_{gf}^2 E(t_{gf})\} \Big|_{t_{gf}=w_0^2} = 0.3. \quad (11)$$

The resulting values of t_0 and w_0 for the 13 ensembles are given in Table III. Either quantity, t_0 or w_0 , can be used to set the scale of the unflowed lattice configurations as discussed in Sec. IV C.

III. THE θ AND WEINBERG OPERATORS

Our long-term interest in calculating the CP symmetry violating topological charge Q and the dimension-six Weinberg operator W is to determine their contribution to the nucleon electric dipole moment (nEDM). To remove lattice artifacts, we calculate them as a function of the Wilson flow as it provides a gauge-covariant smoothing of the gauge field and suppresses ultraviolet fluctuations while preserving the topological properties. Using the gluonic field strength tensor $G_{\mu\nu}(x, t_{gf})$ at flow time τ , the topological charge Q is given by

$$Q(t_{gf}) = \int d^4x \frac{1}{32\pi^2} \epsilon^{\mu\nu\rho\sigma} \text{Tr}[G_{\mu\nu}(x, t_{gf}) G_{\rho\sigma}(x, t_{gf})], \quad (12)$$

and the dimension-six Weinberg charge W by

$$W(t_{gf}) \equiv \int d^4x \epsilon^{\rho\mu\eta\sigma} \text{Tr}[G_{\mu\nu}(x, t_{gf}) G_{\nu\rho}(x, t_{gf}) G_{\eta\sigma}(x, t_{gf})]. \quad (13)$$

In the absence of lattice artifacts, the topological charge should be integer valued on each configuration. In our data, this convergence is not reached at even the largest flow time simulated. However, as shown in the panels on the left in Figs. 14–17, the distribution of Q stabilizes at relatively early flow time. Fortunately, as discussed in Ref. [46], the property relevant for reliably extracting the topological susceptibility and the correlation of Q or W with nucleon n -point functions needed to calculate their contribution to the nEDM is the stabilization of the distribution as shown in Figs. 14 and 17.

In this work we analyze only the renormalization group invariant topological susceptibility,

$$\chi_Q \equiv \langle \int d^4x Q(x) Q(0) \rangle \equiv \frac{1}{V} \langle Q^2 \rangle \quad \text{with} \quad \langle Q \rangle = 0. \quad (14)$$

since our calculation of the renormalization constant for W , which has a power divergent mixing with Q , is not yet complete.

In Fig. 3, we plot the dimensionless quantity $(t_0^2/a^4)(a^4\chi_Q)$ as a function of the flow time $(t_0/a^2)(a^2/t_{gf})$ for the eleven ensembles.

Variation with the flow time t_{gf} is a lattice artifact that, on each ensemble, is removed by fitting χ_Q versus t_{gf} using the ansatz

$$t_0^2 \chi_Q = c_0 + c_1 a^2 / t_{gf} + c_2 (a^2 / t_{gf})^2. \quad (15)$$

This ansatz suffices (without overparameterization) for all eleven ensembles as shown in Fig. 3. The asymptotic values and the χ^2/dof of the fits are given in Table IX. Assuming finite volume corrections can be neglected, these numbers are then extrapolated to the chiral-continuum limit using a second order polynomial ansatz

$$\begin{aligned} t_0^2 \chi_Q = & c_1 \frac{a^2}{t_0} + c_2 \phi_2 + c_3 \phi_2^2 + c_4 \phi_2^2 / \phi_4 \\ & + c_5 \phi_2 \frac{a^2}{t_0} + c_6 \phi_2 \phi_4, \end{aligned} \quad (16)$$

that incorporates the requirement that the susceptibility χ_Q must vanish in the chiral-continuum limit. Possible discretization effects at finite lattice spacing a are modeled by the term $c_1 \frac{a^2}{t_0}$. Note that, throughout, this analysis is in terms of dimensionless quantities $t_0^2 \chi_Q$, a^2/t_0 (given in Table III), $\phi_2 \equiv 8t_0 M_\pi^2$ and $\phi_4 \equiv 8t_0 (M_K^2 + M_\pi^2/2)$ that are calculated explicitly on the lattice and do not require knowledge of the lattice scale a of each ensemble.

Once the c_i are determined, Eq. (16) is evaluated at $a = 0$, $M_\pi = 135$ MeV and with t_0 set to the already calculated t_0^{phy} to get χ_Q^{phy} for the eleven models given

Ens. ID	aM_π	aM_K	$aM_{s\bar{s}}$	M_K/M_π	$M_{s\bar{s}}/M_\pi$
$a117m310$	0.18341(26)(1)	0.30516(45)(10)	0.38968(40)(5)	1.6621(47)	2.1226(54)
$a087m290$	0.1279(4)				
$a087m290L$	0.12809(8)(1)	0.24362(25)(3)	0.32095(21)(2)	1.9004(41)	2.5030(51)
$a087m230$	0.10327(14)(0)	0.25893(27)(7)	0.35264(24)(1)	2.489(10)	3.391(14)
$a087m230X$	0.10010(15)(3)	0.23421(20)(4)	0.31630(14)(7)	2.3402(55)	3.1612(71)
$a086m180$	0.0781(2)				
$a086m180L$	0.07812(11)(1)	0.22786(30)(1)	0.31302(26)(0)	2.940(13)	4.040(17)
$a068m290$	0.10013(6)(3)	0.21204(29)(6)	0.28461(21)(5)	2.1149(65)	2.8383(82)
$a068m230$	0.07966(6)(1)	0.19385(31)(0)	0.26384(26)(12)	2.4295(71)	3.3079(82)
$a068m175$	0.05938(8)(2)	0.19240(19)(5)	0.26717(14)(2)	3.246(11)	4.502(15)
$a067m135$	0.04567(7)(4)	0.18515(16)(1)	0.25902(13)(2)	4.067(13)	5.691(18)
$a053m295$	0.07962(6)(3)	0.14963(33)(12)	0.19765(29)(2)	1.8949(53)	2.5017(64)
$a053m230$	0.06088(6)(4)	0.14799(13)(10)	0.20148(10)(14)	2.4323(44)	3.3098(56)
Physical				3.667	5.089

TABLE IV. Results for pseudoscalar masses in lattice units. These values are obtained from weighted averages over two-state fits to SS and SP correlators. The first error is the overall analysis error and the second, a systematic error, is estimated from the difference between SS and SP values. The strange spectrum, M_K and $M_{s\bar{s}}$, is computed on only a subset of the configurations (see Table III for the number of configurations analyzed) and using only the N_{HP} measurements given in Table II, however, the fractional error in them is comparable to that in M_π . Mass ratios are given in the two columns on the right. The "physical" values of the ratios are with $M_\pi = 135$ MeV, $M_K = 495$ MeV, and $M_{s\bar{s}} = 686$ MeV. The latter is estimated using χ PT and the Gellmann-Oakes-Renner relation. The plots for the effective mass, aM_{eff}^π , are shown in Figs 12 and 13.

Ens. ID	i	aM_π	aM_K	af_π	af_K
$a117m310$	1	0.18343(27)	0.30518(40)	0.10057(14)	0.11097(32)
	2	0.18351(26)	0.30527(39)	0.100656(96)	0.11112(30)
$a087m230$	1	0.10315(13)	0.25894(23)	0.07139(25)	0.08387(23)
	2	0.10315(15)	0.25896(23)	0.07136(16)	0.08388(22)
$a087m230X$	1	0.10013(14)	0.23430(16)	0.069820(78)	0.08096(17)
	2	0.10021(14)	0.23427(18)	0.069887(66)	0.08096(18)
$a087m290L$	1	0.128067(80)	0.24375(21)	0.073575(44)	0.08338(22)
	2	0.128176(75)	0.24366(25)	0.073668(31)	0.08340(25)
$a086m180L$	1	0.07808(12)	0.22794(24)	0.067116(51)	0.07894(18)
	2	0.07817(11)	0.22787(28)	0.067153(42)	0.07888(21)
$a068m290$	1	0.100100(58)	0.21206(24)	0.056824(29)	0.06601(26)
	2	0.100116(55)	0.21199(30)	0.056826(25)	0.06592(32)
$a068m230$	1	0.079683(59)	0.19396(26)	0.054070(39)	0.06305(27)
	2	0.079711(58)	0.19383(34)	0.054091(38)	0.06309(35)
$a068m175$	1	0.059384(73)	0.19243(14)	0.051712(44)	0.06196(13)
	2	0.059410(70)	0.19244(15)	0.051740(37)	0.06195(15)
$a067m135$	1	0.045672(70)	0.18526(12)	0.050186(43)	0.06082(11)
	2	0.045700(67)	0.18522(12)	0.050203(40)	0.06076(11)
$a053m295$	1	0.079603(46)	0.14969(21)	0.043945(25)	0.04970(22)
	2	0.079592(44)	0.14962(30)	0.043938(24)	0.04966(29)
$a053m230$	1	0.060892(52)	0.14809(9)	0.041897(28)	0.04917(9)
	2	0.060850(52)	0.14803(10)	0.041877(27)	0.04916(10)

TABLE V. Data for the pion and kaon masses and decay constants in lattice units obtained using simultaneous fits to the pseudoscalar-pseudoscalar (Smeared-Smeared) and the pseudoscalar-axial (Smeared-Point) correlators. See plots in Figs. 12 and 13. The statistics for the pions and kaons are different as described in the text and given in Table III. The number $i = 1$ or 2 in column two specifies that the results are based on an i -state truncation of Eq. (3).

Ens. ID	aM_ρ	aM_{K^*}	aM_Φ	M_{K^*}/M_ρ	M_Φ/M_ρ
$a117m310$	0.4622(41)	0.5202(20)	0.5705(13)	1.125(11)	1.234(11)
$a087m290L$	0.3548(32)	0.4081(17)	0.45688(95)	1.153(18)	1.295(17)
$a087m230$	0.3512(63)	0.4176(34)	0.4827(10)	1.189(23)	1.374(25)
$a087m230X$	0.3330(25)	0.3936(16)	0.44893(56)	1.182(10)	1.348(10)
$a086m180L$	0.3132(62)	0.3901(15)	0.44545(95)	1.246(25)	1.422(28)
$a068m290$	0.2858(39)	0.3388(17)	0.3873(11)	1.185(17)	1.355(19)
$a068m230$	0.2592(46)	0.3193(40)	0.3660(10)	1.232(27)	1.412(25)
$a068m175$	0.2444(64)	0.3169(13)	0.36838(64)	1.297(34)	1.507(40)
$a067m135$	0.229(11)	0.31069(89)	0.36145(40)	1.357(65)	1.578(76)
$a053m295$	0.2252(39)	0.2578(14)	0.28624(94)	1.145(21)	1.271(22)
$a053m230$	0.2041(48)	0.25183(99)	0.28707(50)	1.234(29)	1.407(33)
Physical				1.15037(61)	1.31525(58)

TABLE VI. Data for vector meson masses using 2-state fits. The Φ meson assumed to be a pure $\bar{s}s$ state and the disconnected contributions are neglected. Note that (i) estimates of M_ρ are not robust as the effective mass plot, M_ρ^{eff} , does not exhibit a credible plateau, and (ii) the input value of the strange quark in the calculation of M_{K^*} and M_Φ is heavier than the physical.

Ens. ID	aM_N	aM_Σ	aM_Λ	aM_Ξ	M_N/M_π
$a117m310$	0.6175(9)(1)	0.7219(38)(10)	0.6852(50)(5)	0.7741(46)(15)	3.414(23)
$a087m290$	0.468(5)				
$a087m290L$	0.4671(6)(10)	0.5588(41)(10)	0.5350(35)(1)	0.6132(25)(1)	3.654(39)
$a087m230$	0.4484(7)(0)	0.5652(53)(12)	0.5364(54)(9)	0.6395(25)(4)	4.448(51)
$a087m230X$	0.4368(14)(2)	0.5411(33)(8)	0.5107(37)(1)	0.5986(18)(1)	4.410(37)
$a086m180$	0.416(2)				
$a086m180L$	0.4166(7)(2)	0.5291(60)(19)	0.4918(92)(8)	0.5895(31)(10)	5.423(88)
$a068m290$	0.3726(7)(1)	0.4593(50)(20)	0.4376(39)(14)	0.5144(25)(18)	3.764(43)
$a068m230$	0.3482(8)(1)	0.4306(73)(22)	0.4095(42)(28)	0.4856(25)(2)	4.360(61)
$a068m175$	0.3262(29)(40)	0.4268(42)(9)	0.3983(42)(3)	0.4854(16)(3)	5.59(12)
$a067m135$	0.3161(15)(5)	0.4227(30)(1)	0.3884(46)(15)	0.4730(23)(11)	6.88(15)
$a053m295$	0.2935(4)(1)	0.3494(27)(18)	0.3338(26)(8)	0.3820(18)(3)	3.744(38)
$a053m230$	0.2749(6)(1)	0.3424(14)(8)	0.3221(13)(5)	0.3800(9)(4)	4.504(61)
Physical					6.956

TABLE VII. Masses of octet baryons in lattice units from 3-state fits. The statistics of the nucleon data is the highest as discussed in the text. This allowed investigation of two-, three-, and four-state truncations of Eq. (3) with the three- and four-state fits compared in Figs. 20 and 21 in Appendix D.

Ens. ID	aM_Δ	aM_{Σ^*}	aM_{Ξ^*}	aM_Ω	M_Ω/M_π
$a117m310$	0.7859(24)(20)	0.8553(72)(25)	0.9009(63)(23)	0.9473(59)(16)	5.174(24)
$a087m290$					
$a087m290L$	0.6077(9)(3)	0.6528(125)(36)	0.6988(92)(24)	0.7454(66)(12)	5.842(61)
$a087m230$	0.5931(28)(38)	0.6499(135)(48)		0.7883(38)(13)	7.600(44)
$a087m230X$	0.5823(29)(18)	0.6325(91)(5)		0.7374(39)(7)	7.398(31)
$a086m180$					
$a086m180L$	0.5658(20)(57)	0.6165(113)(31)		0.7302(43)(47)	9.425(63)
$a068m290$	0.4841(19)(38)	0.5352(125)(12)		0.6319(60)(66)	6.292(56)
$a068m230$	0.4569(37)(62)	0.5124(90)(4)		0.6005(63)(3)	7.523(49)
$a068m175$	0.4501(23)(56)	0.5046(99)(133)		0.5992(35)(13)	10.106(95)
$a067m135$	0.4392(35)(20)	0.4975(86)(68)		0.5909(29)(22)	13.058(55)
$a053m295$	0.3810(15)(23)	0.4076(115)(94)		0.4689(44)(14)	5.887(79)
$a053m230$	0.3664(19)(14)	0.3917(51)(13)		0.4704(15)(16)	7.754(26)
Physical					12.39

TABLE VIII. Masses of decuplet baryons in lattice units. The signal in the effective mass plots for the Δ , Σ^* and Ξ^* degrades into noise before a plateau is manifest, so these estimates, based on a 2-state fit, are not robust. For most ensembles, no data for Ξ^* were collected due to an oversight.

by the various combinations of the c_i specified in Table X. Neglecting the two models, with non-zero $\{c_1, c_2\}$ and $\{c_1, c_2, c_6\}$, that have large χ^2/dof , we perform an average weighted by σ^2 of the remaining nine to get the final value $\chi_Q = (65(10) \text{ MeV})^4$. This is shown by the magenta horizontal band at the bottom of Fig. 3, and is consistent with the result $\chi_Q = (66(6) \text{ MeV})^4$ obtained in Ref. [46] using the same methodology but on ensembles with 2+1+1-flavors of HISQ fermions provided by the MILC collaboration [47].

Phenomenologically, knowing χ_Q and especially its temperature dependence, is interesting for cosmology and whether the axion is a candidate for dark matter because of the relation:

$$m_a^2 f_a^2 = \chi_Q, \quad (17)$$

where m_a and f_a are the mass and the decay constant of the standard model axion that characterizes the axion coupling. To improve the estimate of χ_Q , the main requirement is similarly precise data on many more ensembles to control the chiral-continuum extrapolation, and, hopefully, with increasingly more terms in Eq. (16).

Lastly, a goal of this paper is to characterize these 2+1-flavor clover ensembles and validate that they are a good representation of the QCD vacuum. One requirement is that topology is not frozen [48] during the lattice generation. This requirement is satisfied on all eleven ensembles as confirmed by the time histories of Q and W at large flow time shown in Figs. 14–17 (plots on the right) in Appendix B.

ID	Configs Analyzed	$t_0^2 \chi_Q \times 10^4$ ($t_{gf} \rightarrow \infty$)	χ^2/dof
$a117m310$	998	2.12(10)	0.56
$a087m290L$	1794	1.634(63)	0.79
$a087m230$	2233	1.365(50)	0.29
$a087m230X$	2006	1.364(53)	1.2
$a086m180L$	1007	1.183(62)	0.61
$a068m290$	2112	1.040(39)	1.7
$a067m230$	2092	0.846(33)	0.32
$a067m175$	1676	0.697(32)	1.5
$a067m135$	602	0.666(47)	2.6
$a053m295$	2441	0.856(79)	0.3
$a053m230$	1958	0.601(26)	0.9

TABLE IX. The number of configurations used in the measurement of the topological charge Q and the Weinberg operator. The fit to $t_0^2 \chi_Q$ versus t_{gf}/t_0 , using Eq. (15) to obtain the value in the limit $t_{gf} \rightarrow \infty$ for each ensemble, is shown in Fig. 3 and the results summarized here.

IV. ANALYSIS OF THE DECAY CONSTANTS f_π AND f_K

The strength of the leptonic decays of pions ($\pi^+ \rightarrow \mu^+ \nu_\mu$) and kaons ($K^+ \rightarrow \mu^+ \nu_\mu$) via weak interactions is given by the decay constants f_π and f_K . These are obtained from the nuclear matrix elements, for example $\langle 0 | A_\mu | \pi(p) \rangle = i f_\pi p_\mu$, where A_μ is the renormalized axial part of the weak current and $\pi(p)$ is the pion state. These are, in turn, extracted efficiently and accurately from simultaneous fits to the lattice two-point functions (correlators) $\langle P_S(0)P_S(\tau) \rangle$ and $\langle P_S(0)A_P(\tau) \rangle$ with the interpolating operators $P = \bar{\psi} \gamma_5 \psi$ and $A_4 = \bar{\psi} \gamma_4 \gamma_5 \psi$

c_1	c_2	c_3	c_4	c_5	c_6	$\chi_Q^{1/4 Phy}$ (MeV)	χ^2/dof
2.86 (12)	1.10 (13)					74.1(2.4)	2.4
3.13(14)	0.007(359)	3.06(94)				51(15)	1.2
3.17(14)	-0.39(39)		6.6(1.7)			40(31)	0.50
2.48(15)	0.67(17)			3.36(88)		65.3(4.3)	0.69
2.87(13)	0.93(66)				0.11(40)	73.0(4.6)	2.7
3.15(14)	-0.38(39)	-1.5(2.1)	9.0(3.8)			45(22)	0.51
3.14(14)	1.28(67)	4.7(1.2)			-1.15(51)	58(11)	0.62
2.35(18)	1.54(68)			3.86(96)	-0.58(44)	70.8(5.0)	0.51
2.58(31)	0.52(44)	0.5(1.6)		2.9(1.5)		62.7(9.3)	0.79
2.89(31)	-0.05(50)		4.3(2.8)	1.5(1.5)		51(17)	0.41
3.15(15)	-0.03(71)		6.9(1.7)		-0.25(41)	48(20)	0.53

TABLE X. Results for the parameters c_i , defined in Eq. (16), for the eleven models used to perform the chiral-continuum extrapolation of the data for χ_Q . The $\chi_Q^{1/4|Phy}$ (MeV) for each model is given in column seven and the χ^2/dof of the fit in column eight.

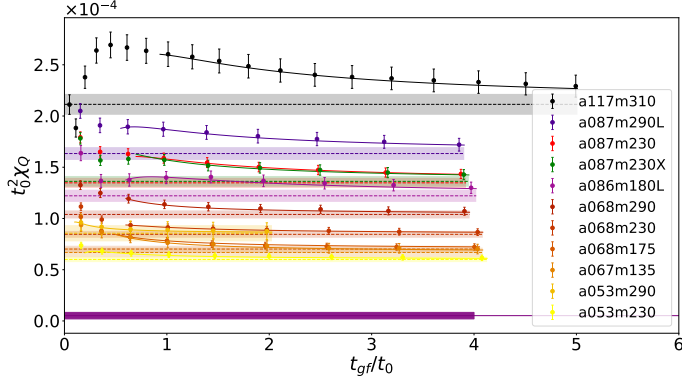


FIG. 3. The data for the dimensionless quantity $t_0^2 \chi_Q$ is plotted as a function of the flow time t_{gf}/t_0 for the eleven ensembles. To fit all the data on one plot, the x-axis for the $a117m310$ ensemble has been scaled and should be read as $(t_{gf}/t_0)/3$. To remove lattice artifacts, these data are fit versus $1/t_{gf}$ using Eq. (15). The $t_{gf}/t_0 \rightarrow \infty$ values are shown by the horizontal bands that are then extrapolated to the physical point using the chiral-continuum ansatz given in Eq. (16). This physical point result is shown by the magenta horizontal band at the bottom.

placed at time $t = 0$ (source) and τ (sink). The subscript S (P) denotes smeared (point) sources/sinks. Since the S2N in these correlators does not degrade with τ , we use the large τ limit of their spectral decomposition,

$$\langle P_S(0)A_P(\tau) \rangle = \sum_i \langle 0|P|\pi_i \rangle \langle \pi_i|A_4|0 \rangle e^{-E_i \tau}, \quad (18)$$

to isolate the ground state and obtain an accurate value of $\langle 0|A_\mu|\pi(p)\rangle$. Two kinds of fits are done to check consistency: (i) a 1-state fit starting at large τ_{\min} where a single state domination is manifest, i.e., the plateau in M^{eff} is well established, and (ii) a 2-state fit starting earlier at a τ_{\min} where some excited state effects are present as shown in Figs. 12 and 13. The results, summarized in Table V, show that the two fits give consistent, within

1σ , results for the masses, M_π and M_K , and the decay constants, f_π and f_K . For the final results, we take the estimates from the 1-state fits since the M_0 values from the individual fits to the two correlators are closer.

The statistical analysis of the data was done by generating two hundred bootstrap samples starting with the binned data on the eleven ensembles. Noting that the number of binned data points N_l/N_{bin} (or N_s/N_{bin} for strange states) in each ensemble are different, N_l/N_{bin} (or N_s/N_{bin}) values were drawn randomly from each. Estimates for M_π , f_π , M_K , and f_K on each of the 11 ensembles, were then calculated using Eq. (3). These bare lattice values of f_π and f_K were renormalized using the Z_A calculated for the local isovector axial vector current on these ensembles. (The results for all five renormalization factors, Z_Γ , for all 11 ensembles, calculated using the RI-sMOM intermediate scheme on the lattice, are summarized in Table XI and discussed in Sec. IV A.) Lastly, results at the physical point were obtained by doing a continuum-chiral fit. This process was repeated 200 times to get the 200 bootstrap samples used for estimating the errors.

The first application of these data is to extract the physical point value for the scales, t_0^{Phy} and w_0^{Phy} . As described in Sec. IV B, this is done using the chiral-continuum (CC) fit ansatz given in Eq. (20) for the combination $f_{\pi K}$ defined as

$$af_{\pi K} = Z_A \left(\frac{2}{3}af_K + \frac{1}{3}af_\pi \right). \quad (19)$$

The second, described in Sec. IV D, is to calculate the ratio $f_K/f_\pi|^{\text{Phy}}$ using two ansatz for the CC fit given in Eqs. (25) and (26) and the physical values given in Eq. (6).

Before presenting these analyses, we first discuss the calculation of the renormalization constants Z_Γ for all local quark bilinear operators, of which Z_A is used to renormalize A_μ needed in the calculation of f_π and f_K .

A. The Renormalization Constants Z_Γ

The renormalization constants, Z_Γ , for quark bilinear local operators are calculated using the regularization independent symmetric momentum subtraction (RI-sMOM) intermediate scheme on the lattice [29, 30]. We calculated the needed 2- and 3-point functions using external quark states on lattices fixed to the Landau gauge at a number of values of the four-momentum squared, p_{sym}^2 , that are symmetric (the same) in all three legs of the 3-point functions. These $Z^{\text{RI-sMOM}}$ for each p_{sym}^2 are converted to the $\overline{\text{MS}}$ scheme at scale μ using horizontal matching, i.e., with $\mu^2 = p_{\text{sym}}^2$, and then run to $\mu = 2$ GeV. The last two steps use results from QCD perturbation theory. The end results at $\mu = 2$ GeV should be independent of p_{sym}^2 for all the Z_Γ , however, in practice, they exhibit a small dependence on p_{sym}^2 that is a lattice artifact arising due to discretization effects, in particular

$$\sqrt{8t_0}f_{\pi K}(M_\pi, M_K, a) = \frac{A}{4\pi} \left[1 - \frac{7}{6}L\left(\frac{\phi_2}{A^2}\right) - \frac{4}{3}L\left(\frac{\phi_4 - \frac{1}{2}\phi_2}{A^2}\right) - \frac{1}{2}L\left(\frac{\frac{4}{3}\phi_4 - \phi_2}{A^2}\right) + B\phi_4 \right] \left(1 + Cf\left(\frac{a}{\sqrt{8t_0}}\right) \right), \quad (20)$$

with the first part on the right hand side modeling, motivated by χ PT [38, 39, 50], the chiral behavior and the second part the discretization corrections.

Here $L(x) = x \ln x$ and A, B, C are fit parameters that, in general, depend on ϕ_2, ϕ_4 and other low-energy constants of χ PT. The ideal situation for the adequacy of such a low-order ansatz would be if the ensembles had been generated along the green line in Fig. 2 implying a roughly constant m_s . Our ensembles, unfortunately, have a large variation with $m_s > m_s^{\text{Phy}}$. Future lattice generation should target the green line.

For parameterizing the discretization errors, we investigate three possibilities:

$$f(a) = \frac{a^2}{8t_0}, \quad \frac{\alpha_s a}{\sqrt{8t_0}}, \quad \frac{a}{\sqrt{8t_0}}, \quad (21)$$

with $\alpha_s a / \sqrt{8t_0}$ expected to be the closest for our almost $O(a)$ improved action.

As shown in Eq. (20), the analysis is done making all terms dimensionless using t_0/a^2 or w_0/a that are also calculated on the lattice. When using t_0/a^2 , $A = 4\pi\sqrt{8t_0}f_{\pi K}^{\text{chiral limit}}$. Doing the full analysis using w_0^2 instead of t_0/a^2 in Eq. (20) gives w_0^{Phy} , however, the results for t_0^{Phy} and w_0^{Phy} are highly correlated.

Our central analysis is done assuming $\{A, B, C\}$ are constants. The statistical analysis is done by generating 200 bootstrap samples. The values of $\{A, B, C\}$, using t_0 to make quantities dimensionless, are shown in Fig. 4.

With A, B, C determined, the relation in Eq. (20) is solved for t_0^{Phy} (or w_0^{Phy}) using physical point values

due to the Lorentz group being broken to 90° rotations. This artifact is removed by making a fit versus p_{sym}^2 over a range specified in physical units, i.e., in GeV. Such a fit introduces the need to know, even for Z_V and Z_A , a in GeV and $\alpha_s(1/a)$ for each ensemble. These are given in Table XIV and their extraction is discussed in Sec. IV C.

Further details of this procedure for calculating Z_Γ for the 2+1-flavor theory are given in the Appendix B in Ref. [49] and we direct readers to it. While we give results for Z_Γ calculated using both a^{naive} and $a^{\text{corr.}}$ in Table XI, all our final results are obtained using a^{naive} . Using these Z_A and a^{naive} , the estimates for the decay constants on the 11 ensembles are given in Table XIII.

B. Extracting the scales t_0^{Phy} and w_0^{Phy} using the data for $f_{\pi K}$

To extract t_0^{Phy} and w_0^{Phy} from the data for $f_{\pi K}$, a fit is made using the following ansatz:

for $f_{\pi K}$, ϕ_2 and ϕ_4 . The results for the three ansatz used for modeling discretization errors overlap as shown in Table XII, however, there is an insignificant increase in the value of t_0^{Phy} (and similarly of w_0^{Phy}) under $a^2 \rightarrow \alpha_s a \rightarrow a$. An example, one of the 200 bootstrap samples, of how well the ansatz in Eq. (20) fits the data is shown in Fig. 5.

Considering that the Dirac action used in this study is close to $O(a)$ improved, we choose the $f(a/\sqrt{8t_0}) = (\alpha_s a)/\sqrt{8t_0}$ ansatz for the central value and the larger of the three errors to get

$$\begin{aligned} \sqrt{t_0^{\text{Phy}}}|_{f_{\pi K}} &= 0.1424(26) \text{ fm}, \\ w_0^{\text{Phy}}|_{f_{\pi K}} &= 0.1718(25) \text{ fm}. \end{aligned} \quad (22)$$

These results agree, within 1σ , with the FLAG 2024 averages $\sqrt{t_0^{\text{Phy}}}|_{\text{FLAG}} = 0.14474(57)$ fm and $w_0^{\text{Phy}}|_{\text{FLAG}} = 0.17355(92)$ fm for the 2+1-flavor theory [43], however, the errors in our results are much larger.

With eleven data points, we have investigated a larger parameter space by allowing the A and B to depend on ϕ_4 . The ansatz $A(\phi_4) = A_0 + A_1\phi_4$ changed the results by $\sim 10\%$, however the error in t_0^{Phy} increased by a factor of about 5. The ansatz $B(\phi_4) = B_0 + B_1\phi_4$ led to unphysical results. We, therefore, conclude that these additional terms lead to overparameterization and our best estimates from the 11 ensembles are with keeping A and B constants.

Ens. ID		Z_A	Z_S	Z_P	Z_T	Z_V	Z_A/Z_V	Z_S/Z_V	Z_P/Z_V	Z_T/Z_V
$a117m310$	n	0.876(9)	0.820(11)	0.739(34)	0.881(12)	0.796(17)	1.097(13)	1.021(23)	0.925(49)	1.106(10)
	c	0.879(10)	0.841(11)	0.763(31)	0.871(16)	0.799(21)	1.096(15)	1.043(27)	0.951(49)	1.091(10)
$a087m290L$	n	0.884(11)	0.790(8)	0.717(16)	0.923(16)	0.823(16)	1.075(9)	0.957(22)	0.871(30)	1.122(8)
	c	0.885(12)	0.807(10)	0.736(13)	0.913(15)	0.824(17)	1.074(9)	0.977(23)	0.892(29)	1.109(8)
$a087m230$	n	0.883(7)	0.791(9)	0.720(21)	0.924(16)	0.825(15)	1.071(11)	0.958(26)	0.873(40)	1.122(8)
	c	0.884(8)	0.804(11)	0.733(20)	0.917(16)	0.826(16)	1.071(12)	0.973(27)	0.888(41)	1.112(8)
$a087m230X$	n	0.874(14)	0.776(7)	0.710(13)	0.919(19)	0.820(19)	1.065(8)	0.944(22)	0.865(30)	1.121(7)
	c	0.875(16)	0.786(7)	0.721(12)	0.913(20)	0.821(22)	1.065(9)	0.954(24)	0.877(30)	1.113(7)
$a086m180L$	n	0.872(11)	0.782(10)	0.712(15)	0.918(13)	0.823(15)	1.059(9)	0.946(19)	0.863(24)	1.116(8)
	c	0.873(11)	0.787(10)	0.717(14)	0.915(13)	0.823(16)	1.060(9)	0.952(19)	0.869(24)	1.113(8)
$a068m290$	n	0.896(7)	0.770(11)	0.721(10)	0.957(16)	0.853(12)	1.052(8)	0.902(26)	0.846(25)	1.123(6)
	c	0.897(7)	0.787(10)	0.738(9)	0.946(16)	0.853(13)	1.052(9)	0.923(26)	0.865(24)	1.110(6)
$a067m230$	n	0.891(5)	0.757(13)	0.701(11)	0.959(9)	0.852(9)	1.046(7)	0.886(22)	0.821(18)	1.126(7)
	c	0.892(5)	0.769(13)	0.712(10)	0.951(9)	0.852(8)	1.046(7)	0.900(22)	0.834(17)	1.117(7)
$a066m175$	n	0.895(6)	0.761(11)	0.713(12)	0.961(13)	0.852(12)	1.050(8)	0.891(24)	0.835(24)	1.129(6)
	c	0.895(6)	0.767(11)	0.719(12)	0.958(13)	0.852(12)	1.050(8)	0.898(23)	0.842(24)	1.124(6)
$a066m135$	n	0.894(14)	0.768(39)	0.714(29)	0.970(9)	0.853(16)	1.047(20)	0.891(44)	0.830(34)	1.138(20)
	c	0.897(12)	0.771(37)	0.715(30)	0.969(8)	0.857(13)	1.045(19)	0.892(47)	0.828(35)	1.132(17)
$a053m295$	n	0.900(6)	0.737(10)	0.692(11)	0.989(12)	0.865(9)	1.040(5)	0.850(19)	0.798(19)	1.143(6)
	c	0.900(7)	0.752(9)	0.706(9)	0.979(11)	0.866(10)	1.040(5)	0.866(19)	0.815(19)	1.132(6)
$a053m230$	n	0.902(5)	0.745(10)	0.705(10)	0.984(14)	0.870(9)	1.038(6)	0.856(19)	0.810(20)	1.132(6)
	c	0.903(5)	0.754(10)	0.715(10)	0.978(14)	0.870(9)	1.038(6)	0.866(19)	0.821(19)	1.125(6)

TABLE XI. The renormalization constants $Z_{\Gamma}^{\overline{\text{MS}}}(2\text{GeV})$ for the isovector quark bilinear operators. The steps in their calculation are (i) calculate $Z_{\Gamma}^{\text{RI-sMOM}}$ nonperturbatively on the lattice using the RI-sMOM scheme at various values of symmetric momentum p_{sym}^2 ; (ii) match to the continuum $\overline{\text{MS}}$ scheme at $\mu^2 = p_{\text{sym}}^2$; (iii) run these results to 2 GeV; and (iv) remove a lattice artifact, the dependence on p_{sym}^2 , by making fits as explained in the text. The labels "n" and "c" in the second column specify whether the results were obtained using a^{naive} or a^{corr} , respectively.

$O(a)$	A	B	C	$\sqrt{t_0^{\text{Phy}}}$	χ^2_{red}	A	B	C	w_0^{Phy}	χ^2_{red}
a^2	2.48(17)	-0.088(51)	-0.12(14)	0.1421(20)	0.96	3.17(21)	-0.100(29)	-0.72(18)	0.1702(23)	0.80
$\alpha_S a$	2.48(17)	-0.088(50)	-0.12(14)	0.1424(22)	0.96	3.20(22)	-0.100(29)	-0.64(16)	0.1718(25)	0.75
a	2.49(18)	-0.087(50)	-0.050(55)	0.1430(26)	0.95	3.25(22)	-0.097(28)	-0.243(59)	0.1744(29)	0.69

TABLE XII. Estimates for the fit parameters A , B , and C defined in Eq. (20), and the extracted values of $\sqrt{t_0^{\text{Phy}}}|_{f_{\pi K}}$ and $w_0^{\text{Phy}}|_{f_{\pi K}}$. Results are presented for the three ansatz used for modeling the discretization error.

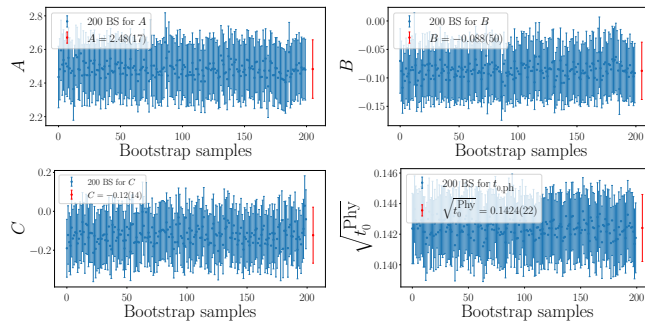


FIG. 4. Results for the fit parameters $\{A, B, C\}$ defined in Eq. (20) for the 200 bootstrap samples (BS) used for the statistical analysis. The red point on the right in each panel shows the bootstrap average. In these fits, t_0 was used to make quantities dimensionless.

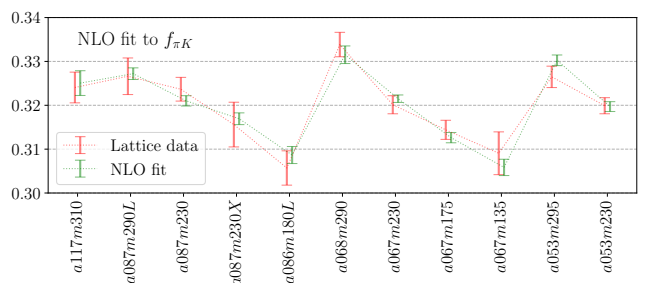


FIG. 5. This figure illustrates how well data for $\sqrt{8t_0}f_{\pi K}$ are fit by the ansatz in Eq. (20). The fit shown is for one bootstrap sample with t_0^{Phy} used to set the scale and the $\mathcal{O}(\alpha_s a)$ continuum correction factor. It has $\chi^2/\text{dof} = 1.20$.

Ens. ID	f_π^{bare} MeV	f_K^{bare} MeV	f_π^{ren} MeV	f_K^{ren} MeV
$a117m310$	170.3(3.1)	188.0(3.4)	149.2(3.1)	164.7(3.4)
$a087m290L$	161.2(3.0)	189.4(3.5)	142.5(3.2)	167.4(3.7)
$a087m230$	157.8(2.9)	183.0(3.4)	139.4(2.8)	161.6(3.2)
$a087m230X$	167.8(3.1)	190.2(3.6)	146.7(3.6)	166.2(4.1)
$a086m180L$	154.2(2.9)	181.3(3.4)	134.4(3.0)	158.1(3.6)
$a068m290$	164.4(2.9)	191.0(3.4)	147.3(2.8)	171.1(3.4)
$a068m230$	158.5(2.8)	184.9(3.4)	141.3(2.6)	164.7(3.2)
$a068m175$	152.3(2.7)	182.5(3.3)	136.3(2.6)	163.3(3.1)
$a067m135$	148.5(2.7)	179.9(3.3)	132.7(3.2)	160.9(3.8)
$a053m295$	162.5(3.0)	183.8(3.4)	146.3(2.8)	165.4(3.3)
$a053m230$	155.7(2.8)	182.7(3.4)	140.6(2.7)	165.0(3.2)

TABLE XIII. Bare and renormalized values for the pion and kaon decay constant using the renormalization constant Z_A specified in Table XI calculated using the lattice spacing a^{naive} given in Table XIV. For comparison, the values at the physical point given in FLAG 2024 [43] are $f_\pi = 130.2(0.8)$ MeV and $f_K = 155.7(0.7)$ MeV for the $N_f = 2 + 1$ theory.

C. Setting the lattice scale a using $\sqrt{t_0^{\text{Phy}}}$ and w_0^{Phy}

In the determination of the scales t_0^{Phy} and w_0^{Phy} using $f_{\pi K}$ (see Sec. IV B) or the octet or decuplet baryon masses, the value of the lattice spacing a in physical

units on each ensemble is not needed as the chiral part of the CC ansatz can be written in terms of dimensionless quantities and the calculation of Z_A does not depend on knowing $\alpha_s(1/a)$ and, thus, on a . A dependence on a is, however, introduced if the continuum part of the CC ansatz includes terms of $O(\alpha_s a)$. In this work we will neglect this (circular) effect as it is tiny as evident from the agreement of results obtained by considering the two values of α_s from two significantly different estimates of a given in Table XIV. Knowing the value of the scale a on each ensemble is, however, necessary in other analyses, for example in the calculation of the renormalization constants presented in Sec. IV A or if scales in physical units are used to regulate chiral logarithms as in Eq. (25).

In this section, we therefore determine the lattice spacing a on each ensemble in physical units based on the $f_{\pi K}$ fit. The first is the "naive" choice of a using the extracted value of t_0^{Phy} given in Eq. (22) and the measured t_0/a^2 :

$$a_{f_{\pi K}}^{\text{naive}} = (t_0/a^2)^{-1/2} \sqrt{t_0^{\text{Phy}}} \Big|_{f_{\pi K}}. \quad (23)$$

This definition implies that the value of a is adjusted so that $t_0 = t_0^{\text{Phy}}$ on each ensemble. The second, $a_{f_{\pi K}}^{\text{corr.}}$, includes the corrections factors given by the fit for $f_{\pi K}$:

$$\begin{aligned} a_{f_{\pi K}}^{\text{corr.}} &= a_{f_{\pi K}}^{\text{naive}} \times C_1 \times C_2 \\ C_1 &\equiv 1 + C \frac{\alpha_s a}{\sqrt{8t_0}}, \\ C_2 &\equiv \frac{1 - \frac{7}{6}L\left(\frac{\phi_2}{A^2}\right) - \frac{4}{3}L\left(\frac{\phi_4 - \frac{1}{2}\phi_2}{A^2}\right) - \frac{1}{2}L\left(\frac{\frac{4}{3}\phi_4 - \phi_2}{A^2}\right) + B\phi_4}{1 - \frac{7}{6}L\left(\frac{\phi_2^{\text{Phy}}}{A^2}\right) - \frac{4}{3}L\left(\frac{\phi_4^{\text{Phy}} - \frac{1}{2}\phi_2^{\text{Phy}}}{A^2}\right) - \frac{1}{2}L\left(\frac{\frac{4}{3}\phi_4^{\text{Phy}} - \phi_2^{\text{Phy}}}{A^2}\right) + B\phi_4^{\text{Phy}}}, \end{aligned} \quad (24)$$

where ϕ_2^{Phy} and ϕ_4^{Phy} are computed using the physical pion and kaon masses. These two estimates of the lattice spacing are summarized in Table XIV.

Two notable points regarding the second definition, $a^{\text{corr.}}$, given in Eq (24). First, most of the correction comes from the chiral behavior, i.e., from the term C_2 . Second, the net effect of including the correction factors C_i in extracting the lattice spacing $a^{\text{corr.}}$ is to set the quantity $f_{\pi K} = f_{\pi K}^{\text{Phy}}$ on each ensemble to within the accuracy of the fit ansatz. Thus, using $a^{\text{corr.}}$ to take the continuum limit for other quantities implies $f_{\pi K}$ is being kept constant in those fits.

In other words, these two definitions of the lattice scale specify which mass dimension quantity is held fixed in physical units and used to construct the dimensionless variables used in the CC fits to take the continuum limit, i.e., $a/\sqrt{8t_0}$ or $a f_{\pi K}$. To any given order of the CC ansatz both are valid. Differences reflect the fact that (i) truncated ansatz are used to make the CC fits and (ii) a

limited number of data points are available.

The last issue is—which value of a should be used in the calculation of $\alpha_s(1/a)$ that enters in modeling discretization errors if terms proportional to $\alpha_s a$ are used and in the scale dependent renormalization constants $Z_{S,T}$? For example, how to handle the difference in the results for the renormalized scalar charge of the nucleon, Z_{Sgs} , on each ensemble and in the final result g_S^{Phy} after the continuum-chiral extrapolation using a given ansatz? Again our contention is, at a given order, both are valid. One should, however, use $\alpha_s(1/a^{\text{naive}})$ [$\alpha_s(1/a^{\text{corr.}})$] with a^{naive} [$a^{\text{corr.}}$]. Note that in the two fits with the same CC ansatz and different a values, the fit parameters will absorb part of the differences. Only an exact fit ansatz applied to much more extensive data is expected to give the same g_S^{Phy} . Based on this understanding, in this work we use a^{naive} for the calculation of α_s , and the renormalization factors discussed in Sec. IV A. We neglect the differences in results from the full analysis with a^{naive} versus

Ens. ID	$a_{f_{\pi K}}^{\text{naive}}$ [fm]	$\alpha_s(1/a)$	C_1	C_2	$a_{f_{\pi K}}^{\text{corr.}}$ [fm]	$\alpha_s(1/a)$
$a117m310$	0.1165(21)	0.324(4)	0.998(13)	1.090(11)	0.1255(28)	0.338(6)
$a087m290L$	0.0874(16)	0.278(3)	0.9926(87)	1.090(12)	0.0946(18)	0.289(3)
$a087m230$	0.0873(16)	0.278(3)	0.9926(87)	1.069(12)	0.0927(18)	0.286(4)
$a087m230X$	0.0865(16)	0.277(3)	0.9927(86)	1.0566(87)	0.0908(16)	0.283(3)
$a086m180L$	0.0859(16)	0.276(3)	0.9928(85)	1.0301(62)	0.0879(15)	0.279(3)
$a068m290$	0.0682(12)	0.249(2)	0.9948(61)	1.099(16)	0.0745(15)	0.258(3)
$a068m230$	0.0673(12)	0.247(2)	0.9949(59)	1.067(11)	0.0714(13)	0.253(2)
$a068m175$	0.0670(12)	0.247(2)	0.9950(59)	1.0384(84)	0.0692(11)	0.250(2)
$a067m135$	0.0667(12)	0.246(2)	0.9950(59)	1.0167(61)	0.0674(10)	0.248(2)
$a053m295$	0.0534(10)	0.226(2)	0.9963(43)	1.093(13)	0.0581(11)	0.233(2)
$a053m230$	0.0531(10)	0.225(2)	0.9964(43)	1.0597(95)	0.05607(92)	0.230(2)

TABLE XIV. The lattice spacing $a_{f_{\pi K}}^{\text{naive}}$ is obtained using Eq. (23), which corresponds to requiring the value of t_0 on each ensemble to equal t_0^{Phy} obtained from the $f_{\pi K}$ fit. The second estimate, $a_{f_{\pi K}}^{\text{corr.}}$, is extracted from $a_{f_{\pi K}}^{\text{naive}}$ by including the continuum and chiral correction factors C_1 and C_2 as defined in Eq. (24). This scale corresponds to requiring $f_{\pi K}$ on each ensemble equals $f_{\pi K}^{\text{Phy}}$.

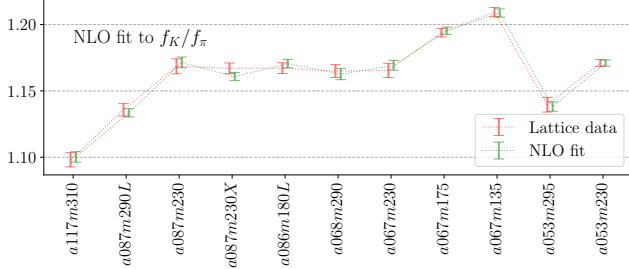


FIG. 6. Result of the fit to f_K/f_π using Eq. (25) with $\mathcal{O}(\alpha_s a)$ discretization ansatz and scale set by t_0^{phy} . A single bootstrap sample was used to make this plot. The fit has $\chi^2/\text{dof} = 1.09$. Plots using $\mathcal{O}(a)$ and $\mathcal{O}(a^2)$ are almost identical.

$a^{\text{corr.}}$ as they are much smaller than the other errors we quote.

D. Calculating the ratio f_K/f_π

Having used $f_{\pi K}$ to set the lattice scale, we can determine the second independent quantity f_K/f_π using the data for f_π and f_K . For this, we investigate two ansatz to carry out the chiral-continuum extrapolation. The first is the next-to-leading order chiral fit given in Ref. [40] that is based on the SU(3) χ PT in Ref. [38]:

$$\begin{aligned} \frac{f_K}{f_\pi} = 1 &+ \frac{c_0}{2} \left[\frac{5}{4} (8t_0 M_\pi^2) \log \frac{(aM_\pi)^2}{(a\mu)^2} \right. \\ &- \frac{1}{2} (8t_0 M_K^2) \log \frac{(aM_K)^2}{(a\mu)^2} \\ &- \frac{3}{4} (8t_0 M_\eta^2) \log \frac{(aM_\eta)^2}{(a\mu)^2} \\ &\left. + c_1 8t_0 (M_K^2 - M_\pi^2) \right], \quad (25) \end{aligned}$$

where $M_\eta^2 = (4M_K^2 - M_\pi^2)/3$ and μ is a fixed renormalization scale of the chiral effective theory in physical units, which we choose to be $\mu = 770$ MeV. Then, to keep all terms in Eq. (25) dimensionless requires knowing the lattice spacing a on each ensemble to converting μ to $a\mu$. We use a^{naive} determined in Sec. IV C.

We also consider the 4-parameter polynomial ansatz used in Ref. [40]:

$$\begin{aligned} \frac{f_K}{f_\pi} = 1 &+ 8t_0 (M_K^2 - M_\pi^2) \left[c_0 + c_1 8t_0 (M_K^2 - M_\pi^2) \right. \\ &\left. + c_2 8t_0 M_\pi^2 + c_3 8t_0 M_\pi^4 \right]. \quad (26) \end{aligned}$$

Table XV gives the results for $f_K/f_\pi|^{\text{phy}}$ obtained using different CC fit models: the three ansatz for discretization errors, the two ansatz for the chiral correction, and the two values of the lattice spacing, $a_{f_{\pi K}}^{\text{naive}}$ and $a_{f_{\pi K}}^{\text{corr.}}$. We choose $f_K/f_\pi = 1.193(33)$ given in Table XV

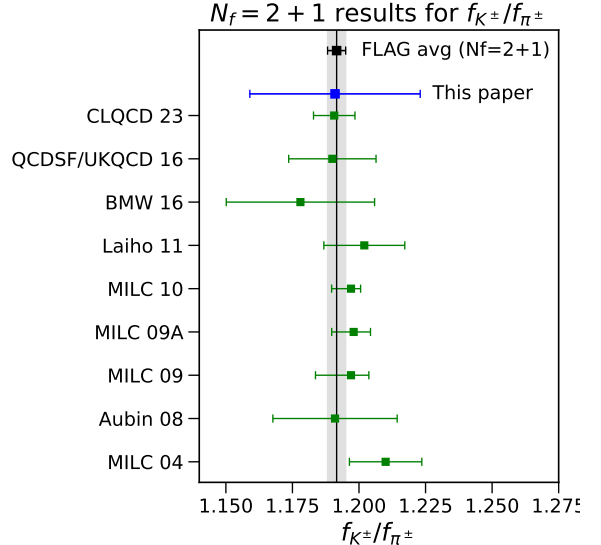


FIG. 7. Comparison of $\frac{f_{K^\pm}}{f_{\pi^\pm}}$ (blue square) obtained in this work with results from previous lattice studies with 2+1-flavor QCD: CLQCD 23 [52], QCDSF/UKQCD 16 [53], BMW 16 [40], Laiho 11 [54], MILC 10 [55], MILC 09A [56], MILC 09 [57], Aubin 08 [58], and MILC 04 [59]. The grey band shows the FLAG 2024 average given in Ref. [43].

for the $\mathcal{O}(\alpha_s a)$ continuum correction and a^{naive} . To compare this isosymmetric 2+1-flavor theory result with the phenomenological extraction, f_K^\pm/f_π^\pm , requires applying the isospin breaking correction $\delta_{\text{SU}(2)}$ [43, 51] using the relation:

$$\frac{f_{K^\pm}}{f_{\pi^\pm}} = \frac{f_K}{f_\pi} \sqrt{1 + \delta_{\text{SU}(2)}}. \quad (27)$$

We find $\delta_{\text{SU}(2)} = -0.0039(11) \implies \frac{f_{K^\pm}}{f_{\pi^\pm}} = 1.191(32)$. As shown in Fig. 7, while our central value is consistent, the error is large compared with other lattice determinations that enter the FLAG average and the FLAG 2024 average $\frac{f_{K^\pm}}{f_{\pi^\pm}} = 1.1917(37)$.

V. ANALYSIS OF THE OCTET AND DECUPLET BARYON SPECTRUM

Our analysis covers the 4 octet baryon states, $O \in \{N, \Sigma, \Lambda, \Xi\}$, and only one decuplet state, $D = \{\Omega\}$ that have a good S2N ratio as discussed in Sec. I D. The physical point values are obtained using a simultaneous CC fit as discussed in sections I C and I E with the full analysis done using t_0 and w_0^2 independently to make quantities dimensionless. The chiral parts of the fits, i.e., behavior versus pion and kaon masses, use predictions from heavy baryon chiral perturbation theory (HB χ PT) at NLO (accurate to $\mathcal{O}(m_q)$) and at NNLO (accurate to $\mathcal{O}(m_q^{3/2})$) order [41, 42] as discussed in Sec. I E. For discretization

$f(a/\sqrt{8t_0})$	Fit formula	$f_K/f_\pi _{\text{using } \sqrt{t_0^{\text{Phy}}} _{f_{\pi K}}}$	$f_K/f_\pi _{\text{using } w_0^{\text{Phy}} _{f_{\pi K}}}$
a^2	Eq. (25) with $a = a_{f_{\pi K}}^{\text{naive}}$	1.192(33)	1.195(35)
a^2	Eq. (25) with $a = a_{f_{\pi K}}^{\text{corr.}}$	1.200(44)	1.202(46)
a^2	Eq. (26)	1.186(22)	1.190(27)
α_{SA}	Eq. (25) with $a = a_{f_{\pi K}}^{\text{naive}}$	1.193(33)	1.193(35)
α_{SA}	Eq. (25) with $a = a_{f_{\pi K}}^{\text{corr.}}$	1.202(45)	1.201(47)
α_{SA}	Eq. (26)	1.188(23)	1.191(29)
a	Eq. (25) with $a = a_{f_{\pi K}}^{\text{naive}}$	1.196(35)	1.189(35)
a	Eq. (25) with $a = a_{f_{\pi K}}^{\text{corr.}}$	1.206(48)	1.199(47)
a	Eq. (26)	1.190(25)	1.191(30)

TABLE XV. Results for the ratio $f_K/f_\pi|_{\text{Phy}}$ for the three ansatz used for removing discretization errors, the two ansatz for the chiral correction, and two values of the lattice spacing, $a_{f_{\pi K}}^{\text{naive}}$ and $a_{f_{\pi K}}^{\text{corr.}}$. The statistical errors shown within the parentheses were calculated using the 200 bootstrap samples described in Sec. IV. Results are shown for the two cases: scale set by t_0^{Phy} (the $\chi^2/\text{dof} \approx 0.63(31)$ for all the fits) and w_0^{Phy} (the $\chi^2/\text{dof} \approx 0.70(34)$ for all the fits).

effects, three possible ansatz for the leading order correction term are explored. The inputs for this CC analysis are

- Lattice measurements of meson and baryon masses, $\{aM_\pi, aM_K, aM_O, aM_D\}$, the decay constants f_π and f_K , and the Wilson flow scales $\{t_0/a^2, w_0/a\}$ for each ensemble.
- HB χ PT formulae, made dimensionless using t_0/a^2 (or w_0/a) [39], describing the mass dependence of the octet (O) and the decuplet (D) baryons [41, 42], in terms of M_π and M_K .
- The physical values, M_π^{Phy} , M_K^{Phy} , and one other quantity given in Eq. (6) to set the quark masses and the lattice scale. One can choose it to be a baryon mass, or t_0^{Phy} or w_0^{Phy} .

Predictions for the octet and decuplet baryon spectrum are then extracted from these CC fits in the following two ways:

- Set the scale using t_0^{Phy} (or w_0^{Phy}) extracted in Sec. IV B.
- Use one baryon mass to set the scale and then predict t_0^{Phy} (or w_0^{Phy}), $f_{\pi K}$ and f_K/f_π and all but that one baryon mass.

A. Analysis of the octet baryon masses

The CC extrapolation formula for the octet baryon masses, with all variables made dimensionless using t_0/a^2 , is:

$$\begin{aligned} & \sqrt{8t_0}M_O(M_\pi, M_K, a) \\ &= \sqrt{8t_0}M_O(M_\pi, M_K, a=0) \\ & \quad \times \left\{ 1 + f(a) \left[c_o + \bar{c}_o(8t_0\bar{M}^2) + \delta c_O(8t_0\delta M^2) \right] \right\}, \end{aligned} \quad (28)$$

where $O \in \{N, \Lambda, \Sigma, \Xi\}$. For the factor $f(a)$ modeling discretization corrections, we investigate the same three cases given in Eq. (21). The continuum part of the ansatz has six parameters: the c_o and \bar{c}_o are common while δc_O are different for each octet baryon. The two mass parameters \bar{M}^2 and δM^2 are

$$\bar{M}^2 \equiv \frac{1}{3}(2M_K^2 + M_\pi^2), \quad \delta M^2 \equiv 2(M_K^2 - M_\pi^2). \quad (29)$$

The chiral part of the ansatz, at NNLO [$\mathcal{O}(m_q^{3/2})$] and

again in units of t_0 , is

$$\begin{aligned} \sqrt{8t_0}M_O(M_\pi, M_K) &= \mathbf{M}_0 + \bar{\mathbf{b}} \left(8t_0 \bar{M}^2 \right) + \boldsymbol{\delta b}_O \left(8t_0 \delta M^2 \right) \\ &+ \sum_{P=\pi, K, \eta_8} \mathbf{g}_{O,P} f_O \left(\frac{\sqrt{8t_0}M_P}{\mathbf{M}_0} \right), \end{aligned} \quad (30)$$

where the first three terms on the right define the NLO [$\mathcal{O}(m_q)$] ansatz. The various dimensionless parameters (bold letters), and their relation to commonly used parameters, are

$$\begin{aligned} \mathbf{M}_0 &\equiv \sqrt{8t_0}M_0, \\ \bar{\mathbf{b}} &\equiv \frac{\bar{b}}{\sqrt{8t_0}}, \quad \boldsymbol{\delta b}_O \equiv \frac{\delta b_O}{\sqrt{8t_0}}, \\ \mathbf{g}_{O,P} &\equiv \sqrt{8t_0} \frac{M_0^3}{(4\pi F_0)^2} g_{O,P}, \end{aligned} \quad (31)$$

with F_0 the pion decay constant in the limit of $N_f = 3$ massless quarks and $P \in \{\pi, K, \eta_8\}$. Note that in Ref. [32], the same factor $a/\sqrt{8t_0^*}$ was used for all ensembles with the same inverse coupling β . We use the $a/\sqrt{8t_0}$ calculated on each ensemble. The parameter \mathbf{M}_0 is the common octet baryon mass in the chiral-continuum limit, $\bar{\mathbf{b}}$ is the common fit parameter which controls the \bar{M}^2 dependence, and $\boldsymbol{\delta b}_O$ defines the SU(3) breaking part that is different for each state. The EOMS loop-function $f_O(x)$ [60–62] is given by

$$f_O(x) = -2x^3 \left[\sqrt{1 - \frac{x^2}{4}} \arccos \left(\frac{x}{2} \right) + \frac{x}{2} \ln x \right]. \quad (32)$$

The η_8 mass can be written in terms of the pion and kaon masses as

$$M_{\eta_8}^2 \approx \frac{4M_K^2 - M_\pi^2}{3} = \bar{M}^2 + \frac{1}{3}\delta M^2, \quad (33)$$

where we used Eq. (29) to get the second relation.

The NLO ansatz is specified by the four parameters, M_0, b_0, b_D, b_F (or equally, $\mathbf{M}_0, \bar{\mathbf{b}}, b_D, b_F$) defined as

$$\begin{aligned} \bar{\mathbf{b}} &= -6b_0 - 4b_D, \quad \delta b_N = \frac{2}{3}(3b_F - b_D), \\ \delta b_\Lambda &= -\frac{4}{3}b_D, \quad \delta b_\Sigma = \frac{4}{3}b_D, \\ \delta b_\Xi &= -\frac{2}{3}(3b_F + b_D). \end{aligned} \quad (34)$$

The LECs at NNLO introduce only two additional parameters D and F , usually expressed as $D/(4\pi F_0)$ and $F/(4\pi F_0)$, in terms of which

$$\begin{aligned}
g_{N,\pi} &= \frac{3}{2}(D+F)^2, & g_{N,K} &= \frac{5}{3}D^2 - 2DF + 3F^2, & g_{N,\eta_8} &= \frac{1}{6}(D-3F)^2, \\
g_{\Lambda,\pi} &= 2D^2, & g_{\Lambda,K} &= \frac{2}{3}D^2 + 6F^2, & g_{\Lambda,\eta_8} &= \frac{2}{3}D^2, \\
g_{\Sigma,\pi} &= \frac{2}{3}D^2 + 4F^2, & g_{\Sigma,K} &= 2D^2 + 2F^2, & g_{\Sigma,\eta_8} &= \frac{2}{3}D^2, \\
g_{\Xi,\pi} &= \frac{3}{2}(D-F)^2, & g_{\Xi,K} &= \frac{5}{3}D^2 + 2DF + 3F^2, & g_{\Xi,\eta_8} &= \frac{1}{6}(D+3F)^2. \tag{35}
\end{aligned}$$

Their dimensionless versions, \mathbf{D} and \mathbf{F} , are

$$\begin{aligned}
\mathbf{D}^2 &= \sqrt{8t_0} \frac{M_0^3}{(4\pi F_0)^2} D^2, \\
\mathbf{F}^2 &= \sqrt{8t_0} \frac{M_0^3}{(4\pi F_0)^2} F^2. \tag{36}
\end{aligned}$$

Thus, the NLO (NNLO) ansatz has a total of 10 (12) free parameters. We obtain these by fitting the 44 octet masses measured on the eleven ensembles, and the results are given in Table XVI for both t_0 and w_0 to make quantities dimensionless. How well the fits agree with the data for the masses on the 11 ensembles is shown in Figs. 8 using t_0^{Phy} . From these plots, we infer that the NNLO fit is preferred. With these fit parameters in hand, we

- extract the scales t_0^{Phy} or w_0^{Phy} using any one baryon mass, say M_N , to set the lattice scale. Thereafter, the analysis is similar to that presented in Sec. IV B with $f_{\pi K}$ replaced by M_N . The resulting values of t_0^{Phy} and w_0^{Phy} are given in Table XVII and shown in Figs. 10.
- Use the scales t_0^{Phy} or w_0^{Phy} extracted in Sec. IV B to predict the octet spectrum. The results are given in Table XVIII and shown in Figs. 10.

B. Analysis of the decuplet baryon masses

The chiral-continuum fit ansatz used for the decuplet masses is

$$\begin{aligned}
&\sqrt{8t_0}M_D(M_\pi, M_K, a) \\
&= \sqrt{8t_0}M_D(M_\pi, M_K) \\
&\quad \times \left\{ 1 + f(a) \left[c_d + \bar{c}_d \left(8t_0 \bar{M}^2 \right) + \delta c_D (8t_0 \delta M^2) \right] \right\}. \tag{37}
\end{aligned}$$

The $[\mathcal{O}(m_q^{3/2})]$ NNLO ChPT formula for the decuplet $D = \{\Delta, \Sigma^*, \Xi^*, \Omega\}$ baryons, using bold letters for di-

mensionless quantities, is [41, 42].

$$\begin{aligned}
&\sqrt{8t_0}M_D(M_\pi, M_K) \\
&= \mathbf{M}_{D0} + \bar{t} \left(8t_0 \bar{M}^2 \right) + \boldsymbol{\delta t}_D (8t_0 \delta M^2) \\
&\quad + \sum_{P=\pi, K, \eta_8} \mathbf{g}_{D,P} f_D \left(\frac{\sqrt{8t_0}M_P}{\mathbf{M}_{D0}}, \frac{\sqrt{8t_0}M_P}{\mathbf{M}_0} \right). \tag{38}
\end{aligned}$$

Again, the first three terms define the $[\mathcal{O}(m_q)]$ NLO ansatz. The parameter \mathbf{M}_{D0} is the decuplet baryon mass in the chiral limit; \bar{t} is a common fit parameter that controls the \bar{M}^2 dependence; $\boldsymbol{\delta t}_D$ is the SU(3) breaking term that is different for each decuplet state; and the EOMS loop-function is [60–62]

$$\begin{aligned}
f_D(x, y) &= -2x^3 \left\{ \left(1 - \frac{x^2}{4} \right)^{5/2} \arccos \left(\frac{x}{2} \right) \right. \\
&\quad \left. + \frac{x}{64} [17 - 2x^2 + 2(30 - 10x^2 + x^4) \ln y] \right\}. \tag{39}
\end{aligned}$$

Note the M_0 dependence in the second arguments of the loop function. For fits using only the Ω mass, \mathbf{M}_0 in the functions f_D in Eq. (30) is not constrained. Therefore, we replace \mathbf{M}_0 by \mathbf{M}_{D0} . This replacement effects higher-order corrections, i.e., beyond the order we are working at (see the comment below Eq. (5.23) in Ref. [32]).

The relation between the dimensionless parameters and the commonly used parameters are

$$\begin{aligned}
\mathbf{M}_{D0} &\equiv \sqrt{8t_0}M_{D0}, \quad \bar{t} \equiv \frac{\bar{t}}{\sqrt{8t_0}}, \quad \boldsymbol{\delta t}_D \equiv \frac{\boldsymbol{\delta t}_D}{\sqrt{8t_0}}, \\
\mathbf{g}_{D,P} &\equiv \sqrt{8t_0} \frac{M_0^3}{(4\pi F_0)^2} g_{D,P}. \tag{40}
\end{aligned}$$

These NLO parameters can be written in terms of the decuplet LECs t_{D0} and t_D as

$$\begin{aligned}
\bar{t} &= 3t_{D0} + 3t_D, \quad \delta t_\Delta = -t_D, \quad \delta t_{\Sigma^*} = 0, \\
\delta t_{\Xi^*} &= t_D, \quad \delta t_\Omega = 2t_D, \tag{41}
\end{aligned}$$

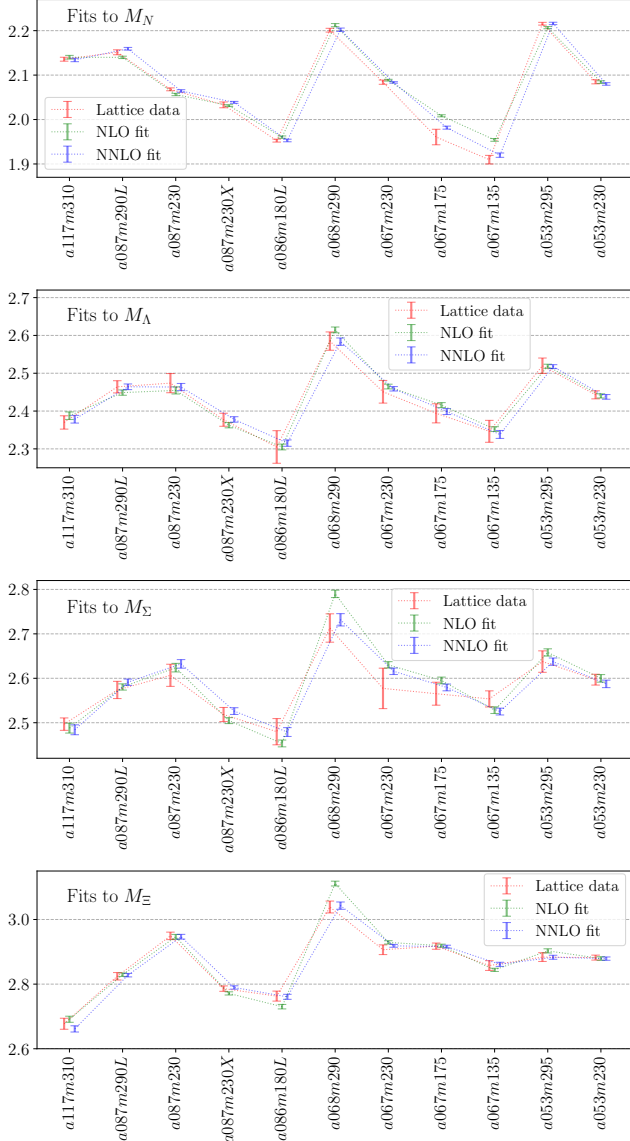


FIG. 8. Comparison of NLO versus NNLO chiral fits to the four octet baryon masses in units of t_0 , i.e., the y-axis labels are $\{\sqrt{8t_0}M_N, \sqrt{8t_0}M_\Lambda, \sqrt{8t_0}M_\Sigma, \sqrt{8t_0}M_\Xi\}$. The $\mathcal{O}(\alpha_s a)$ ansatz is used to remove discretization errors and t_0^{Phy} is used to set the scale.

and the NNLO parameters in terms of the LEC \mathcal{H}

$$\begin{aligned}
g_{\Delta,\pi} &= \frac{25}{54}\mathcal{H}^2, & g_{\Delta,K} &= \frac{5}{27}\mathcal{H}^2, & g_{\Delta,\eta_8} &= \frac{5}{54}\mathcal{H}^2, \\
g_{\Sigma^*,\pi} &= \frac{20}{81}\mathcal{H}^2, & g_{\Sigma^*,K} &= \frac{40}{81}\mathcal{H}^2, & g_{\Sigma^*,\eta_8} &= 0, \\
g_{\Xi^*,\pi} &= \frac{5}{54}\mathcal{H}^2, & g_{\Xi^*,K} &= \frac{5}{9}\mathcal{H}^2, & g_{\Xi^*,\eta_8} &= \frac{5}{54}\mathcal{H}^2, \\
g_{\Omega,\pi} &= 0, & g_{\Omega,K} &= \frac{10}{27}\mathcal{H}^2, & g_{\Omega,\eta_8} &= \frac{10}{54}\mathcal{H}^2. \quad (42)
\end{aligned}$$

Its dimensionless version \mathbf{H} is

$$\mathbf{H}^2 = \sqrt{8t_0} \frac{M_{D0}^3}{(4\pi F_0)^2} \mathcal{H}^2. \quad (43)$$

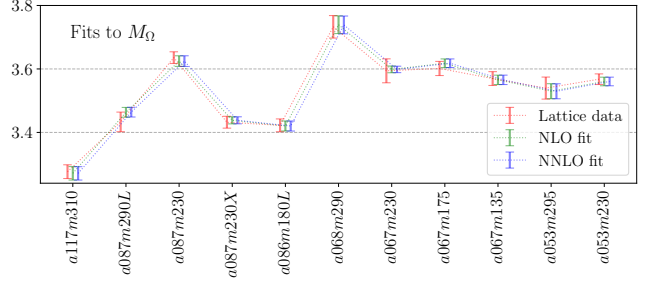


FIG. 9. Comparison of the NLO versus NNLO chiral fits to the Omega baryon mass in units of t_0 , i.e., $\sqrt{8t_0}M_\Omega$. The ansatz used to remove discretization errors is the $\mathcal{O}(\alpha_s a)$ and t_0^{Phy} is used to set the scale.

Thus, there are 6 (7) dimensionless fit parameters in Eq. (6) for the Ω NLO (NNLO) fits, respectively. These are given in Table XVI for both t_0 and w_0 to make quantities dimensionless. How well the NLO and NNLO fits agree with the M_Ω data on the 11 ensembles is shown in Fig. 9 using t_0^{Phy} . We find no significant difference and prefer the NLO ansatz since the χ^2/dof increases with the NNLO. With these dimensionless fit parameters in hand, we determine

- the flow scales t_0^{Phy} (or w_0^{Phy}) using, as input, M_Ω^{Phy} . Results are given in Table XVII and compared with other determinations in Fig. 10. The errors in our determinations are large with that from M_Ω being the largest. This is because while the fit for the octet uses 44 data points, only 11 M_Ω are available for the decuplet.
- M_Ω^{Phy} using t_0^{Phy} . The results are given in Table XVIII and shown in Fig. 11.

VI. COMPARISON WITH OTHER EFFORTS TO GENERATE AND CHARACTERIZE 2+1-FLAVOR LATTICE ENSEMBLES.

A short overview of various efforts worldwide to generate lattice ensembles is being provided at the annual international conferences on lattice QCD [63, 64]. A number of collaborations are generating and analyzing 2+1-flavor Wilson-clover lattices. Using our set of 11 NME ensembles (one with physical pion mass), we present a study similar to that by the RQCD collaboration in Ref. [32] based on 45 ensembles generated by the Coordinated Lattice Simulations (CLS) effort [10, 65, 66] and some additional ones by the RQCD collaboration. Others efforts are (i) the HALQCD collaboration [67] (one physical pion mass ensemble) (ii) the QCDSF collaboration [68] (21 ensembles with $M_\pi^{\text{lightest}} = 220$ MeV); (iii) the PACS collaboration [69] (three physical pion mass ensembles); and (iv) the CLQCD collaboration [52] (16 ensembles with three at physical pion mass). One of our goals is to reach

fit	χ^2/N_{DF}	c_o	\bar{c}_o	δc_N	δc_Λ	δc_Σ	δc_Ξ
octet NLO with t_0	3.75	1.75(66)	-1.84(78)	-0.413(55)	-0.370(66)	-0.399(64)	-0.332(56)
octet NNLO with t_0	0.57	-1.07(65)	0.13(78)	0.157(93)	0.22(11)	0.27(11)	0.236(86)
octet NLO with w_0	3.02	0.28(11)	-0.259(99)	-0.0498(78)	-0.0388(87)	-0.0396(82)	-0.0289(76)
octet NNLO with w_0	0.79	-0.03(11)	-0.10(10)	-0.0009(116)	0.009(13)	0.015(12)	0.015(11)
fit	χ^2/N_{DF}	M_0	\bar{b}	b_D	b_F	D	F
octet NLO with t_0	3.75	1.520(84)	1.160(89)	0.0301(40)	-0.0954(16)	-	-
octet NNLO with t_0	0.57	1.654(88)	2.14(19)	0.073(26)	-0.195(13)	0.752(63)	0.276(63)
octet NLO with w_0	3.02	1.77(12)	1.022(92)	0.0253(35)	-0.0802(14)	-	-
octet NNLO with w_0	0.79	1.90(12)	1.75(18)	0.053(26)	-0.157(12)	0.725(79)	0.284(81)
fit	χ^2/N_{DF}	c_d	\bar{c}_d	δc_Δ	δc_{Σ^*}	δc_{Ξ^*}	δc_Ω
Ω NLO with t_0	0.57	-1.3(2.1)	1.0(2.4)	-	-	-	-0.10(39)
Ω NNLO with t_0	0.63	-1.4(2.1)	1.1(2.4)	-	-	-	-0.10(39)
Ω NLO with w_0	0.88	-0.7(2.6)	0.2(2.5)	-	-	-	-0.30(38)
Ω NNLO with w_0	1.02	-0.7(2.6)	0.3(2.5)	-	-	-	-0.30(38)
fit	χ^2/N_{DF}	M_{D0}	\bar{t}	t_D		H	
Ω NLO with t_0	0.57	2.79(43)	0.37(45)	0.119(47)		-	
Ω NNLO with t_0	0.63	2.80(43)	0.36(45)	0.118(47)		Not constrained	
Ω NLO with w_0	0.88	3.07(38)	0.41(30)	0.115(30)		-	
Ω NNLO with w_0	1.02	3.08(38)	0.40(31)	0.115(30)		Not constrained	

TABLE XVI. Results for the dimensionless fit parameters, converted using $\sqrt{8t_0}$ (upper table) or using $\sqrt{8w_0}$ (lower table), in the CC extrapolation ansatz used for the octet and Ω baryon masses as defined in Eqs. (30), (37) and (38). Results are given for both the NLO and NNLO chiral ansatz, and organized into separate blocks for the continuum and the chiral parameters. Note that H is not constrained by the fit. The discretization errors were modeled using the $\mathcal{O}(\alpha_s a)$ ansatz.

Flow scales [fm]	N	Physical baryon mass used as input			
		Λ	Σ	Ξ	Ω
$\sqrt{t_0^{\text{Phy}}}$ (NLO)	0.1457(26)	0.1394(44)	0.1384(57)	-	0.1489(58)
$\sqrt{t_0^{\text{Phy}}}$ (NNLO)	0.1461(17)	0.1453(26)	0.1456(21)	0.1501(22)	0.1491(56)
w_0^{Phy} (NLO)	0.1756(31)	0.1681(58)	0.1672(77)	0.161(11)	0.1778(98)
w_0^{Phy} (NNLO)	0.1738(22)	0.1730(38)	0.1731(28)	0.1791(30)	0.1783(92)

TABLE XVII. Results for the flow scales $\sqrt{t_0^{\text{Phy}}}$ and w_0^{Phy} determined using fits with the NLO and NNLO ansatz from HB χ PT and the physical mass of one of the octet or the Ω baryon given in Eq. (6). The analysis of the decuplet spectrum is done only for the M_Ω data as explained in the text. The ansatz $\mathcal{O}(\alpha_s a)$ is used to model the discretization correction. We did not find a solution for t_0^{Phy} using the NLO ansatz with M_Ξ as input.

high statistics to determine whether one can demonstrate a data driven method for removing excited-state contributions in 3-point functions using multi-state fits [49]. Towards that goal, the analysis of 3-point functions for extracting nucleon charges and form factors from these ensembles is under progress and results will be reported separately. The analyses here highlight the need for also having a much larger set of ensembles to control the

chiral-continuum fits, especially with higher order ansatz in each. Lastly, we plan to add companion ensembles to the existing eleven with the strange quark mass tuned to its physical value.

	m_N	m_Λ	m_Σ	m_Ξ	m_Ω	$f_{\pi K}$
Pheno: Eq. (6)	937.54(6)	1115.68(1)	1190.66(12)	1316.9(3)	1669.5(3.0)	148.32(34)
Fit with a^2	939.3(7.7)	1114(11)	1188.7(8.3)	1333.7(8.8)	1682(34)	146.3(1.5)
Fit with $\alpha_s a$	945(10)	1118(14)	1195(11)	1340(12)	1698(46)	146.5(1.6)
Fit with a	955(14)	1126(19)	1206(16)	1350(17)	1737(72)	147.0(1.9)

TABLE XVIII. Comparing our results for the mass spectrum and the decay constant $f_{\pi K}$ in units of MeV obtained using the NNLO chiral ansatz and for the three possible ansatz for discretization corrections given in Eq. 21. The phenomenological values in row one for the 2+1-flavor theory used for comparison are reproduced from Eq. (6). The scale is set using $\sqrt{t_0^{\text{Phy}}}|_{\text{FLAG}} = 0.14474(57)$ fm taken from the FLAG 2024 report [43].

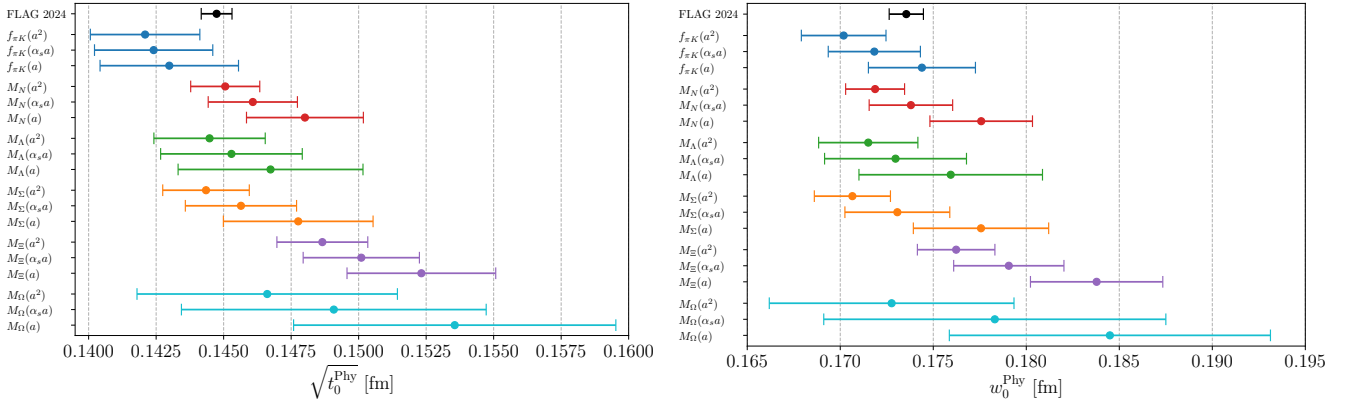


FIG. 10. Our results for t_0^{Phy} (left) and w_0^{Phy} (right) using various measured quantities specified in the y-axis labels and for the three ansatz used to remove discretization errors. For comparison, the FLAG 2024 average value [43] is shown at the top.

VII. CONCLUSIONS

This work describes the eleven NME ensembles with 2+1-flavors of Wilson-clover fermions generated mostly by us as part of a larger effort by the JLab/W&M/LANL/MIT/Marseille collaborations in Sec. I, and presents data on the flow scales t_0 and w_0 (Secs. II and IV B, and Appendix B), scale setting on the lattices (Sec. IV C), the decay constants f_π and f_K (Sec. IV), the behavior of the topological charge and the Weinberg three-gluon operator under Wilson flow (Sec. III, and Appendix B), the meson and baryon spectrum (Secs. V A and V B), a study of autocorrelations in the data, which is needed for the statistical analysis of the various quantities (Appendix C), and results for the renormalization constants for all five quark bilinear local operators (Sec. IV A).

In Sec. IV, we use the data for $f_{\pi K} \equiv (2f_K + f_\pi)/3$ to calculate the physical point values, t_0^{Phy} and w_0^{Phy} . In Sec. IV D, we calculate f_K/f_π^{Phy} , the second independent quantity using the data for f_π and f_K . The result $\frac{f_K \pm}{f_\pi \pm} = 1.191(32)$ agrees with the FLAG 2024 average, however, the errors in our estimate are larger as shown in Fig. 7.

The scales t_0^{Phy} and w_0^{Phy} are also extracted using the data for each of the masses of the four octet states, $\{N, \Lambda, \Sigma, \Xi\}$, and the decuplet state Ω . The resulting estimates are summarized in Fig. 10. The errors in our estimates are significantly larger than those in the FLAG 2024 averages, mostly because the chiral-continuum extrapolation based on 11 ensembles does not provide enough constraints on the parameters. Our best estimates of t_0^{Phy} and w_0^{Phy} are from the analysis of $f_{\pi K}$.

The lattice scale a on each ensemble is determined using the values of t_0^{Phy} and w_0^{Phy} and the fit to $f_{\pi K}$. We give two values, a^{naive} and $a^{\text{corr.}}$ that correspond to taking the continuum limit holding $t_0 = t_0^{\text{Phy}}$ and $f_{\pi K} = f_{\pi K}^{\text{Phy}}$, respectively, on each ensemble. Both are equally well motivated and the differences reflect residual discretization errors and having most ensembles at non-physical values of the light and strange quark masses. The impact of the differences in the two sets of lattice scale a in the CC fits used to obtain physical point values for the other observables is small—the parameters of the CC fits adjust to absorb most of the differences.

We choose to present all final results using a^{naive} but do give results for both so that the reader can assess the effect. An overview of the status and issues with various

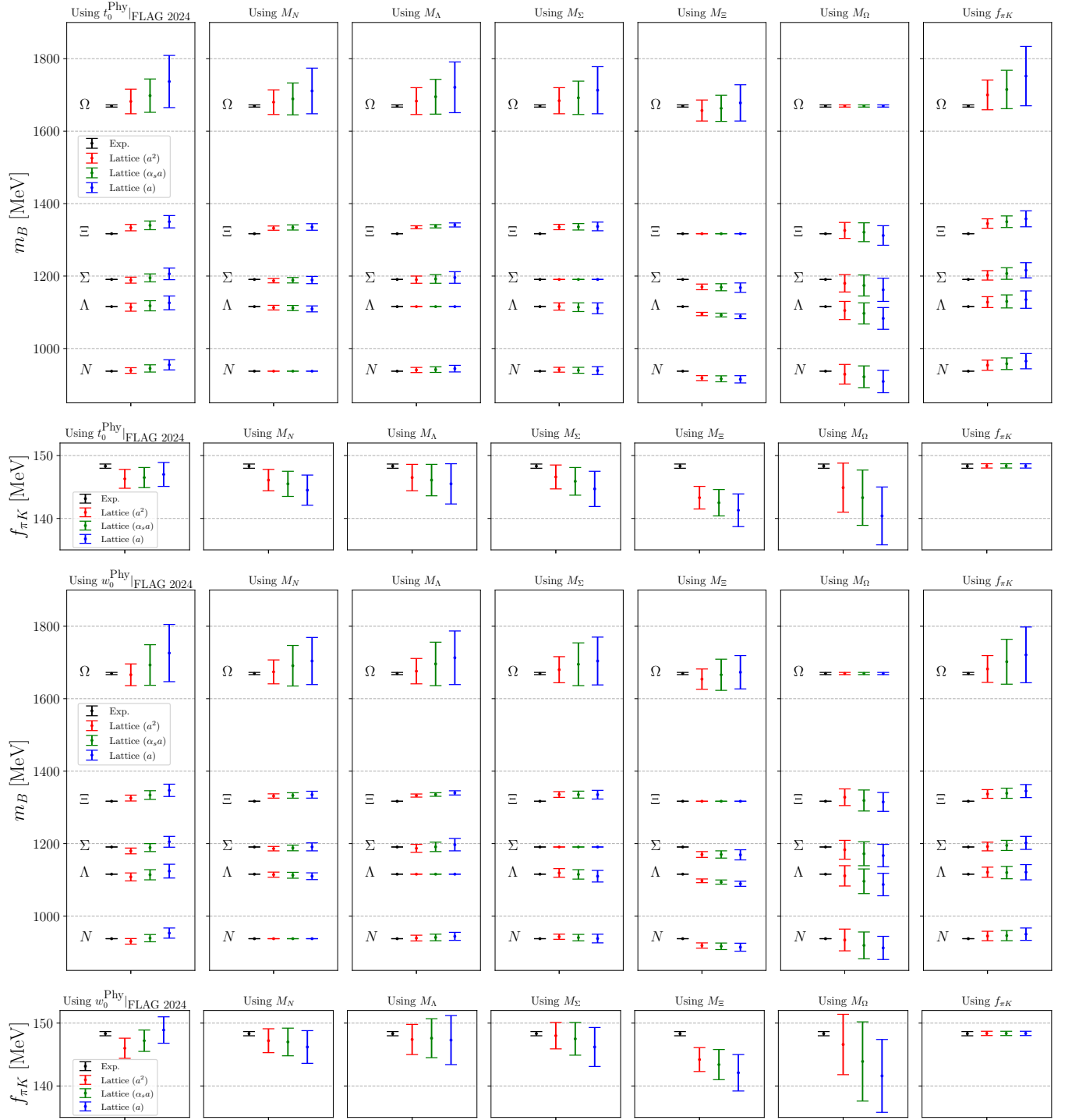


FIG. 11. Predictions of the baryon spectrum and $f_{\pi K}$. The scale is set using t_0^{Phy} (top 2 rows) and w_0^{Phy} (bottom 2 rows) taken from the FLAG 2024 report [43] or our calculation of the quantity specified on top of the figures. Also all quantities are made dimensionless using t_0 (top) w_0 (bottom). Results are given for the three ansatz used to model discretization errors. While the diagonal panels, e.g., predicting M_N using M_N , are shown, the data are trivial. The experimental and FLAG values are taken from Eqs. (6) and (7).

methods used to set the lattice scale a and determine t_0^{Phy} and w_0^{Phy} have been reviewed in the FLAG 2024 report [43].

Fits to get the values of the octet spectrum, $\{M_N, M_\Lambda, M_\Sigma, M_\Xi\}$, at the physical point were carried out using both NLO and NNLO expressions from HB χ PT. As shown in Fig. 8, the NNLO ansatz fit does a better job. For discretization errors, we explored three ansatz $\{\mathcal{O}(a), \mathcal{O}(\alpha_s a), \mathcal{O}(a^2)\}$. They give overlapping results, and the final result is presented with the $\mathcal{O}(\alpha_s a)$ ansatz as our action is almost $\mathcal{O}(a)$ improved.

Fits to decuplet data are less robust as we can only use M_Ω . The NLO and NNLO fits are equally good and the output values consistent as shown in Fig. 9, however, since no reduction in χ^2/dof is observed due to the extra parameter in the NNLO ansatz, we pick the NLO result.

The time history of the Θ and Weinberg operator at large flow time is shown in Appendix B and the data show no evidence for frozen topology in the generation of any of the 11 ensembles.

In Appendix C, we present a study of autocorrelations in the long-distance variables t_0 and w_0 , and find them to be large. To offset these, all analyses of spectral quantities and decay constants, is done using data binned over a sufficiently large number of measurements such that the binned data do not show significant autocorrelations.

Overall, the results from these eleven ensembles are consistent with previous lattice calculations by other collaborations and experimental values. The main limitation in obtaining high precision results are the chiral-continuum fits, i.e., the need for a larger set of ensembles. This work validates the efficacy of using these ensembles for further studies of other observables and our goal of improving precision by generating and analyzing more ensembles, especially ones with $M_K = M_K^{\text{Phy}}$.

ACKNOWLEDGMENTS

We thank Will Detmold and Stefan Meinel for discussions over the years on lattice generation and with Stefan Schaefer on scale setting. The calculations used the Chroma software suite [7]. This research used resources at (i) the National Energy Research Scientific Computing Center, a DOE Office of Science User Facility supported by the Office of Science of the U.S. Department of Energy under Contract No. DE-AC02-05CH11231; (ii) the Oak Ridge Leadership Computing Facility, which is a DOE Office of Science User Facility supported under Contract DE-AC05-00OR22725, through the ALCC program project LGT107 and HEP145, and the INCITE program project HEP133; (iii) the USQCD collaboration, which is funded by the Office of Science of the U.S. Department of Energy; and (iv) Institutional Computing at Los Alamos National Laboratory. This work was prepared in part by LLNL under Contract DE-AC52-07NA27344. S. Park acknowledges the support from the ASC COSMON project. T. Bhattacharya and R. Gupta

were partly supported by the U.S. Department of Energy, Office of Science, Office of High Energy Physics under Contract No. DE-AC52-06NA25396. T. Bhattacharya, R. Gupta, S. Mondal, S. Park, and J. Yoo were partly supported by the LANL LDRD program, and S. Park by the Center for Nonlinear Studies. J. Yoo was partly supported by Brain Pool program funded by the Ministry of Science and ICT through the National Research Foundation of Korea (R2528521).

Appendix A: Effective mass plots for the pion and 2-state fits

Figures 12–13 show the M_{eff} for the pion and the results of 2-state fits to the $\langle P_S(0)P_S(\tau) \rangle$, $\langle P_S(0)P_P(\tau) \rangle$, and $\langle P_S(0)A_P(\tau) \rangle$ two-point correlators on the eleven ensembles. The final results for $M_\pi^{(2)}$ and $f_\pi^{(2)}$, presented in Table V, are obtained from simultaneous fits to $\langle P_S(0)P_S(\tau) \rangle$ and $\langle P_S(0)A_P(\tau) \rangle$.

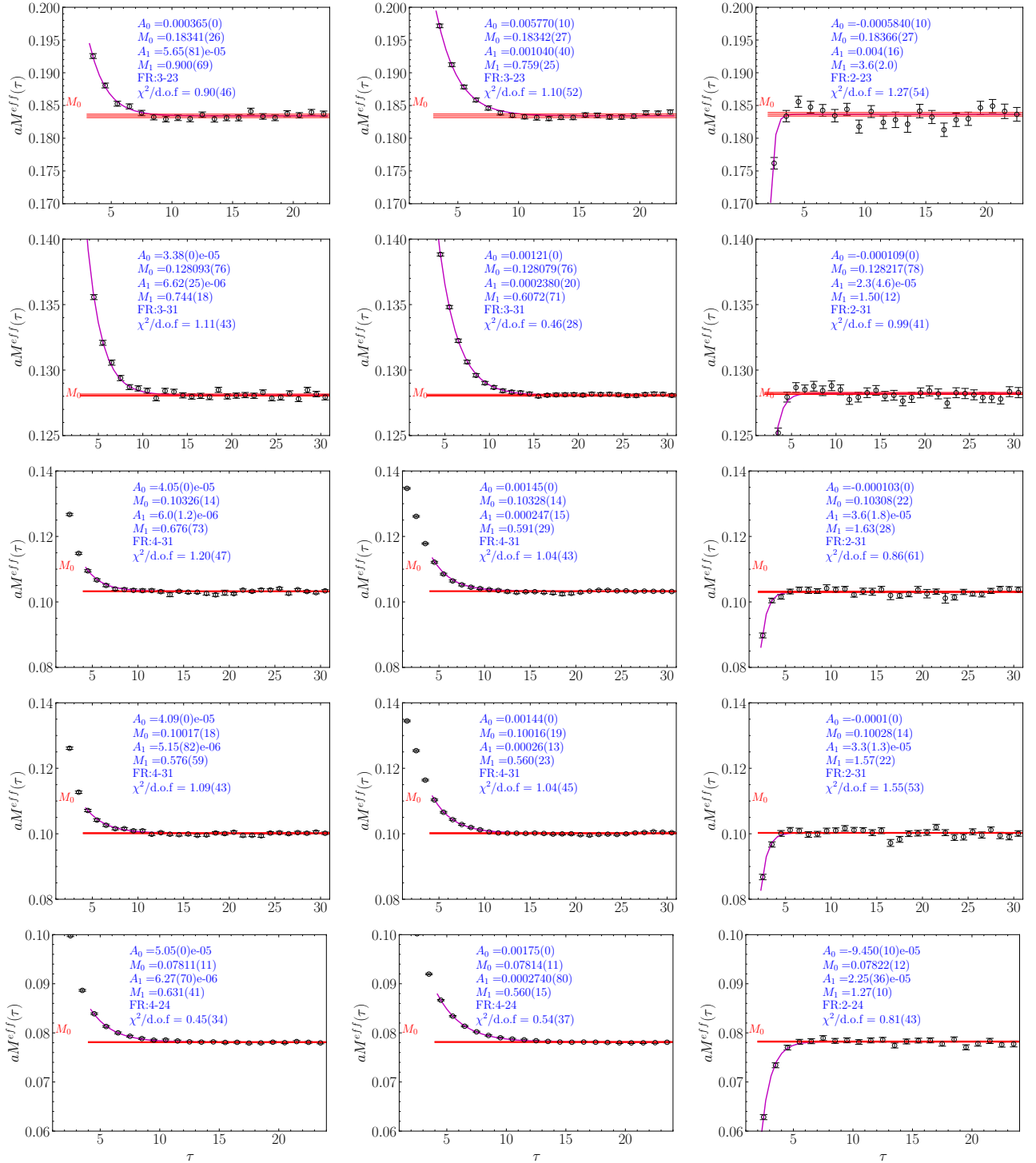


FIG. 12. The pion effective mass in lattice units, aM^{eff} , and two-state fits to the $\langle P_S(0)P_S(\tau) \rangle$ (left), $\langle P_S(0)P_P(\tau) \rangle$ (middle), and $\langle P_S(0)A_P(\tau) \rangle$ (right) correlators on the $a117m310$ (top), $a087m290L$ (second), $a087m230$ (third) and $a087m230X$ (fourth), and $a086m180L$ (bottom) ensembles. The legend gives the two-state fit parameters, the fit range (FR), and the $\chi^2/\text{d.o.f.}$ of the fit. The horizontal red lines give M_0 , also in lattice units.

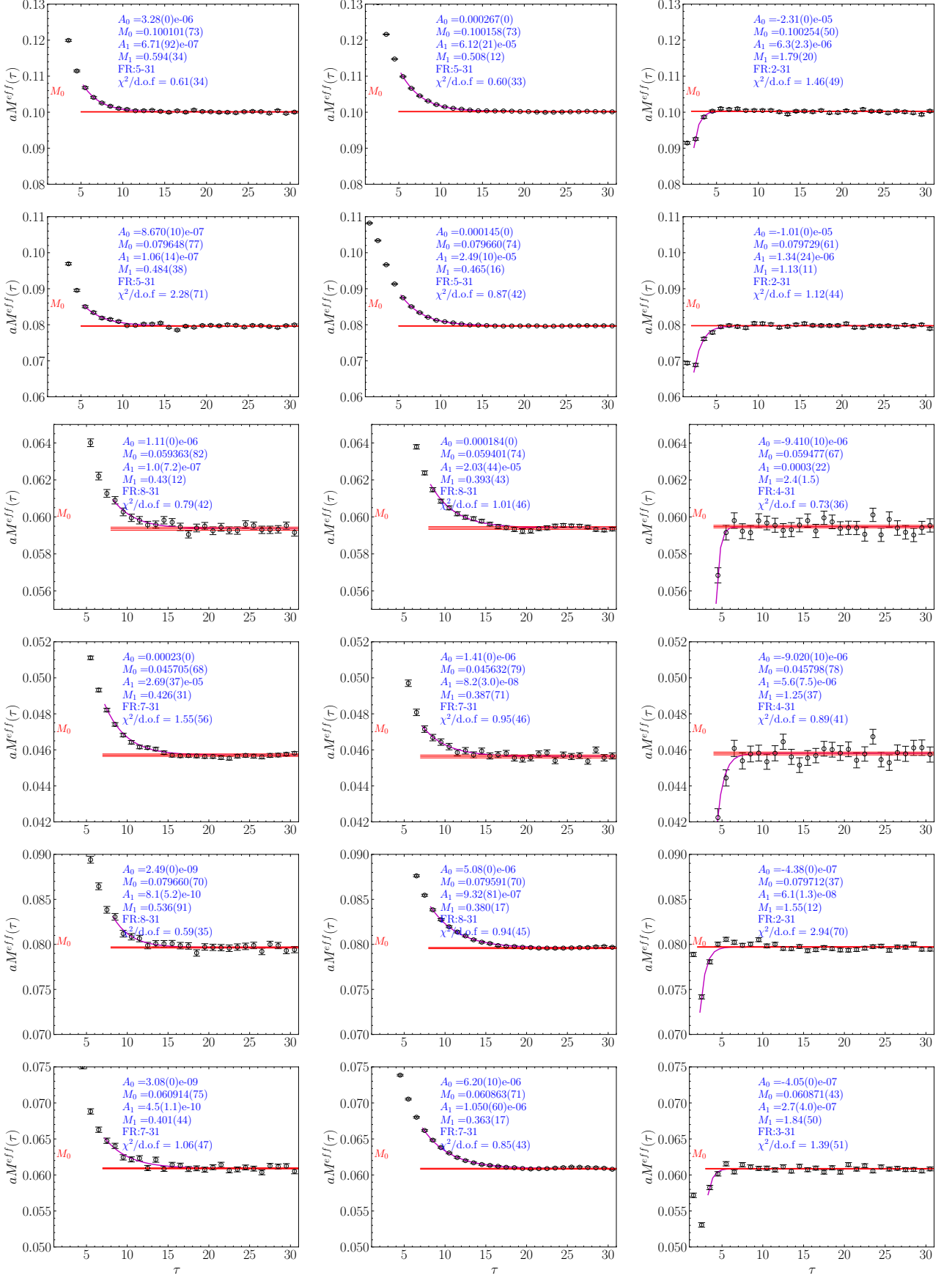


FIG. 13. The pion effective mass data and the two-state fit on the a068m290 (top), a068m230 (second), a068m175 (third), a067m135 (fourth), a053m295 (fifth), and a053m230 (bottom) ensembles. The rest is the same as in Fig. 12.

Appendix B: Theta and Weinberg operators under gradient flow

This Appendix presents, in Figs. 14–17, the evolution of the distribution of Q as a function of the flow time t_{gf} , and the time histories of the topological charge Q and the Weinberg operator W at large flow times for the eleven ensembles. From these figures, we infer the following features:

- No freezing of the Q or W is observed as $M_\pi \rightarrow 135$ MeV or/and as $a \rightarrow 0$ even at large flow times.
- The distribution of Q stabilizes much before it converges to an integer. This, as described in Ref. [46], is sufficient for extracting a robust value for the topological susceptibility and for the measurement of the correlation of Q with nucleon 3-point functions needed, for example, for calculating the contribution of the Θ and Weinberg operators to the neutron electric dipole moment.
- There is little change in the distribution profile of Q in the three ensembles $a087m290L$, $a087m230$ and $a087m230X$ that have the same lattice volume ($48^3 \times 128$) (see Fig. 15), whereas it broadens with an increase in the volume as inferred from Fig. 16 by moving from $a068m290 \rightarrow a067m230 \rightarrow a067m175 \rightarrow a067m135$ data.

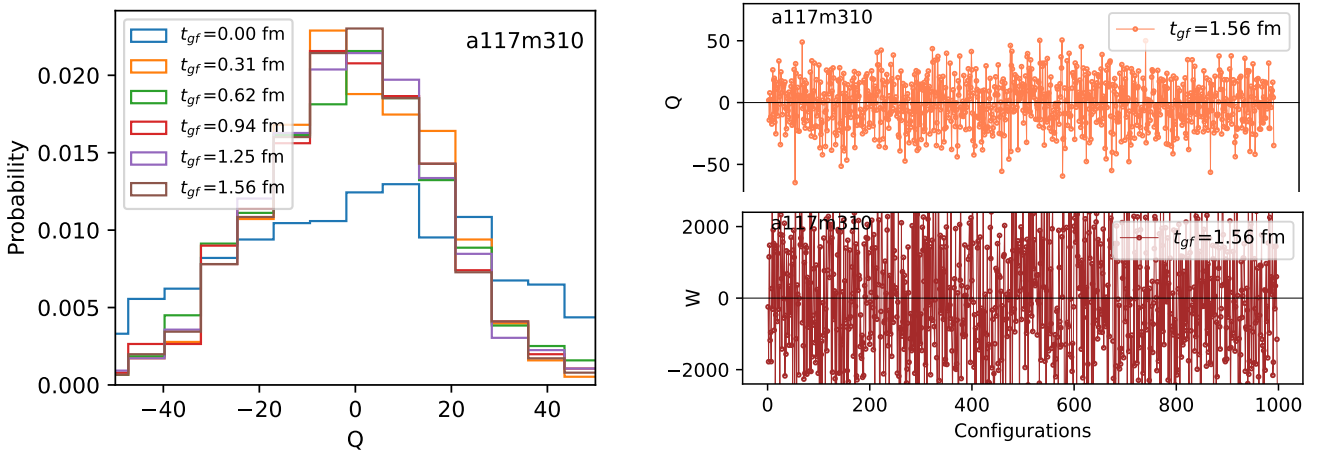


FIG. 14. (Left) Histogram of the distribution of the topological charge Q at different flow times t_{gf} specified in the legend for the $a117m310$ ensemble. (Right) The Monte Carlo time history of the Q (top) and the Weinberg operator W (bottom). The flow times, t_{gf} in fermi, at which data are presented are specified in the labels.

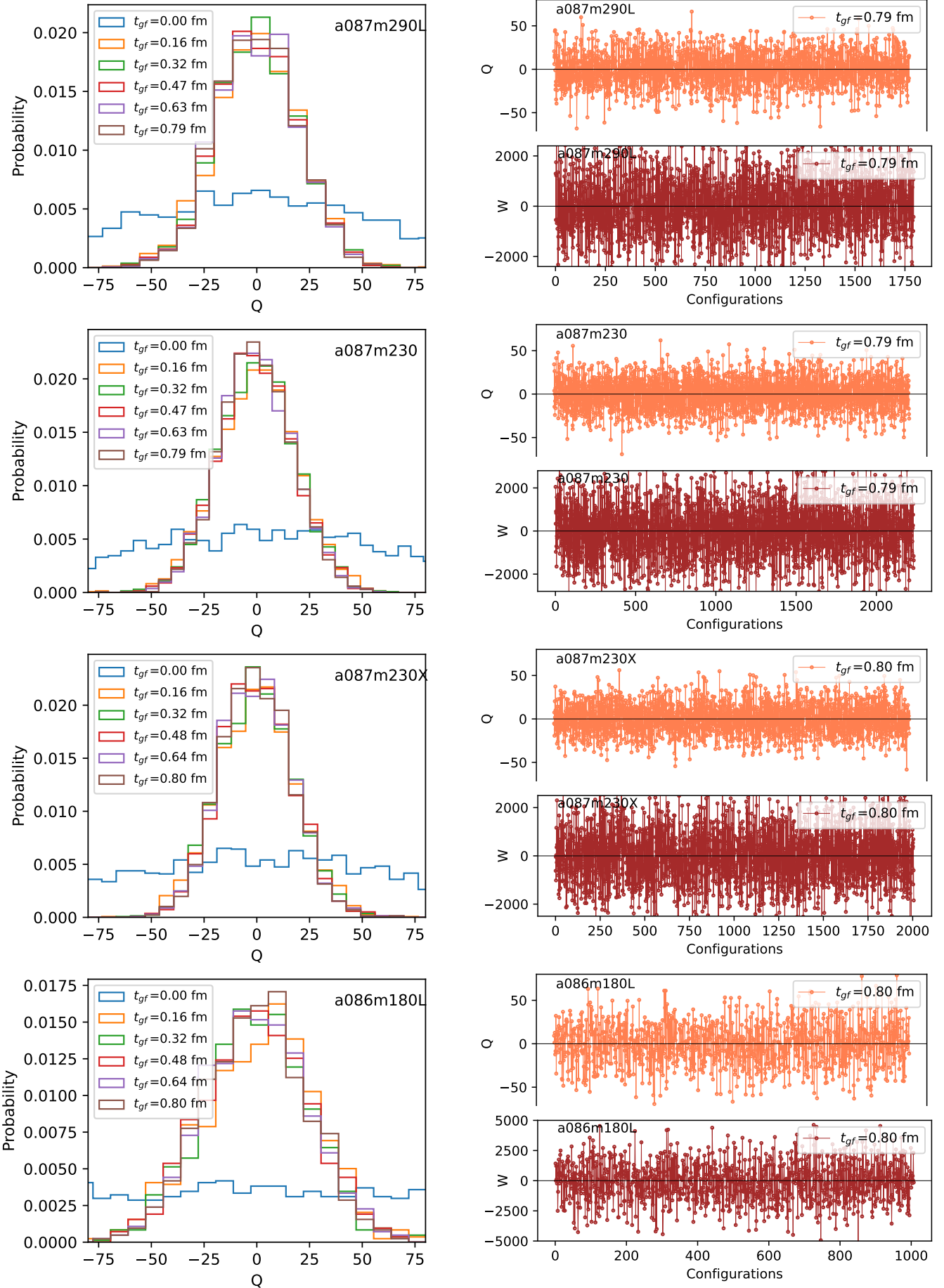


FIG. 15. Same as in Fig. 14 except data are for ensembles $a087m290L$ (top); $a087m230$ (second); $a087m230X$ (third); and $a086m180L$ (bottom). The flow times, t_{gf} in fermi, at which data are presented are specified in the labels.

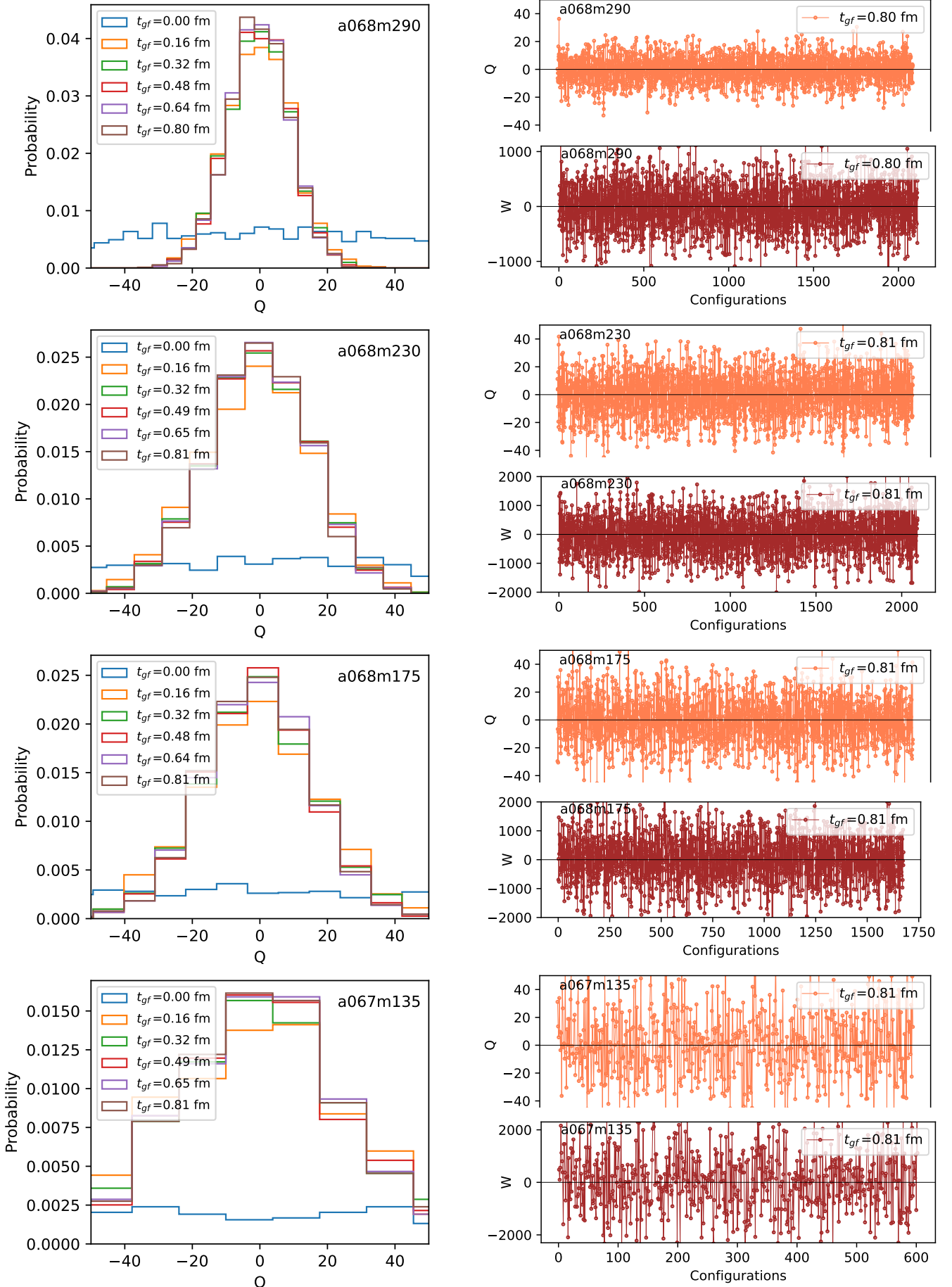


FIG. 16. Same as in Fig. 14 but for ensembles $a068m290$ (top); $a068m230$ (second); $a068m175$ (third); and $a067m135$ (bottom). The flow times, t_{gf} in fermi, at which data are presented are specified in the labels.

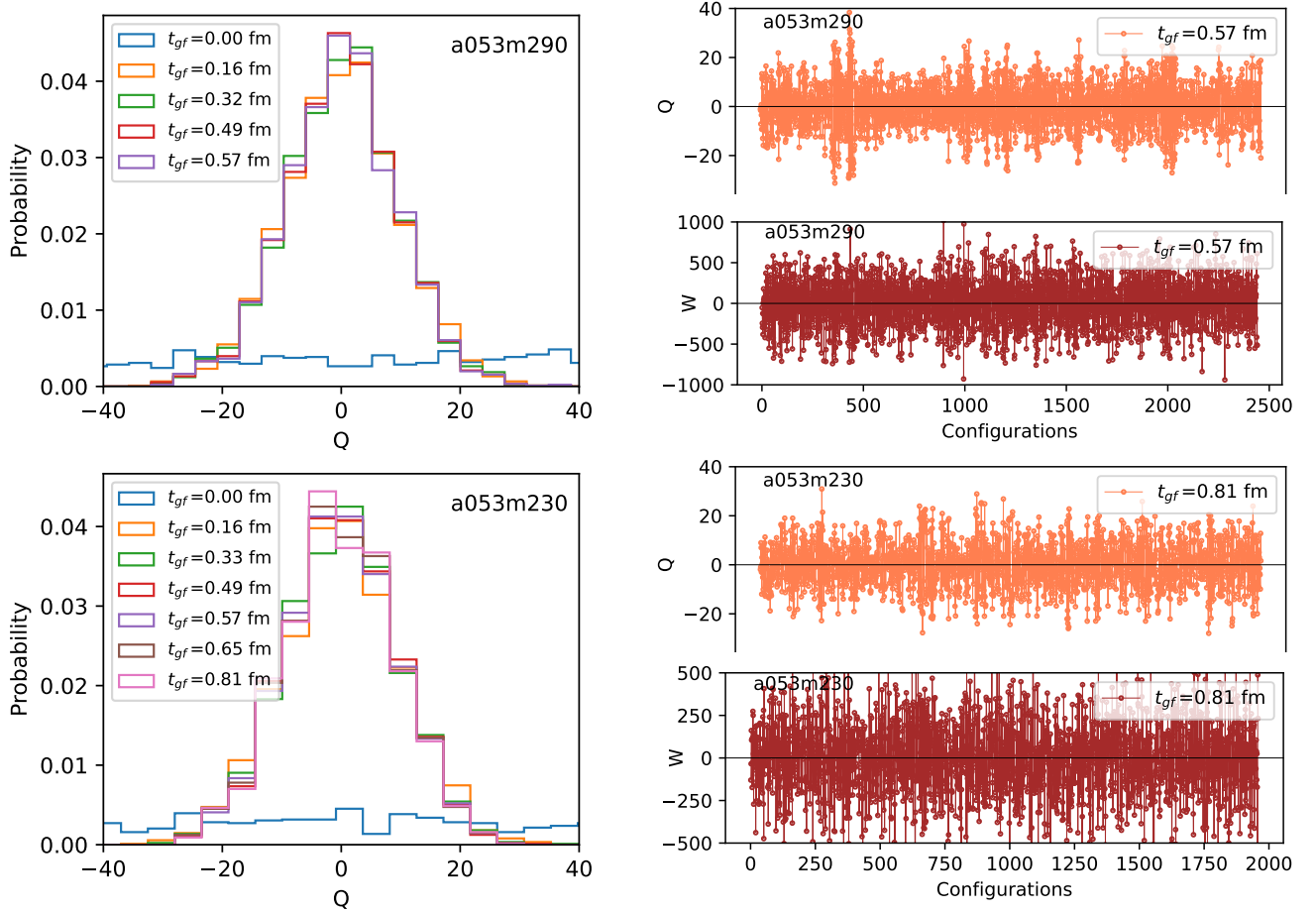


FIG. 17. Same as Fig. 14 but for ensembles $a053m295$ (top) and $a053m230$ (bottom). The flow times, t_{gf} in fermi, at which data are presented are specified in the labels.

Appendix C: Handling Autocorrelations in the Data

Measurements made on configurations generated sequentially in Monte Carlo time are very often correlated. To determine the size of these correlations from N sequential measurements, the autocorrelation function of an observables A is calculated as

$$\Gamma_A(t) = \frac{1}{N-t} \sum_{t_0=1}^{N-t} (A_{t_0+t} - \langle A \rangle)(A_{t_0} - \langle A \rangle), \quad (\text{C1})$$

and modeled as

$$\rho_A(t) = \frac{\Gamma_A(t)}{\Gamma_A(0)} = \sum_k c_{A,k}^2 e^{-|t|/\tau_k} \quad (\text{C2})$$

where τ_k is the autocorrelation time for mode k . Using this, the integrated autocorrelation time (ICT), $\tau_{A,int}$, is taken to be

$$\begin{aligned} \tau_{A,ICT} &\equiv \frac{1}{2} \int_{-\infty}^{\infty} dt \rho_A(t) \\ &= \sum_k c_{A,k}^2 \tau_k. \end{aligned} \quad (\text{C3})$$

We show the autocorrelation function using the precise data for the flow variables w_0 and t_0 stored after each trajectory, except for five streams specified in Table XIX, for each stream of the 11 ensembles in Figs. 18–19. The calculated ICT for w_0 and t_0 , given in Table XIX, are large. Also note the still un-understood variations in the autocorrelation function for the different streams generated on the same computer and over roughly the same interval of time. These are large in the *a067m135* and *a053m295* data.

For the analysis of the data for mesons and baryons, we start with configuration averages, i.e., we first average over the $N_{\text{src}}^{\text{LP}} \times N_{\text{src}}$ measurements. For $\Gamma_\pi(\tau = 1.4)$ fm data, the ICT was found to be smaller than 10 trajectories, and for the nucleon using $\Gamma_N(\tau = 0.9)$ fm data it was less than 5 trajectories. To account for these correlations, we further bin the configuration average data using the bin size N_{bin} specified in Table III. On performing all analyses using these binned data, no augmentation of the resulting statistical errors is considered necessary.

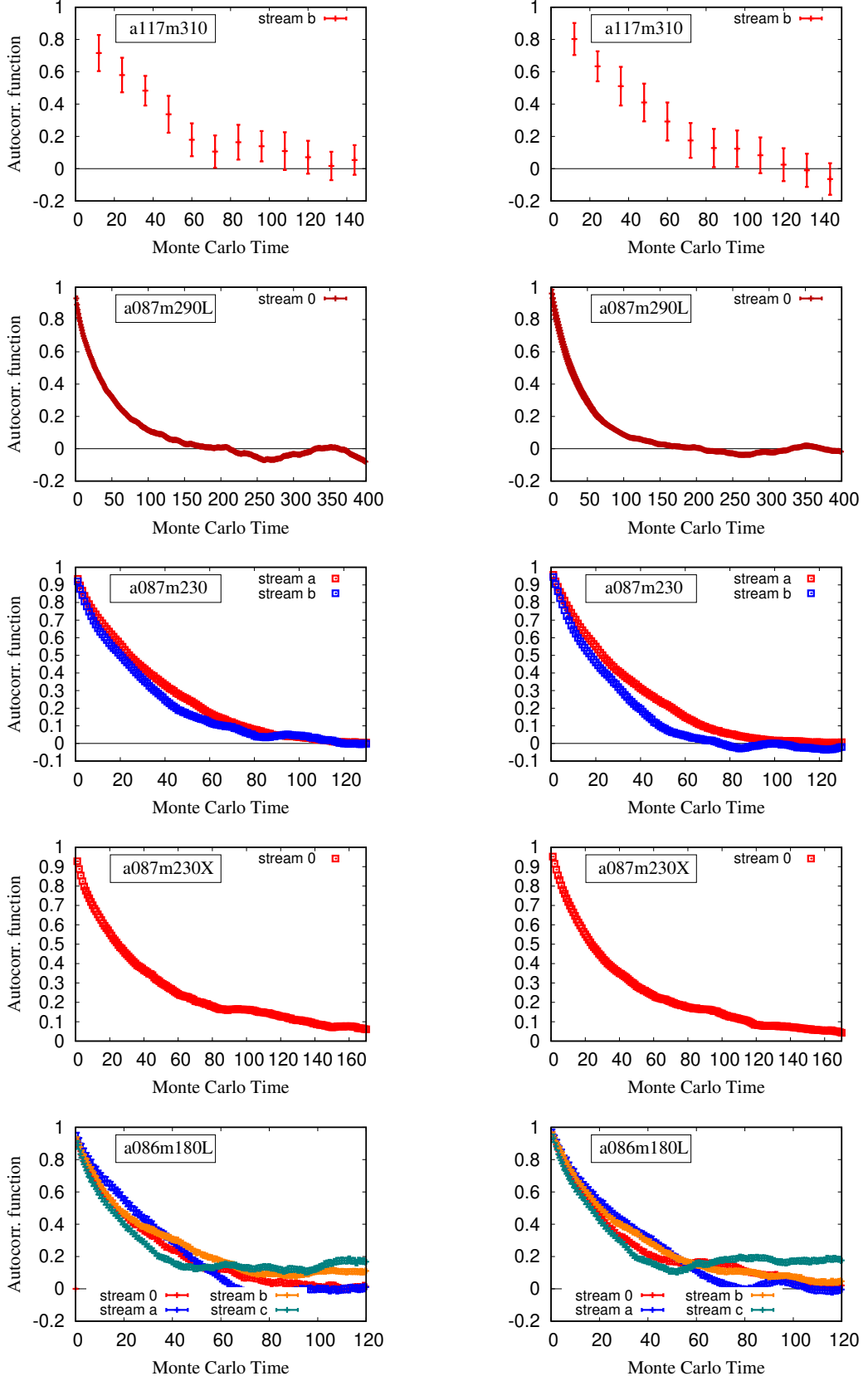


FIG. 18. The autocorrelation function for w_0 (left) and t_0 (right) plotted versus the Monte Carlo (trajectory) time for ensembles $a117m310$ (top), $a086m290$ (second), $a087m230$ (third), $a087m230X$ (fourth) and $a086m180L$ (bottom). The integrated autocorrelation time is calculated from it using Eq. (C3) and given in Table XIX.

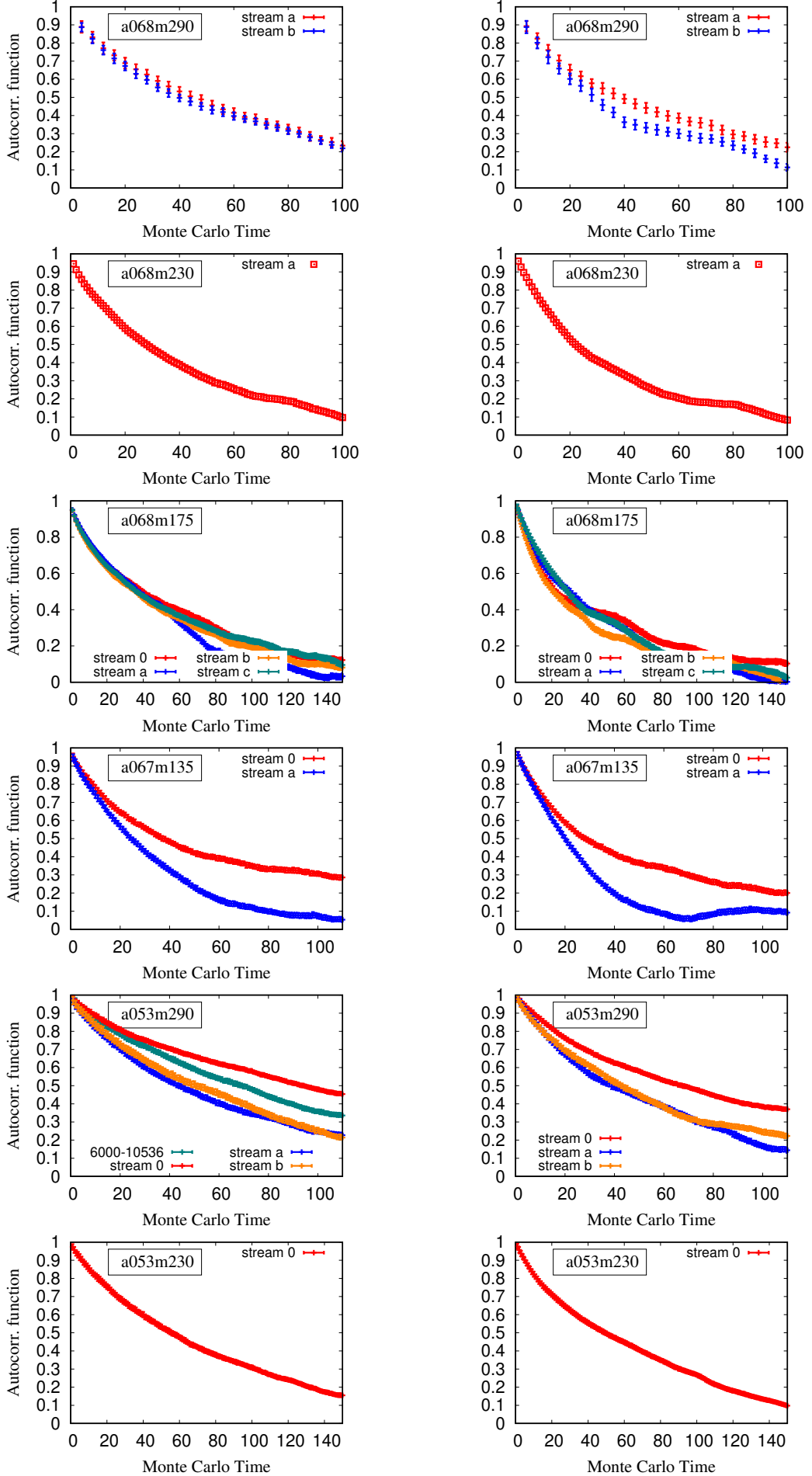


FIG. 19. The autocorrelation function for w_0 (left) and t_0 (right) plotted versus the Monte Carlo (trajectory) time for ensembles a068m290, a068m230, a068m175, a067m135, a053m290, and a053m230. Stream 0 (red line) and stream a (blue line) are shown. Stream b (orange line) is also shown in the a068m175 and a067m135 plots. Stream c (green line) is also shown in the a068m175 and a067m135 plots. The x-axis is Monte Carlo Time and the y-axis is Autocorr. function.

Ens. ID	streams	trajectory interval used for calculating τ_{int}	Files with t_0 and w_0 data stored every # trajectories	IAC time	
				τ_{w_0}	τ_{t_0}
$a117m310\dagger$	0, a				
$a117m310^*$	b	2374 - 3310	12	43	47
$a087m290$	0	2010 -6020	4,6	45	49
$a087m290L$	0	1 - 14340	1	44	42
$a087m230$	a	1-12154	1	34	33
$a087m230$	b	659-9245	1	28	26
$a087m230X$	s	1-12670††	1	46	45
$a086m180 \dagger$	0, a, b				
$a086m180$	c	4-2848	4	23	22
$a086m180 \dagger$	d,e,f,g				
$a086m180L$	0	4047 - 6896	1	27	26
$a086m180L$	a	3323 - 5838	1	31	33
$a086m180L$	b	2947 - 6970	1	34	32
$a086m180L$	c	3287 - 6776	1	22	23
$a068m290 \dagger$	0				
$a068m290$	a	200-8224	4	55	63
$a068m290$	b	4-13796	4	68	45
$a068m230$	0	1 - 10896	1	40	40
$a068m230 \dagger$	a	802-3068			
$a068m175$	0	1 - 348, 541-5640	1	62	56
$a068m175$	a	1 - 5516	1	50	45
$a068m175$	b	1 - 5544	1	54	40
$a068m175$	c	1 - 5508	1	58	46
$a067m135$	0	767 - 6400	1	85	70
$a067m135$	a	1 - 5210	1	34	26
$a053m295$	0	337-10536	1	181	108
$a053m295$	a	1-5624	1	63	63
$a053m295$	b	1-5376	1	74	62
$a053m230$	0	1-11306	1	79	76
$a053m230 \dagger$	a	802-2816			

TABLE XIX. The integrated autocorrelation (IAC) time τ , in units of the molecular dynamics (MD) trajectories of roughly unit length, calculated using w_0 and t_0 . A symbol \dagger in the ensemble ID implies log files with flow data were lost. The τ on C13(b) is evaluated using 75 configurations separated by 12 MD units. The τ for stream F5(0) is much larger, mostly arising from correlations on the first 6000 trajectories. The spectrum and topology data on these trajectories do not, however, show any significant deviation-from-mean behavior. We also note that estimates from w_0 and t_0 are similar in almost all cases. The calculations of 2- and 3-point functions is done on configurations separated by four trajectories except for ensemble $a068m290$ where measurements were made every 6 trajectories.

Appendix D: Baryon Effective Mass Plots and Extracting Masses

In Figs. 20–21, we present the data for M_{eff} for the nucleon along with 3- and 4-state fits using Eq. (3). We expect good consistency between estimates for the ground state results, M_0 and A_0 , and rough agreement for the first excited-state values, M_1 and A_1 . A reasonable length plateau is observed in M_{eff} for all the ensembles and the estimates of the ground-state mass, M_0 , and the amplitude, A_0 , agree between the 3-state and 4-state fits. The χ^2/dof increases slightly for the 4-state fits while the estimate for M_0 is $(1-2)\sigma$ larger in the two-state fits. Using both the Akaike criteria (requiring χ^2 to decrease by two units for each extra parameter) and the observed convergence in M_0 from above, we take results of the 3-state fits for our best estimates.

The data also show that the results for the first excited state, $\Delta M_1 \equiv M_1 - M_0$ and $R_1 \equiv A_1/A_0$, are also consistent except for the $a087m290L$ and $a067m175$ ensembles. We are investigating these cases, however, note that in this paper we only use the ground-state parameters. The estimates for the second excited state differ. This is not unexpected—for any n -state fit, the parameters of the n^{th} state try to accommodate all the higher states. In short, only the ground and first excited state parameters in 3-state fits are expected to be useful.

A comparison of the effective mass plots for the five baryon states, $\{\Omega_3, \Xi_1, \Sigma_6, \Lambda_3, N_6\}$, is shown in Figs. 22 and 23. The labels specify the ensemble and the subscript on the state, e.g., in Ω_3 , specifies the interpolation operator used as defined in Table XX. The horizontal dashed lines give the ground-state mass, M_0 , obtained from 2-state fits. Comparing the data from the SS (left) and SP (right) correlators, we note that the errors in $M_{eff}(\tau)$ at a given τ are smaller in the SP data whereas the plateau sets in slightly earlier in τ in the SS data. Estimates of M_0 overlap.

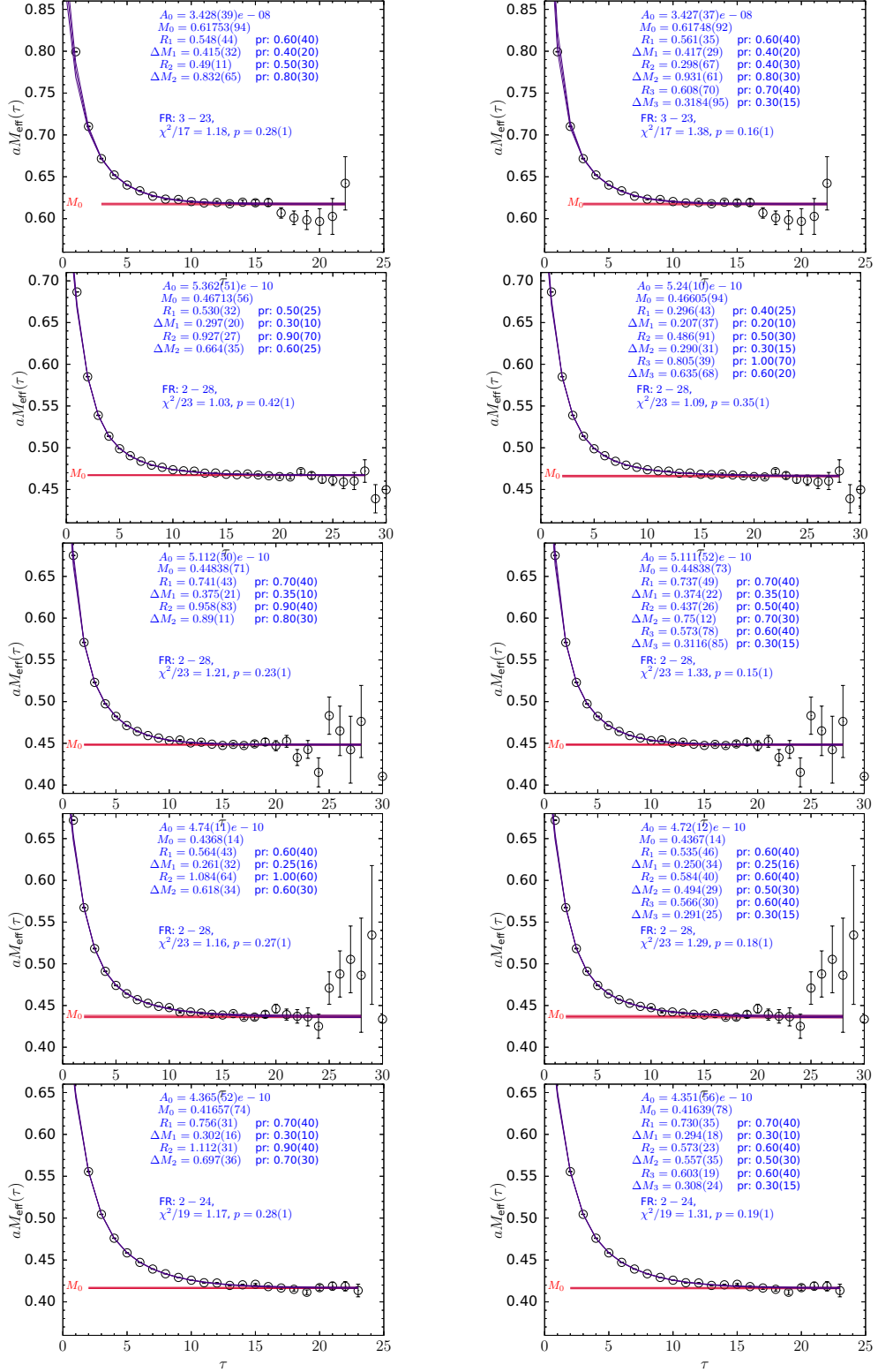


FIG. 20. Data for $aM_{eff}(\tau)$ for the nucleon using the N_3 operator and SS correlators, along with 3-state (left) and 4-state (right) fits on a117m310 (top), a086m290 (second), a087m230 (third), a087m230X (fourth) and a086m180L (bottom) ensembles. The fit parameters and the input priors (pr) are given in the labels with $\Delta M_i \equiv M_i - M_{i-1}$, $R_i \equiv A_i/A_0$. FR is short for the fit range and M_0 is the ground-state mass.

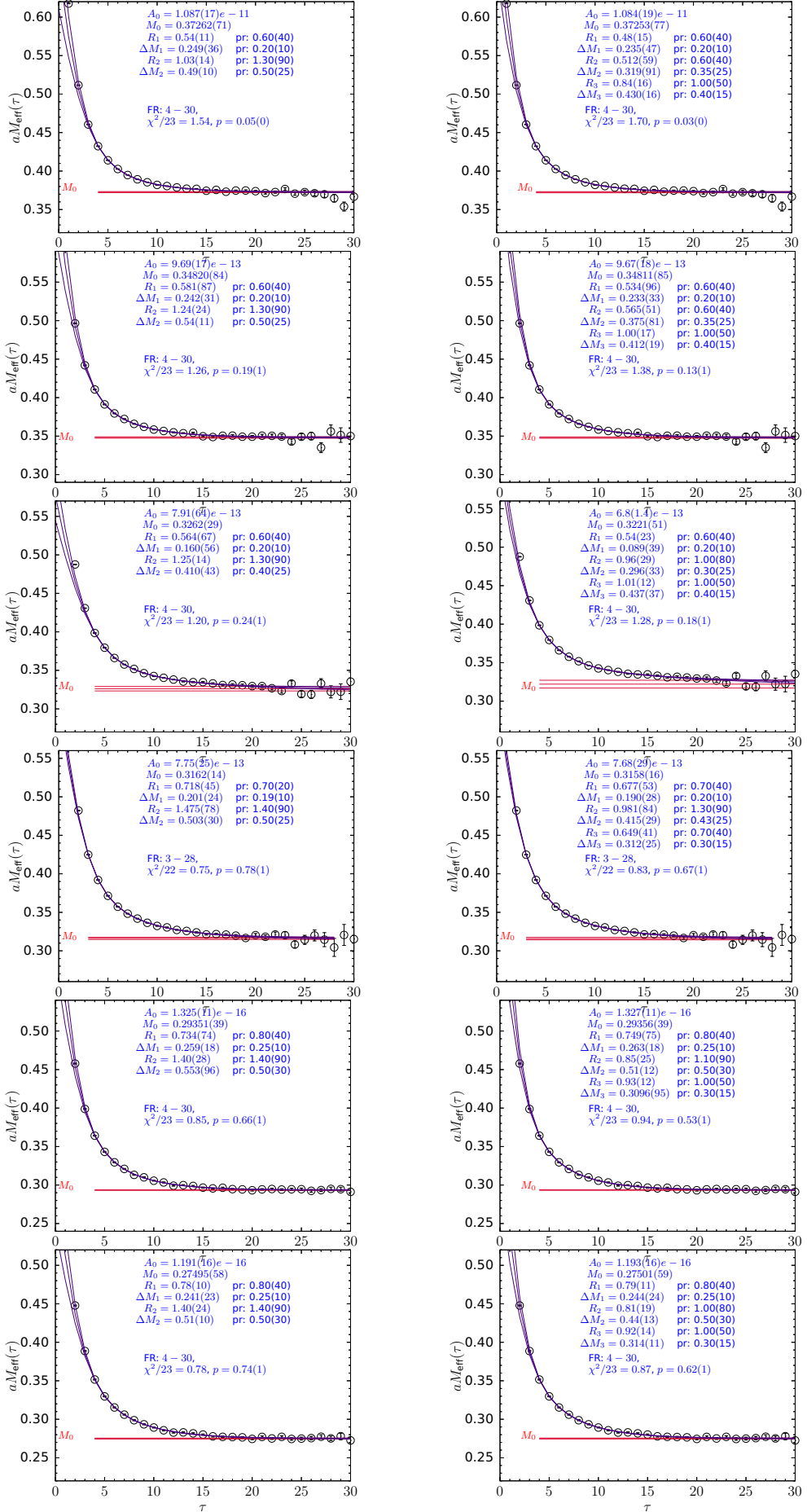


FIG. 21. Data for $aM_{\text{eff}}^{\text{nucleon}}(\tau)$ with 3-state (left) and 4-state (right) fits on $a068m290$ (top), $a068m230$ (second), $a068m175$ (third), $a067m135$ (fourth), $a053m295$ (fifth) and $a053m230$ (bottom) ensembles. The rest is same as in Fig. 20.

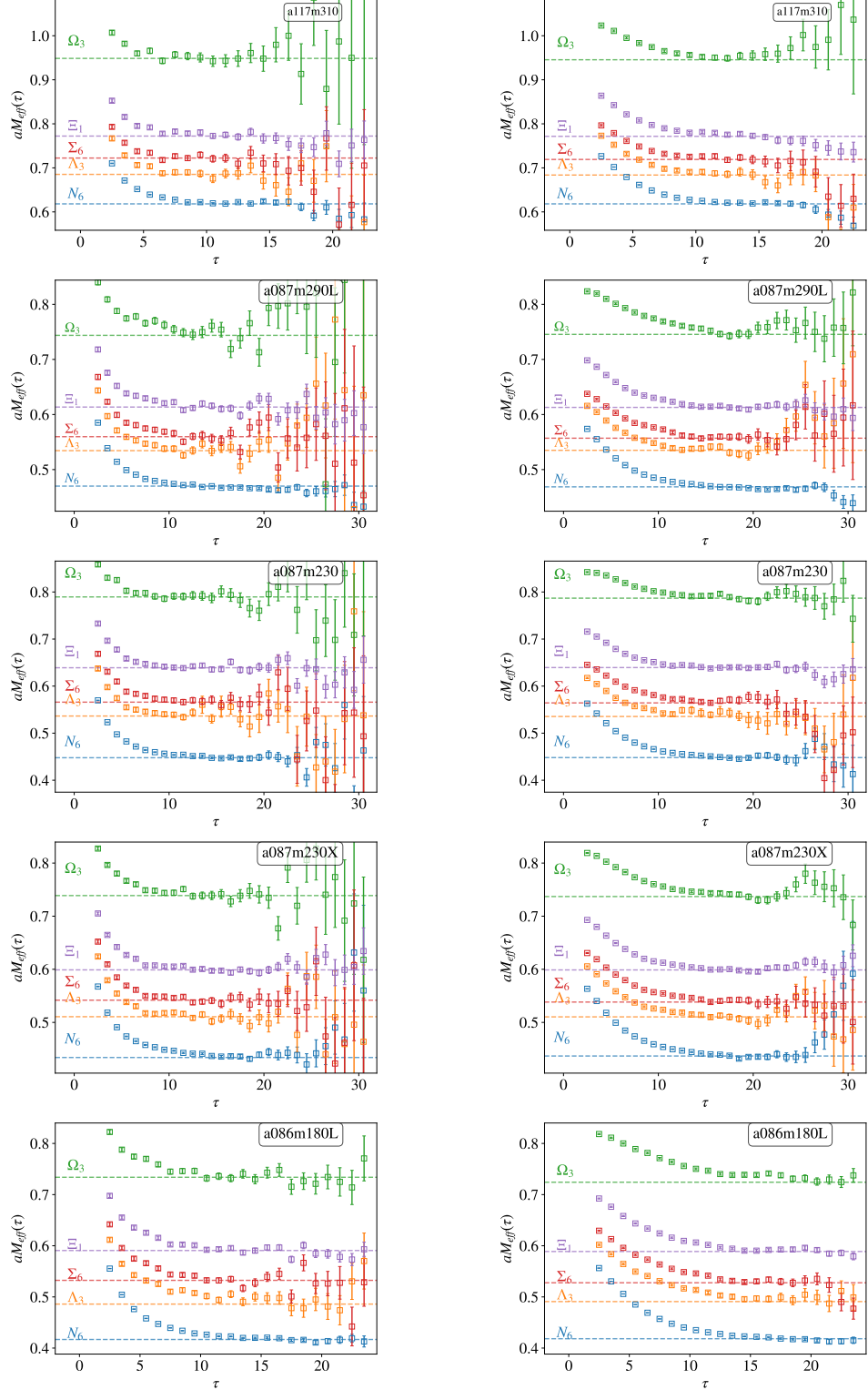


FIG. 22. Effective mass plots for the five baryon states, $\{\Omega_3, \Xi_1, \Sigma_6, \Lambda_3, N_6\}$, using the SS (left) and SP (right) correlators. The labels specify the ensemble and the baryon state, e.g., Ω_3 , specifies the interpolation operator used as defined in Table XX. The horizontal dashed lines give the ground-state mass obtained from 2-state fits.

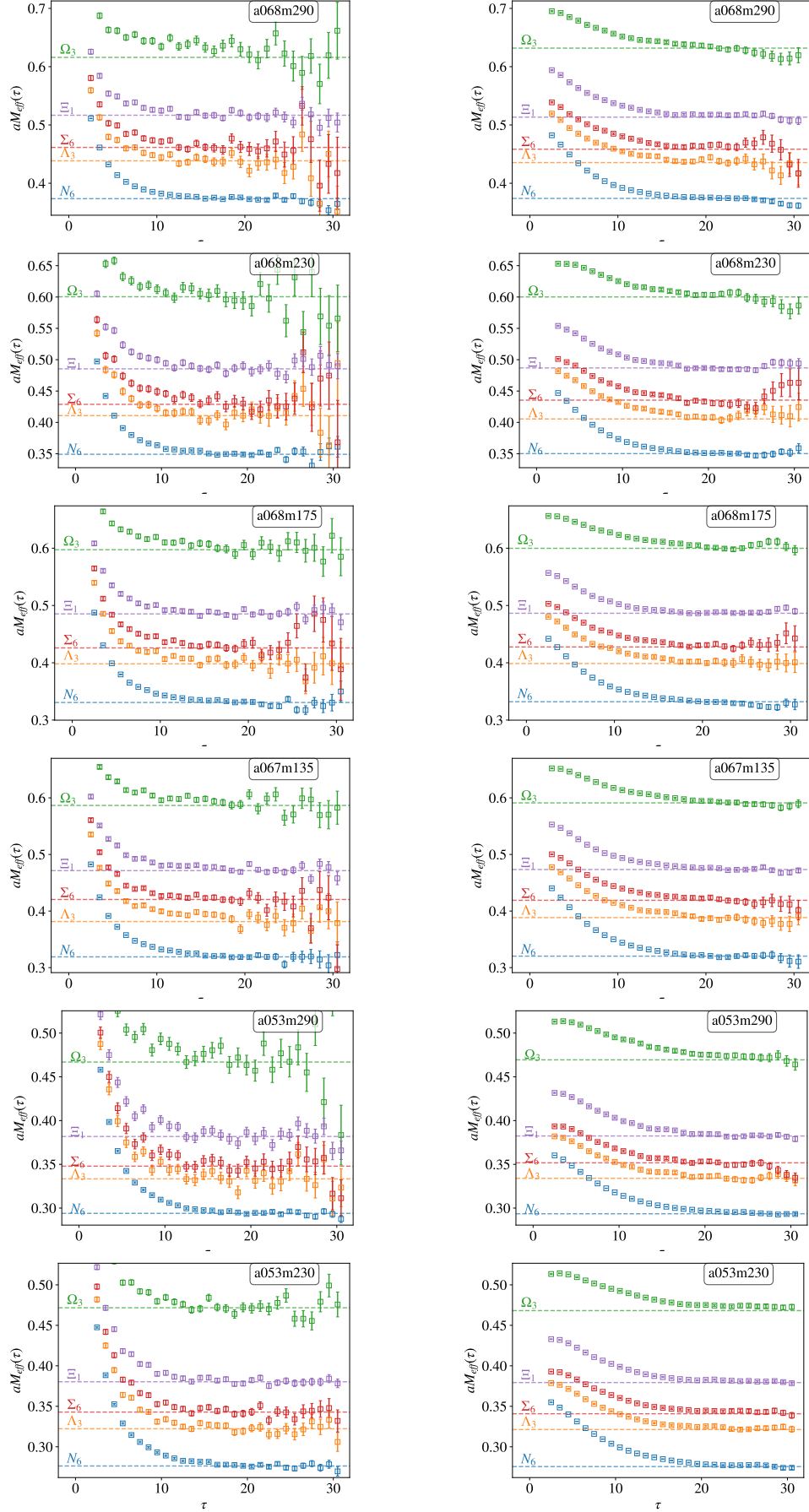


FIG. 23. Effective mass plots for the five baryon states, $\{\Omega_3, \Xi_1, \Sigma_6, \Lambda_3, N_6\}$, using the SS (left) and SP (right) correlators. The labels specify the ensemble and the state, e.g., Ω_3 , specifies the interpolation operator used as defined in Table XX. The horizontal dashed lines give the ground-state mass obtained from 2-state fits.

Appendix E: Meson and Baryon Interpolating Operators Used

The interpolating operators used to study the mesons and baryons are written as

$$\chi_f^M = (\bar{q}_1 S q_2), \quad \chi_f^B = (\bar{q}_1 S q_2) q_3. \quad (\text{E1})$$

In terms of these, the two-point correlators are

$$C_{2pt}^M = \langle \chi_f \bar{\chi}_f \rangle, \quad C_{2pt}^B = T \langle \chi_f \bar{\chi}_f \rangle \quad (\text{E2})$$

with the matrices S and T for the various operators are defined in Table XX.

State	S	T
π_1	γ_5	
π_2	$\gamma_4 \gamma_5$	
ρ_1	γ_i	
ρ_2	$\gamma_4 \gamma_i$	
N_1	$C \gamma_5$	$(1 + \Sigma_3) \frac{1+\gamma_4}{2}$
N_2	$C \gamma_5 \gamma_4$	$(1 + \Sigma_3) \frac{1+\gamma_4}{2}$
N_3	$C \gamma_5 \frac{1+\gamma_4}{2}$	$(1 + \Sigma_3) \frac{1+\gamma_4}{2}$
N_4	$C \gamma_5$	$\frac{1+\gamma_4}{2}$
N_5	$C \gamma_5 \gamma_4$	$\frac{1+\gamma_4}{2}$
N_6	$C \gamma_5 \frac{1+\gamma_4}{2}$	$\frac{1+\gamma_4}{2}$
Δ_1	$C \gamma_-$	$(1 + \Sigma_3) \frac{1+\gamma_4}{2}$
Δ_2	$C \gamma_4 \gamma_-$	$(1 + \Sigma_3) \frac{1+\gamma_4}{2}$
Δ_3	$C \frac{1+\gamma_4}{2} \gamma_-$	$(1 + \Sigma_3) \frac{1+\gamma_4}{2}$
Ω_1	$C \gamma_-$	$(1 + \Sigma_3) \frac{1+\gamma_4}{2}$
Ω_2	$C \gamma_4 \gamma_-$	$(1 + \Sigma_3) \frac{1+\gamma_4}{2}$
Ω_3	$C \frac{1+\gamma_4}{2} \gamma_-$	$(1 + \Sigma_3) \frac{1+\gamma_4}{2}$
Σ_1	$C \gamma_5$	$(1 + \Sigma_3)(1+\gamma_4)/2$
Σ_2	$C \gamma_5 \gamma_4$	$(1 + \Sigma_3)(1+\gamma_4)/2$
Σ_3	$C \gamma_5 (1+\gamma_4)/2$	$(1 + \Sigma_3)^*(1+\gamma_4)/2$
Σ_4	$C \gamma_5$	$(1+\gamma_4)/2$
Σ_5	$C \gamma_5 \gamma_4$	$(1+\gamma_4)/2$
Σ_6	$C \gamma_5 (1+\gamma_4)/2$	$(1+\gamma_4)/2$
Λ_1	$C \gamma_5$	$(1 + \Sigma_3)(1+\gamma_4)/2$
Λ_2	$C \gamma_5 \gamma_4$	$(1 + \Sigma_3)(1+\gamma_4)/2$
Λ_3	$C \gamma_5 (1+\gamma_4)/2$	$(1 + \Sigma_3)(1+\gamma_4)/2$
Λ_4	$C \gamma_5$	$(1+\gamma_4)/2$
Λ_5	$C \gamma_5$	$(1 + \Sigma_3)(1+\gamma_4)/2$
Ξ_1	$C \gamma_5$	$(1+\gamma_4)/2$
Ξ_2	$C \gamma_5$	$(1 + \Sigma_3)(1+\gamma_4)/2$
Σ_1^*	$C \gamma_-$	$(1 + \Sigma_3)(1+\gamma_4)/2$
Σ_2^*	$C \gamma_5 \gamma_-$	$(1 + \Sigma_3)(1+\gamma_4)/2$
Σ_3^*	$C \gamma_5 (1+\gamma_4) \gamma_-/2$	$(1 + \Sigma_3)(1+\gamma_4)/2$
Ξ_1^*	$C \gamma_-$	$(1 + \Sigma_3)(1+\gamma_4)/2$
Ξ_2^*	$C \gamma_4 \gamma_-$	$(1 + \Sigma_3)(1+\gamma_4)/2$
Ξ_3^*	$C (1+\gamma_4) \gamma_-/2$	$(1 + \Sigma_3)(1+\gamma_4)/2$

TABLE XX. The matrix S in Eq. E1 used to define the meson and baryon interpolating operators used in Eq. (E2), and the projection matrix T for the 2-point function. The pseudoscalar and vector mesons are labeled, generically, by π and ρ . Note that $C = \gamma_2 \gamma_4$, $C \gamma_5 = \gamma_1 \gamma_3$, $\Sigma_3 = -i \gamma_1 \gamma_2$ and $\gamma_- = \frac{1}{2}(\gamma_2 + i \gamma_1)$. These matrices are the same for the Δ and Ω states.

[1] S. Duane, A. D. Kennedy, B. J. Pendleton, and D. Roweth, Hybrid Monte Carlo, *Phys. Lett. B* **195**, 216 (1987).

[2] T. Bhattacharya, R. Gupta, W. Lee, and S. R. Sharpe, Scaling behavior of discretization errors in renormalization and improvement constants, *Phys. Rev. D* **73**, 114507 (2006), arXiv:hep-lat/0509160.

[3] B. Yoon *et al.*, Controlling Excited-State Contamination in Nucleon Matrix Elements, *Phys. Rev. D* **93**, 114506 (2016), arXiv:1602.07737 [hep-lat].

[4] B. Yoon *et al.*, Isovector charges of the nucleon from 2+1-flavor QCD with clover fermions, *Phys. Rev. D* **95**, 074508 (2017), arXiv:1611.07452 [hep-lat].

[5] S. Park, R. Gupta, B. Yoon, S. Mondal, T. Bhattacharya, Y.-C. Jang, B. Joó, and F. Winter (Nucleon Matrix Elements (NME)), Precision nucleon charges and form factors using (2+1)-flavor lattice QCD, *Phys. Rev. D* **105**, 054505 (2022), arXiv:2103.05599 [hep-lat].

[6] S. Mondal, R. Gupta, S. Park, B. Yoon, T. Bhattacharya, B. Joó, and F. Winter (Nucleon Matrix Elements (NME)), Nucleon momentum fraction, helicity and transversity from 2+1-flavor lattice QCD, *JHEP* **21**, 004, arXiv:2011.12787 [hep-lat].

[7] R. G. Edwards and B. Joo (SciDAC, LHPC, UKQCD), The Chroma software system for lattice QCD, *Nucl. Phys. B Proc. Suppl.* **140**, 832 (2005), arXiv:hep-lat/0409003.

[8] J. Bálint, R. Edwards, K. Orginos, and D. Richards, Unpublished.

[9] B. Sheikholeslami and R. Wohlert, Improved Continuum Limit Lattice Action for QCD with Wilson Fermions, *Nucl. Phys. B* **259**, 572 (1985).

[10] J. Bulava and S. Schaefer, Improvement of $N_f = 3$ lattice QCD with Wilson fermions and tree-level improved gauge action, *Nucl. Phys. B* **874**, 188 (2013), arXiv:1304.7093 [hep-lat].

[11] M. Lüscher, S. Sint, R. Sommer, P. Weisz, and U. Wolff, Nonperturbative O(a) improvement of lattice QCD, *Nucl. Phys. B* **491**, 323 (1997), arXiv:hep-lat/9609035.

[12] C. Morningstar and M. J. Peardon, Analytic smearing of SU(3) link variables in lattice QCD, *Phys. Rev. D* **69**, 054501 (2004), arXiv:hep-lat/0311018.

[13] M. Hasenbusch and K. Jansen, Speeding up the Hybrid Monte Carlo algorithm for dynamical fermions, *Nucl. Phys. B Proc. Suppl.* **106**, 1076 (2002), arXiv:hep-lat/0110180.

[14] C. Urbach, K. Jansen, A. Shindler, and U. Wenger, HMC algorithm with multiple time scale integration and mass preconditioning, *Comput. Phys. Commun.* **174**, 87 (2006), arXiv:hep-lat/0506011.

[15] J. C. Sexton and D. H. Weingarten, Hamiltonian evolution for the hybrid Monte Carlo algorithm, *Nucl. Phys. B* **380**, 665 (1992).

[16] M. A. Clark, B. Joo, A. D. Kennedy, and P. J. Silva, Improving dynamical lattice QCD simulations through integrator tuning using Poisson brackets and a force-gradient integrator, *Phys. Rev. D* **84**, 071502 (2011), arXiv:1108.1828 [hep-lat].

[17] H. Yin and R. D. Mawhinney, Improving DWF Simulations: the Force Gradient Integrator and the Möbius Accelerated DWF Solver, *PoS LATTICE2011*, 051 (2011), arXiv:1111.5059 [hep-lat].

[18] R. C. Brower, T. Ivanenko, A. R. Levi, and K. N. Orginos, Chronological inversion method for the Dirac matrix in hybrid Monte Carlo, *Nucl. Phys. B* **484**, 353 (1997), arXiv:hep-lat/9509012.

[19] J. Brannick, R. C. Brower, M. A. Clark, J. C. Osborn, and C. Rebbi, Adaptive Multigrid Algorithm for Lattice QCD, *Phys. Rev. Lett.* **100**, 041601 (2008), arXiv:0707.4018 [hep-lat].

[20] M. A. Clark, B. Joó, A. Strelchenko, M. Cheng, A. Gambhir, and R. C. Brower (QUADA), Accelerating lattice QCD multigrid on GPUs using fine-grained parallelization, in *International Conference for High Performance Computing, Networking, Storage and Analysis* (2016) arXiv:1612.07873 [hep-lat].

[21] R. Babich, J. Brannick, R. C. Brower, M. A. Clark, T. A. Manteuffel, S. F. McCormick, J. C. Osborn, and C. Rebbi, Adaptive multigrid algorithm for the lattice Wilson-Dirac operator, *Phys. Rev. Lett.* **105**, 201602 (2010), arXiv:1005.3043 [hep-lat].

[22] M. A. Clark, R. Babich, K. Barros, R. C. Brower, and C. Rebbi (QUADA), Solving Lattice QCD systems of equations using mixed precision solvers on GPUs, *Comput. Phys. Commun.* **181**, 1517 (2010), arXiv:0911.3191 [hep-lat].

[23] S. Gusken, K. Schilling, R. Sommer, K. H. Mutter, and A. Patel, Mass Splittings in the Baryon Octet and the Nucleon σ Term in Lattice QCD, *Phys. Lett. B* **212**, 216 (1988).

[24] R. Gupta, Y.-C. Jang, B. Yoon, H.-W. Lin, V. Cirigliano, and T. Bhattacharya, Isovector Charges of the Nucleon from 2+1+1-flavor Lattice QCD, *Phys. Rev. D* **98**, 034503 (2018), arXiv:1806.09006 [hep-lat].

[25] S. Mondal, R. Gupta, S. Park, B. Yoon, T. Bhattacharya, and H.-W. Lin, Moments of nucleon isovector structure functions in 2 + 1 + 1-flavor QCD, *Phys. Rev. D* **102**, 054512 (2020), arXiv:2005.13779 [hep-lat].

[26] G. Parisi, The Strategy for Computing the Hadronic Mass Spectrum, *Phys. Rept.* **103**, 203 (1984).

[27] H. W. Hamber, E. Marinari, G. Parisi, and C. Rebbi, Considerations on Numerical Analysis of QCD, *Nucl. Phys. B* **225**, 475 (1983).

[28] G. P. Lepage, The Analysis of Algorithms for Lattice Field Theory, in *Theoretical Advanced Study Institute (TASI) in Elementary Particle Physics, Boulder*. (1989) pp. 97–120.

[29] G. Martinelli, C. Pittori, C. T. Sachrajda, M. Testa, and A. Vladikas, A General method for nonperturbative renormalization of lattice operators, *Nucl. Phys. B* **445**, 81 (1995), arXiv:hep-lat/9411010 [hep-lat].

[30] C. Sturm, Y. Aoki, N. H. Christ, T. Izubuchi, C. T. C. Sachrajda, and A. Soni, Renormalization of quark bilinear operator in a momentum-subtraction scheme with a nonexceptional subtraction point, *Phys. Rev. D* **80**, 014501 (2009), arXiv:0901.2599 [hep-ph].

[31] M. Lüscher, Volume Dependence of the Energy Spectrum in Massive Quantum Field Theories. 2. Scattering States, *Commun. Math. Phys.* **105**, 153 (1986).

[32] G. S. Bali, S. Collins, P. Georg, D. Jenkins, P. Korcyl, A. Schäfer, E. E. Scholz, J. Simeth, W. Söldner, and S. Weishäupl (RQCD), Scale setting and the light baryon

spectrum in $N_f = 2 + 1$ QCD with Wilson fermions, JHEP **05**, 035, arXiv:2211.03744 [hep-lat].

[33] P. Boyle, F. Erben, V. Gülpers, M. T. Hansen, F. Joswig, M. Marshall, N. P. Lachini, and A. Portelli, Light and Strange Vector Resonances from Lattice QCD at Physical Quark Masses, Phys. Rev. Lett. **134**, 111901 (2025), arXiv:2406.19194 [hep-lat].

[34] P. Boyle, F. Erben, V. Gülpers, M. T. Hansen, F. Joswig, M. Marshall, N. P. Lachini, and A. Portelli, Physical-mass calculation of $\rho(770)$ and $K^*(892)$ resonance parameters via $\pi\pi$ and $K\pi$ scattering amplitudes from lattice QCD, Phys. Rev. D **111**, 054510 (2025), arXiv:2406.19193 [hep-lat].

[35] J. J. Dudek, R. G. Edwards, M. J. Peardon, D. G. Richards, and C. E. Thomas, Toward the excited meson spectrum of dynamical QCD, Phys. Rev. D **82**, 034508 (2010), arXiv:1004.4930 [hep-ph].

[36] C. E. Thomas, R. G. Edwards, and J. J. Dudek, Helicity operators for mesons in flight on the lattice, Phys. Rev. D **85**, 014507 (2012), arXiv:1107.1930 [hep-lat].

[37] H. Akaike, A new look at the statistical model identification, IEEE Transactions on Automatic Control **19**, 716 (1974).

[38] J. Gasser and H. Leutwyler, Chiral Perturbation Theory: Expansions in the Mass of the Strange Quark, Nucl. Phys. B **250**, 465 (1985).

[39] O. Bar and M. Golterman, Chiral perturbation theory for gradient flow observables, Phys. Rev. D **89**, 034505 (2014), [Erratum: Phys. Rev. D **89**, 099905 (2014)], arXiv:1312.4999 [hep-lat].

[40] S. Dürr *et al.*, Leptonic decay-constant ratio f_K/f_π from lattice QCD using 2+1 clover-improved fermion flavors with 2-HEX smearing, Phys. Rev. D **95**, 054513 (2017), arXiv:1601.05998 [hep-lat].

[41] E. E. Jenkins and A. V. Manohar, Baryon chiral perturbation theory using a heavy fermion Lagrangian, Phys. Lett. B **255**, 558 (1991).

[42] P. J. Ellis and K. Torikoshi, Baryon masses in chiral perturbation theory with infrared regularization, Phys. Rev. C **61**, 015205 (2000), arXiv:nucl-th/9904017.

[43] Y. Aoki *et al.* (Flavour Lattice Averaging Group (FLAG)), FLAG Review 2024, (2024), arXiv:2411.04268 [hep-lat].

[44] M. Lüscher, Properties and uses of the Wilson flow in lattice QCD, JHEP **08**, 071, [Erratum: JHEP 03, 092 (2014)], arXiv:1006.4518 [hep-lat].

[45] M. Nagatsuka, K. Sakai, and S. Sasaki, Equivalence between the Wilson flow and stout-link smearing, Phys. Rev. D **108**, 094506 (2023), arXiv:2303.09938 [hep-lat].

[46] T. Bhattacharya, V. Cirigliano, R. Gupta, E. Mereghetti, and B. Yoon, Contribution of the QCD Θ -term to the nucleon electric dipole moment, Phys. Rev. D **103**, 114507 (2021), arXiv:2101.07230 [hep-lat].

[47] A. Bazavov, C. Bernard, J. Komijani, C. DeTar, L. Levkova, W. Freeman, S. Gottlieb, R. Zhou, U. M. Heller, J. E. Hetrick, J. Laiho, J. Osborn, R. L. Sugar, D. Toussaint, and R. S. Van de Water (MILC), Lattice QCD ensembles with four flavors of highly improved staggered quarks, Phys. Rev. D **87**, 054505 (2013), arXiv:1212.4768 [hep-lat].

[48] C. Bernard and D. Toussaint (MILC), Effects of nonequilibrated topological charge distributions on pseudoscalar meson masses and decay constants, Phys. Rev. D **97**, 074502 (2018), arXiv:1707.05430 [hep-lat].

[49] S. Park, R. Gupta, T. Bhattacharya, F. He, S. Mondal, H.-W. Lin, and B. Yoon, Flavor diagonal nucleon charges using clover fermions on MILC HISQ ensembles, Phys. Rev. D **112**, 054508 (2025), arXiv:2503.07100 [hep-lat].

[50] B. Strassberger *et al.*, Scale setting for CLS 2+1 simulations, PoS **LATTICE2021**, 135 (2022), arXiv:2112.06696 [hep-lat].

[51] V. Cirigliano and H. Neufeld, A note on isospin violation in $\text{Pl2}(\text{gamma})$ decays, Phys. Lett. B **700**, 7 (2011), arXiv:1102.0563 [hep-ph].

[52] Z.-C. Hu *et al.* (CLQCD), Quark masses and low-energy constants in the continuum from the tadpole-improved clover ensembles, Phys. Rev. D **109**, 054507 (2024), arXiv:2310.00814 [hep-lat].

[53] V. G. Bornyakov, R. Horsley, Y. Nakamura, H. Perlt, D. Pleiter, P. E. L. Rakow, G. Schierholz, A. Schiller, H. Stüben, and J. M. Zanotti (QCDSF-UKQCD), Flavour breaking effects in the pseudoscalar meson decay constants, Phys. Lett. B **767**, 366 (2017), arXiv:1612.04798 [hep-lat].

[54] J. Laiho and R. S. Van de Water, Pseudoscalar decay constants, light-quark masses, and B_K from mixed-action lattice QCD, PoS **LATTICE2011**, 293 (2011), arXiv:1112.4861 [hep-lat].

[55] A. Bazavov *et al.* (MILC), Results for light pseudoscalar mesons, PoS **LATTICE2010**, 074 (2010), arXiv:1012.0868 [hep-lat].

[56] A. Bazavov *et al.* (MILC), MILC results for light pseudoscalars, PoS **CD09**, 007 (2009), arXiv:0910.2966 [hep-ph].

[57] A. Bazavov *et al.* (MILC), Nonperturbative QCD Simulations with 2+1 Flavors of Improved Staggered Quarks, Rev. Mod. Phys. **82**, 1349 (2010), arXiv:0903.3598 [hep-lat].

[58] C. Aubin, J. Laiho, and R. S. Van de Water, Light Pseudoscalar Meson Masses and Decay Constants from Mixed Action Lattice QCD, PoS **LATTICE2008**, 105 (2008), arXiv:0810.4328 [hep-lat].

[59] C. Aubin, C. Bernard, C. E. DeTar, J. Osborn, S. Gottlieb, E. B. Gregory, D. Toussaint, U. M. Heller, J. E. Hetrick, and R. Sugar (MILC), Light pseudoscalar decay constants, quark masses, and low energy constants from three-flavor lattice QCD, Phys. Rev. D **70**, 114501 (2004), arXiv:hep-lat/0407028.

[60] J. Gegelia and G. Japaridze, Matching heavy particle approach to relativistic theory, Phys. Rev. D **60**, 114038 (1999), arXiv:hep-ph/9908377.

[61] L. S. Geng, J. Martin Camalich, and M. J. Vicente Vacas, Leading-order decuplet contributions to the baryon magnetic moments in Chiral Perturbation Theory, Phys. Lett. B **676**, 63 (2009), arXiv:0903.0779 [hep-ph].

[62] J. Martin Camalich, L. S. Geng, and M. J. Vicente Vacas, The lowest-lying baryon masses in covariant SU(3)-flavor chiral perturbation theory, Phys. Rev. D **82**, 074504 (2010), arXiv:1003.1929 [hep-lat].

[63] G. Bali *et al.*, Lattice gauge ensembles and data management, PoS **LATTICE2022**, 203 (2022), arXiv:2212.10138 [hep-lat].

[64] Y. Aoki *et al.*, Lattice gauge ensembles and data management, PoS **LATTICE2024**, 412 (2025), arXiv:2502.08303 [hep-lat].

[65] M. Bruno *et al.*, Simulation of QCD with $N_f = 2 + 1$ flavors of non-perturbatively improved Wilson fermions, JHEP **02**, 043, arXiv:1411.3982 [hep-lat].

[66] M. Bruno, T. Korzec, and S. Schaefer, Setting the scale for the CLS 2 + 1 flavor ensembles, *Phys. Rev. D* **95**, 074504 (2017), arXiv:1608.08900 [hep-lat].

[67] T. Aoyama, T. M. Doi, T. Doi, E. Itou, Y. Lyu, K. Murakami, and T. Sugiura (HAL QCD), Scale setting and hadronic properties in the light quark sector with (2+1)-flavor Wilson fermions at the physical point, *Phys. Rev. D* **110**, 094502 (2024), arXiv:2406.16665 [hep-lat].

[68] R. E. Smail *et al.* (QCDSF/UKQCD/CSSM), Constraining beyond the standard model nucleon isovector charges, *Phys. Rev. D* **108**, 094511 (2023), arXiv:2304.02866 [hep-lat].

[69] Y. Aoki, K.-I. Ishikawa, Y. Kuramashi, S. Sasaki, K. Sato, E. Shintani, R. Tsuji, H. Watanabe, and T. Yamazaki (PACS), Method for high-precision determination of the nucleon axial structure using lattice QCD: Removing πN -state contamination, *Phys. Rev. D* **112**, 074510 (2025), arXiv:2505.06854 [hep-lat].